National and Kapodistrian University of Athens

Department of Physics

PhD Thesis

Nuclear structure of the neutron-rich nuclei ^{140}Ba and ^{180}Hf

Ahmed Khaliel

Athens, 2020

Advising committee members

- Theo J. Mertzimekis (Main advisor), Associate Professor, National and Kapodistrian University of Athens, Athens, Greece
- Efstathios Styliaris, Associate Professor, National and Kapodistrian University of Athens, Athens, Greece
- Michael Kokkoris, Professor, National Technical University of Athens, Athens, Greece

Examination committee members

- Theo J. Mertzimekis, Associate Professor, National and Kapodistrian University of Athens, Athens, Greece
- Efstathios Styliaris, Associate Professor, National and Kapodistrian University of Athens, Athens, Greece
- Michael Kokkoris, Professor, National Technical University of Athens, Athens, Greece
- Tassos Lagoyiannis, Senior Researcher, National Center for Scientific Research Demokritos, Athens, Greece
- Michael Axiotis, Researcher, National Center for Scientific Research Demokritos, Athens, Greece
- Dennis Bonatsos, Director of Research, National Center for Scientific Research Demokritos, Athens, Greece
- Nicu Mărginean, Senior Researcher I, Horia Hulubei National Institute for Physics and Nuclear Engineering (NIPNE), Magurele, Romania

Acknowledgements

I would like to express my sincere gratitude to my advisor, Prof. Theo J. Mertzimekis, for the continuous support of this thesis, his patience, motivation and immense knowledge, and for steering me in the right direction whenever he thought I needed it. It has been a wonderful experience working with him these past years which resulted in a very productive collaboration.

Besides my advisor, I would like to thank Prof. Angela Bracco and Prof. Fabio Crespi (INFN Milan) for their guidance during the conduction and the analysis of the ^{140}Ba experiment as well as for their insightful advice that they provided me with. Special thanks belongs to Dr. Nicu Mărginean, Senior Researcher I, at the 9MV Tandem lab at IFIN-HH, for his ideas, advice and guidance during the conduction and analysis of the ^{180}Hf experiment. Much credit is also given to Dr. Nicoleta Florea, Senior Researcher at the Target Laboratory of IFIN-HH, for her invaluable ideas during the target preparations. Furthermore, I would like to thank the rest of my thesis committee members, for their support, encouragement and their insightful comments which incited me to widen my research from various perspectives.

I would like to thank the staff of the 9MV Tandem lab at IFIN-HH and the members of the NuSTRAP group for their irreplaceable contribution during both experiments that have been studied in this thesis and for the excellent cooperation both in scientific and technical level.

Last but not least, I would like to thank my parents, Hatem Khaliel and Sotiria Zogaki, as well as my sister Christina Khaliel, for supporting me throughout writing this thesis, and my life in general.

H.F.R.I.
Hellenic Foundation for
Research & Innovation

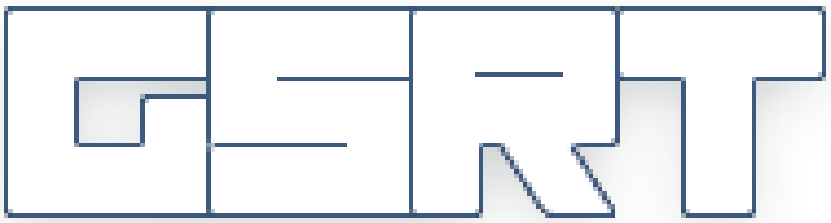

GENERAL SECRETARIAT FOR
RESEARCH AND TECHNOLOGY

This research work was supported by the Hellenic Foundation for Research and Innovation (HFRI) and the General Secretariat for Research and Technology (GSRT), under the HFRI PhD Fellowship grant (GA. no. 74117/2017).

Πυρηνική δομή των πλούσιων σε νετρόνια πυρήνων ^{140}Ba και ^{180}Hf

Εθνικό και Καποδιστριακό Πανεπιστήμιο Αθηνών, Τμήμα Φυσικής

Άχμεντ Χαλήλ

Περίληψη

Η μελέτη των πλούσιων σε νετρόνια πυρήνων αποτελεί ένα από τα πιο ενεργά πεδία έρευνας της σύγχρονης πυρηνικής φυσικής. Ιδιαίτερο ενδιαφέρον παρουσιάζουν οι άρτιοι-άρτιοι πυρήνες, μακριά από κλειστούς φλοιούς, κάποιοι από τους οποίους χαρακτηρίζονται από παραμορφωμένο σχήμα. Το φαινόμενο αυτό της παραμόρφωσης, δηλαδή της απόκλισης από το σφαιρικό σχήμα, μπορεί να εξηγηθεί μέσω της αναδιάταξης των μονοσωματιδιακών καταστάσεων, που μπορεί να οδηγήσει σε νέους κλειστούς φλοιούς, που δεν προβλέπονται από το μοντέλο των φλοιών.

Η ανάπτυξη νέων ανιχνευτικών διατάξεων, ικανών να απαρτίζονται από μεγάλο αριθμό ανιχνευτών, παράλληλα με την ανάπτυξη των ραδιενεργών δεσμών έχουν σημαντικά συνεισφέρει στη γνώση της δομής των πλούσιων σε νετρόνια πυρήνων. Ανιχνευτικές διατάξεις υψηλής απόδοσης στη γ-φασματοσκοπία έχουν βελτιώσει σημαντικά το βαθμό της πληροφορίας που μπορούμε να λάβουμε από ένα πυρήνα, καθώς πλέον μπορούν να πραγματοποιηθούν μετρήσεις μεγαλύτερης ακρίβειας σε σημαντικά μικρότερο εργαστηριακό χρόνο.

Οι πλούσιοι σε νετρόνια πυρήνες μπορούν να διεγερθούν με αντιδράσεις μεταφοράς νουκλεονίων, οι οποίες αποτελούν ένα δημοφιλές εργαλείο για μελέτες πυρηνικής δομής και η χρήση του έχει αποδειχθεί ιδιαίτερα επιτυχής. Σε αυτή τη διατριβή, μελετήθηκαν πειραματικά οι δύο πλούσιοι σε νετρόνια πυρήνες ^{180}Hf και ^{140}Ba. Πραγματοποιήθηκαν δύο πειράματα κατόπιν υποβολής επίσημης ερευνητικής πρότασης και αξιολόγησης από Διεθνή Επιτροπή (PAC) στο εργαστήριο επιταχυντή Tandem του IFIN-HH, στο Βουκουρέστι της Ρουμανίας. Και οι δύο

πυρήνες σχηματίστηκαν έπειτα από αντιδράσεις μεταφοράς νουκλεονίων, ενώ η εκπομπή της γ-ακτινοβολίας που ακολούθησε την αποδιέγερσή τους, ανιχνεύτηκε από τη συστοιχία ανιχνευτών ROSPHERE.

Ο σταθερός πυρήνας ^{180}Hf βρίσκεται σε μια περιοχή του μαζών του ισοτοπικού χάρτη όπου τα πρωτόνια και τα νετρόνιά του χαρακτηρίζονται από τροχιακά με υψηλές τιμές της Ω στροφορμής σε ελλειψοειδείς πυρήνες, κοντά στην ενέργεια Fermi. Αυτό αποτελεί αιτία για την παρουσία ισομερών καταστάσεων με υψηλή προβολή στροφορμής K, η οποία μαζί με τις αντίστοιχες περιστροφικές ζώνες μπορούν να δώσουν χρήσιμες πληροφορίες σχετικά με την διάταξη των μονοσωματιδιακών καταστάσεών του.

Στην παρούσα εργασία, ο πυρήνας ^{180}Hf σχηματίστηκε μέσω της αντίδρασης ^{181}Ta(^{11}B,^{12}C)^{180}Hf για πρώτη φορά στη διεθνή βιβλιογραφία, προκειμένου να διερευνηθεί αν υπάρχουν νέα υποψήφια K-ισομερή. Επιπλέον στόχος ήταν η μέτρηση των άγνωστων τιμών σπιν-ομοτιμίας καταστάσεων και του λόγου ανάμειξης διαφόρων μεταπτώσεων. Οι μετρήσεις των λόγων ανάμειξης είναι ιδιαίτερα σημαντικές, καθώς μπορούν να καθορίσουν το βαθμό επιμερισμού της πολυπολικότητας των μεικτών ηλεκτρομαγνητικών μεταβάσεων και συνεπώς είναι απαραίτητες για τη δοκιμή διάφορων θεωρητικών μοντέλων. Σε αυτή την εργασία παρουσιάζονται τα αποτελέσματα για σπιν-ομοτιμίες της ζώνης διέγερσης της βασικής κατάστασης έως την ενεργειακή στάθμη των 1084 keV, των καταστάσεων 1370 keV (μπάντα 6), 1374 keV (μπάντα 2) και των καταστάσεων 1821 keV, 1608 keV, οι οποίες δεν ανήκουν σε κάποια συγκεκριμένη ζώνη διέγερσης μέχρι σήμερα. Ειδικότερα για την ενεργειακή στάθμη των 1374 keV, η τιμή που βρέθηκε σε αυτή την εργασία ευνοεί την τιμή 4^-. Αυτή η μέτρηση διευθετεί τη διαφωνία που βρίσκεται στη βιβλιογραφία μεταξύ των τιμών σπιν-ομοτιμίας 3^- και 4^-. Αντίστοιχα, για την μετάβαση $1374 \rightarrow 309$ keV, ο λόγος ανάμειξης βρέθηκε να συμφωνεί με την προηγούμενη τιμή της βιβλιογραφίας, με μια τιμή ακριβέστερη κατά περίπου 60%. Επιπροσθέτως, μετρήθηκαν λόγοι ανάμειξης των μεταπτώσεων $1370 \rightarrow 309$, $1608 \rightarrow 1200$ και $1821 \rightarrow 1200$ keV. Για μετρήσεις όπου η στατιστική δεν επαρκεί για μια μόνο τιμή, όλες οι πιθανές τιμές σπιν-ομοτιμίας

και λόγου ανάμειξης παρουσιάζονται.

Ο δεύτερος πυρήνας που μελετήθηκε είναι ο πυρήνας ^{140}Ba. Υπάρχουν σοβαρές ενδείξεις ότι ο συγκεκριμένος πυρήνας χαρακτηρίζεται από υψηλές οκταπολικές αλληλοσυσχετίσεις. Το φαινόμενο των υψηλών οκταπολικών αλληλοσυσχετίσεων έχει παρατηρηθεί στις ισοτοπικές αλυσίδες του Ραδίου και το Βαρίου, και οι αντίστοιχοι πυρήνες φαίνεται χαρακτηρίζονται από ένα 'αχλαδοειδές' σχήμα (pear-shaped nuclei). Δύο πρόσφατες μετρήσεις σε γειτονικά ισότοπά του ^{140}Ba(^{144,146}Ba) εμφάνισαν τιμές των αντίστοιχων ανηγμένων πλατών μετάβασης που υπερβαίνουν κάθε θεωρητική πρόβλεψη. Επιπλέον, τα φασματοσκοπικά δεδομένα του ^{140}Ba είναι μέχρι σήμερα εξαιρετικά ελλιπή, καθώς μόνο ο χρόνος ημιζωής της 2_1^+ είναι γνωστός.

Ο πυρήνας σχηματίστηκε μέσω της αντίδρασης μεταφοράς δύο νετρονίων ^{138}Ba(^{18}O,^{16}O)^{140}Ba. Παρά τις υψηλές τεχνικές δυσκολίες, όπως πχ. την κατασκευή του στόχου, τροφοδοτήθηκαν οι ενεργειακές στάθμες στη ζώνη διέγερσης της βασικής κατάστασης μέχρι την 8^+ κατάσταση. Ο βαθμός της τροφοδοσίας ήταν ικανός ώστε να εξαχθούν κάτω όρια στις τιμές των χρόνων ημιζωής των υπολοίπων καταστάσεων της μπάντας της βασικής κατάστασης. Επίσης, μετρήθηκαν οι σχετικές ενεργοί διατομές των αντιδράσεων ^{138}Ba(^{18}O,^{16}O)^{140}Ba ως προς την αντίδραση ^{138}Ba(^{18}O,4n)^{152}Gd και ως προς το κανάλι ανελαστικής σκέδασης. Χρησιμοποιώντας θεωρητικούς υπολογισμούς για την αντίδραση ^{138}Ba(^{18}O,4n)^{152}Gd, κατέστη δυνατή η εξαγωγή των, άγνωστων μέχρι σήμερα, ενεργών διατομών της αντίδρασης ^{138}Ba(^{18}O,^{16}O)^{140}Ba, για ενέργειες δέσμης 61-67 MeV, κοντά στο φράγμα Coulomb. Μετρήσεις των ενεργών διατομών της συγκεκριμένης αντίδρασης είναι σημαντικές τόσο για λόγους πυρηνικής δομής, όσο και για τη μελέτη του μηχανισμού που πραγματοποιούνται γενικότερα οι αντιδράσεις μεταφοράς δύο νετρονίων. Παρόλο που η κατάσταση 3^- (η οποία μπορεί να καθορίσει το βαθμό των οκταπολικών αλληλοσυσχετίσεων) δεν τροφοδοτήθηκε στο συγκεκριμένο πείραμα, τα συμπεράσματα που εξάγονται από την παρούσα εργασία είναι επαρκώς ισχυρά για να καθοδηγήσουν μελλοντικές μελέτες για τον πυρήνα ^{140}Ba, τόσο σε ό,τι αφορά το ερώτημα του βαθμού οκταπολικών

αλληλοσυσχετίσεων, όσο και την επιλογή μελέτης του μέσω εναλλακτικών τεχνικών, που φαίνεται ότι απαιτεί ειδικές και δύσκολες να επιτευχθούν πειραματικές συνθήκες (ραδιενεργές δέσμες σε αντίστροφη κινηματική).

Nuclear structure of the neutron-rich nuclei ^{140}Ba and ^{180}Hf

National and Kapodistrian University of Athens,

Physics Department

Ahmed Khaliel

Abstract

The study of neutron-rich nuclei is one of the most active fields in contemporary nuclear physics. Special interest is focusing on even-even nuclides far from closed shells, some of which are characterized by a deformed shape. This deformation arises from the reordering of the single-particle states in equilibrium, which can eventually lead to new closed shells, different from those predicted by the shell model.

The development of large multi-detector arrays along with the availability of radioactive beams produced via fragmentation or spallation reactions has greatly increased our knowledge for nuclei located in the neutron-rich area of the isotopic chart. High-efficient γ-arrays enhance the amount of information extracted from a nucleus resulting in more precise measurements in a significantly reduced laboratory time. Furthermore, the development of radioactive beam facilities help in probing exotic isotopes in the neutron-rich side of the valley of stability.

Instead of radioactive beams, there is a more "traditional" way of populating excited states of a neutron-rich nucleus, especially the low-lying ones. Multi-nucleon transfer reactions are a widely used tool in nuclear structure, and it has been proven successful in populating excited states in neutron-rich isotopes. In this thesis, the two neutron-rich nuclei ^{180}Hf and ^{140}Ba have been studied experimentally. Two PAC-approved experiments were carried out at

the 9MV Tandem accelerator laboratory of IFIN-HH, Bucharest, Romania. Both nuclei were formed using multi-nucleon transfer reactions, and the subsequent γ-decay was detected by the ROSPHERE array.

The stable neutron-rich nucleus ^{180}Hf is located in a region where both protons and neutrons typically occupy high Ω orbitals located near the Fermi surface. This results in the presence of high K isomers, which along with the associated rotational bands can provide important information about the underlying single-particle orbitals.

In this work, the nucleus ^{180}Hf was populated using the proton pick-up reaction ^{181}Ta(^{11}B,^{12}C)^{180}Hf for the first time, aiming at the observance of possible new K isomers. An additional aim of the experiment was the measurement of unknown values of spins-parities of the populated levels, as well as the mixing ratios of the γ-transitions depopulating them. Mixing ratio measurements are highly important, as this quantity expresses the degree of partitioning of the multipole components of a mixed transition and consequently serve as a sensitive test for nuclear model calculations. In this work, measurements for spins-parities for the nucleus ^{180}Hf are presented for the ground-state band up to the 1084 keV state, the side-band states of 1370 keV(band 6), 1374 keV (band 2) and the non-band levels of 1821 keV and 1608 keV. Especially for the 1374 keV level, the value measured in this work favors a spin-parity assignment of 4^-, which settles the disagreement in the bibliography between the spin-parity values of 3^- and 4^-. Furthermore, the mixing ratio value for the transition 1374 $\rightarrow$ 309 keV, presented in this work, agrees with the previously reported measurement but is more precise by about 60%. In addition, mixing ratio values for the transitions 1370 $\rightarrow$ 309, 1821 $\rightarrow$ 1200 keV and 1608 $\rightarrow$ 1200 keV are reported for the first time. For the cases where the statistics is not sufficient, all possible values for spins-parities and mixing ratios are presented.

The second nucleus studied in this work is the neutron-rich ^{140}Ba. There are strong hints that this nucleus is characterized by enhanced octupole correlations. Such effects have been previously observed in the Ra and Ba isotopic

chains, leading to pear-shaped nuclei. The two neighboring neutron-rich isotopes ^{144}Ba and ^{146}Ba have been studied recently using the Coulomb excitation technique along with radioactive beams, yielding a high value for the corresponding reduced transition probabilities, higher than any theoretical calculation. Furthermore, the spectroscopic information regarding the nucleus ^{140}Ba is still poor, with only the lifetime of the 2_1^+ state measured.

The specific nucleus was populated using the $2n$-transfer reaction ^{138}Ba(^{18}O, ^{16}O)^{140}Ba. Despite the high technical difficulties, e.g. in target preparation, the ground-state band states up to the 8^+ level have been populated. The degree of population was sufficient to extract lower-limits for the lifetimes of the ground-state band. In addition, the relative cross sections of the reaction ^{138}Ba(^{18}O,^{16}O)^{140}Ba with respect to the fusion-evaporation reaction ^{138}Ba(^{18}O,4n)^{152}Gd and to the total inelastic channel have been measured. By using theoretical calculations for the reaction ^{138}Ba(^{18}O,4n)^{152}Gd, it was possible to extract the unknown cross sections of the $2n$-transfer reaction ^{138}Ba(^{18}O,^{16}O)^{140}Ba in the 61-67 MeV beam energy range, near the Coulomb barrier. Such measurements are important for nuclear structure, as well as for the understanding of the mechanisms that such reactions proceed. Even though the 3^- state (whose lifetime can lead to the evaluation of the degree of octupole correlations) was not populated, the results presented in this work are sufficient to guide future studies of ^{140}Ba to the right direction, either regarding the estimation of octupole correlations or the choice of an alternative experimental method (radioactive beams with inverse kinematics).

Contents

Chapter 1

Introduction

The study of neutron-rich nuclei is one of the most active fields in contemporary nuclear physics [1, 2]. Special interest is focusing on even-even nuclides far from closed shells, some of which are characterized by a deformed shape [3]. This deformation arises from the reordering of the single-particle states in equilibrium, which can eventually lead to new closed shells [4, 5], different from those predicted by the shell model [6–8].

The development of large multi-detector arrays along with the availability of radioactive beams produced via fragmentation or spallation reactions has greatly increased our knowledge for nuclei located in the neutron-rich area of the isotopic chart [2]. High-efficient γ-arrays enhance the amount of information extracted from a nucleus resulting in more precise measurements in a significantly reduced laboratory time. Furthermore, the development of radioactive beam facilities help in probing exotic isotopes in the neutron-rich side of the valley of stability. Their availability, however, is limited and there are still issues with beam contaminants and low counting rates, which can affect the accuracy of the measurements.

Instead of radioactive beams, there is a more "traditional" way of populating excited states of a neutron-rich nucleus, especially the low-lying ones. Multi-nucleon transfer reactions [9–12] are a widely used tool in nuclear struc-

ture, and it has been proven successful in populating excited states in neutron-rich isotopes [13, 14]. Such reactions can be studied in stable beam facilities, whose availability is wider compared to the radioactive beam ones, and require the use of a stable target, preferably isotopic. Transfer-reaction cross sections are in general sufficiently high to allow for such studies [9, 15], and the beam-induced background coming from fusion-evaporation reactions can be significantly reduced by using coincidence methods and/or a particle detector.

In this work, a study of the two neutron-rich nuclei ^{180}Hf and the ^{140}Ba is presented. Two experiments have been carried out at the 9MV Tandem accelerator laboratory in Horia Hulubei National Institute of Physics and Nuclear Engineering (IFIN-HH) [16]. Both isotopes were studied using multi-nucleon transfer reactions and their subsequent γ-decay was detected by the highly efficient ROSPHERE array [17].

The stable neutron-rich ^{180}Hf was populated using the proton pick-up reaction ^{181}Ta(^{11}B,^{12}C)^{180}Hf for the first time, aiming at the observance of possible new K isomers as well as the measurement of currently unknown spins-parities and mixing ratios using the $\gamma\gamma$ angular correlation method. This information is important for the single-particle structure of the observed states and the results of this work set the path for new measurements, aiming on the lifetimes of the observed transitions.

The nucleus ^{180}Hf is located in a region where both protons and neutrons typically occupy high Ω orbitals located near the Fermi surface [18]. This results in the presence of high K isomers [19], which along with the associated rotational bands can provide important information about the underlying single-particle orbitals. The Hf isotopes are some of the best examples of rigid and axially symmetric prolate rotors, making the projection K a good quantum number. The low-lying $K^{\pi} = 8^{-}$ isomer has been firstly studied in [21] using activation experiments at Argonne National laboratory. In [22], pulsed ^{238}U and ^{208}Pb beams have been used to populate high-K isomers in Hf iso-

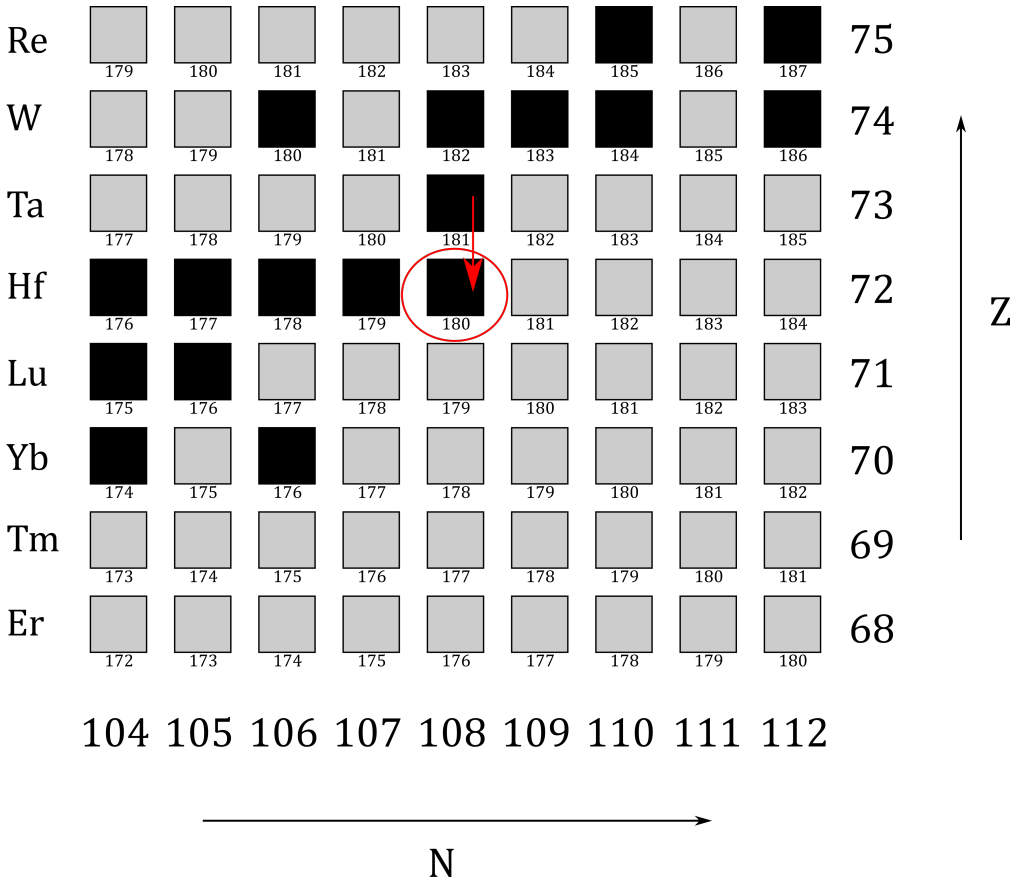

Figure 1.1: Position of ^{180}Hf on the isotopic chart and direction of the reaction ^{181}Ta(^{11}B,^{12}C)^{180}Hf.

topes, reporting $(10^+), 12^+, 14^+$ and (18^-) K-isomeres. In [18], the number of K-isomers is extended, reporting the $4^-, 6^+$ K-isomers, using centroid-shift and decay measurements.

From the above it is clear that ^{180}Hf consists a very good nucleus for providing insight about the structure of the underlying single-particle orbitals, of which information is limited in the neutron-rich area of the isotopic chart. This is expected, as there is a difficulty in populating neutron-rich nuclei at high spins. The reason for this is that fusion-evaporation reactions tend to populated mostly neutron-deficient nuclei. A recent experimental campaign at IFIN-HH [23] resulted in measurements of the lifetimes of the ground state band up to the 6_1^+, using the fast-timing technique. Still, there is a significant amount of certain band and non-band levels/transitions with uncertain structure properties, either in terms of their spins,parities and mixing ratios,

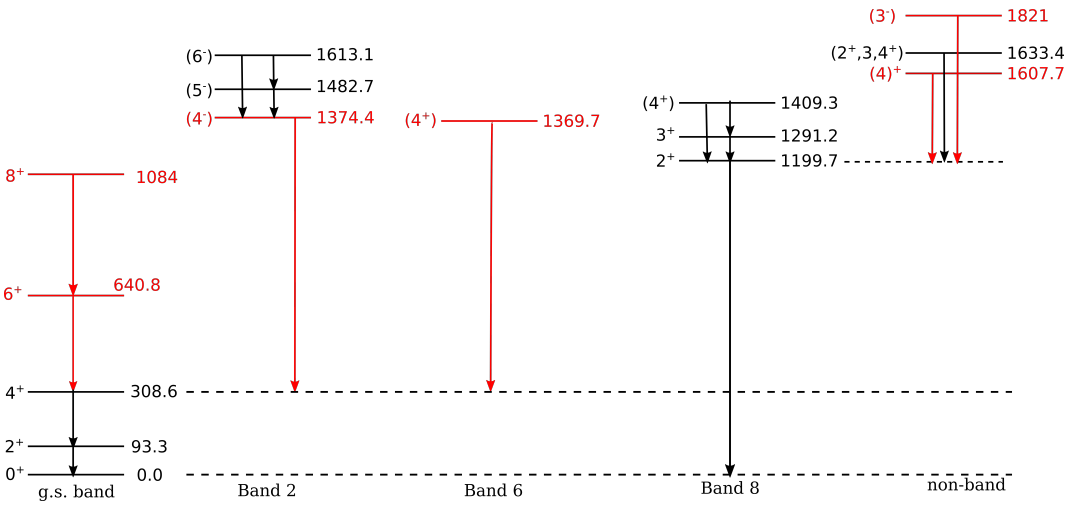

Figure 1.2: Partial level scheme of ^{180}Hf. Transitions and states in red are studied in this work [20].

or their lifetimes.

The direction of the ^{181}Ta(^{11}B,^{12}C)^{180}Hf reaction is shown in Fig 1.1. The particular reaction populated significantly the ground-state band, band 2, band 6, band 8 and several non-band levels. A partial level scheme showing some of the levels and transitions studied in this work is shown on Fig. 1.2. Spins and mixing ratios found in this work are compared with previous measurements [24, 25]. Unmeasured mixing ratios are also presented, and when the statistics of a measurement is not sufficient, the possible values of these observables are listed.

The second nucleus studied in this work is a candidate for having enhanced octupole correlations [26]. ^{140}Ba is located in the neutron-rich side of the Ba isotopic chain (see Fig. 1.3) and can be accessed using a $2n$-transfer reaction. The spectroscopic data of ^{140}Ba are still poor, with only the lifetime of the 2_1^+ state known [27]. The structure of the level scheme, such as a low-lying 3^- state and a negative-parity band besides the positive-parity ground-state band are strong hints of significant octupole correlations in a nucleus. Moreover, the two neighboring neutron-rich isotopes ^{144}Ba and ^{146}Ba have been studied using the Coulomb excitation technique along with radioactive beams [28, 29], so a dedicated study of ^{140}Ba is an important follow-up measurement for pursuing

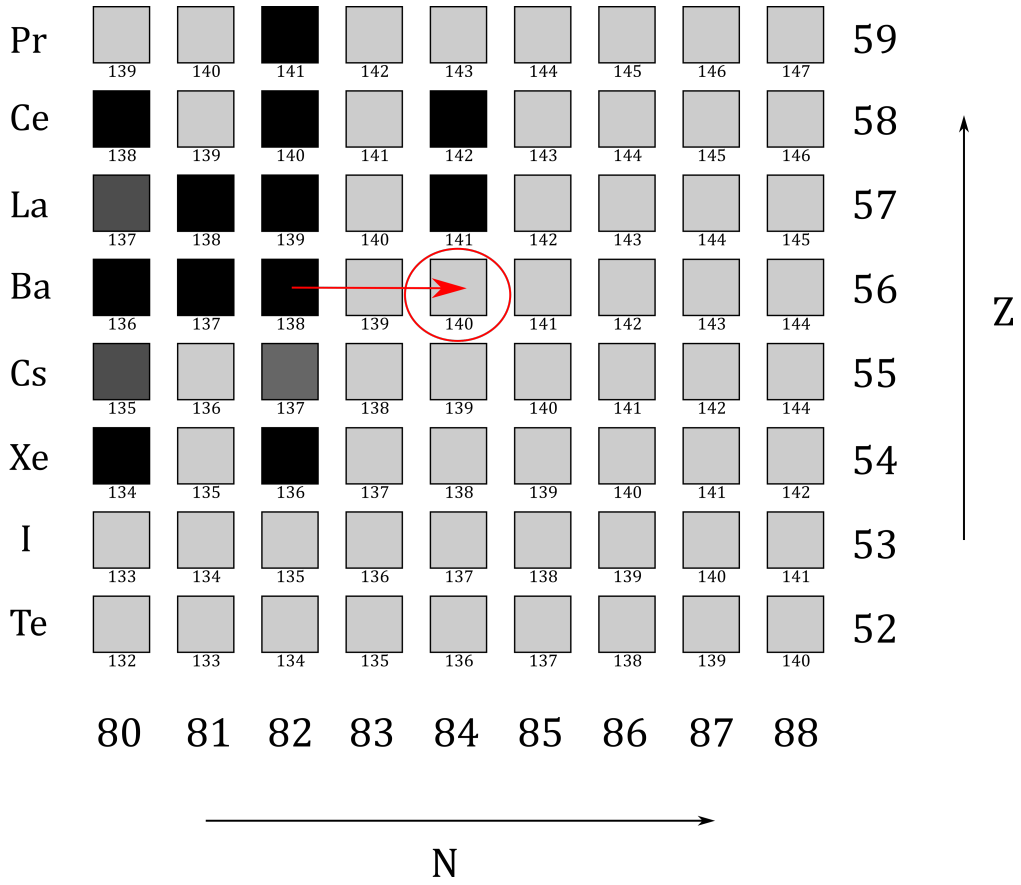

Figure 1.3: Position of the nucleus ^{140}Ba on the isotopic chart and direction of the reaction ^{138}Ba(^{18}O,^{16}O)^{140}Ba.

the onset of octupole correlations in the Ba isotopic chain.

A level scheme showing the low-lying levels of the ground-state band and the negative-parity side band is shown in Fig. 1.4. According to [26], bands with alternating parity along with enhanced $E1$ transitions are hints for enhanced octupole correlations. The 3^- state is of particular interest in the specific case, as a measurement of its lifetime will determine the strength of the transition $3^- \rightarrow 2_1^+$. If a branching ratio can be extracted from a measurement, this would lead also to the estimation of the reduced transition probability $B(E3; 3^- \rightarrow 0^+_{g.s.})$, which will clarify the situation regarding the octupole correlations in the specific isotope.

There are various theoretical studies regarding the many aspects of the Ba isotopic chain. Regarding octupole correlations, [30] presents theoretical cal-

culations for the $^{142-148}$Ba. In the specific description, two parameters have been taken into consideration: the octupole deformation in mass distribution and the position of the center-of-mass of the system. The first parameter is used for the study of reflection assymetric shapes while the second for the establishment of the coordinates of the center-of-mass to the origin of the frame of reference. The interaction which was used along with the Hartree–Fock–BCS method was the Gogny force because of its realistic character and its success in describing the properties of the ground-states of both spherical and deformed nuclei. In [31], the properties of the octupole deformations are described in terms of the Barcelona–Catania–Paris (BCP) density functionals. The Hartree–Fock–Bogolyubov method was used for the analysis. By using a constraint in the axially symmetric octupole moment, it was possible to extract the Potential Energy Curves (PECS), in order to determine their minima and find the octupole deformations. PECS calculations were performed for the isotopes ^{140}Ba up to ^{150}Ba. Along with the PECS calculations, the reduced transition probabilities $B(E1)$ and $B(E3)$ were also calculated, using Collective Schrodinger Equation–CSE.

In this work, the nucleus ^{140}Ba was populated using the $2n$-transfer reaction ^{138}Ba(^{18}O,^{16}O)^{140}Ba, which has been successful in populating the neutron-rich nucleus ^{66}Ni in a previous study [13]. Besides the high technical difficulties in target making (Barium is a material that oxidizes very quickly when exposed to air, thus making the manufacturing of a target quite challenging and a "difficult" nucleus to study using stable beams), the ground-state band levels were populated sufficiently to allow for a rough estimate of the lower limits of their lifetimes. The 3^- state was not observed in the spectra, probably because of the relatively high beam-induced background.

As a side-measurement, a study of the reaction ^{138}Ba(^{18}O,^{16}O)^{140}Ba has also been performed in this work by estimating its cross section for 4 beam energies near the Coulomb barrier. The particular reaction is important, as $2n$-tranfer reactions are widely used to access the neutron-rich area [13]. Cross

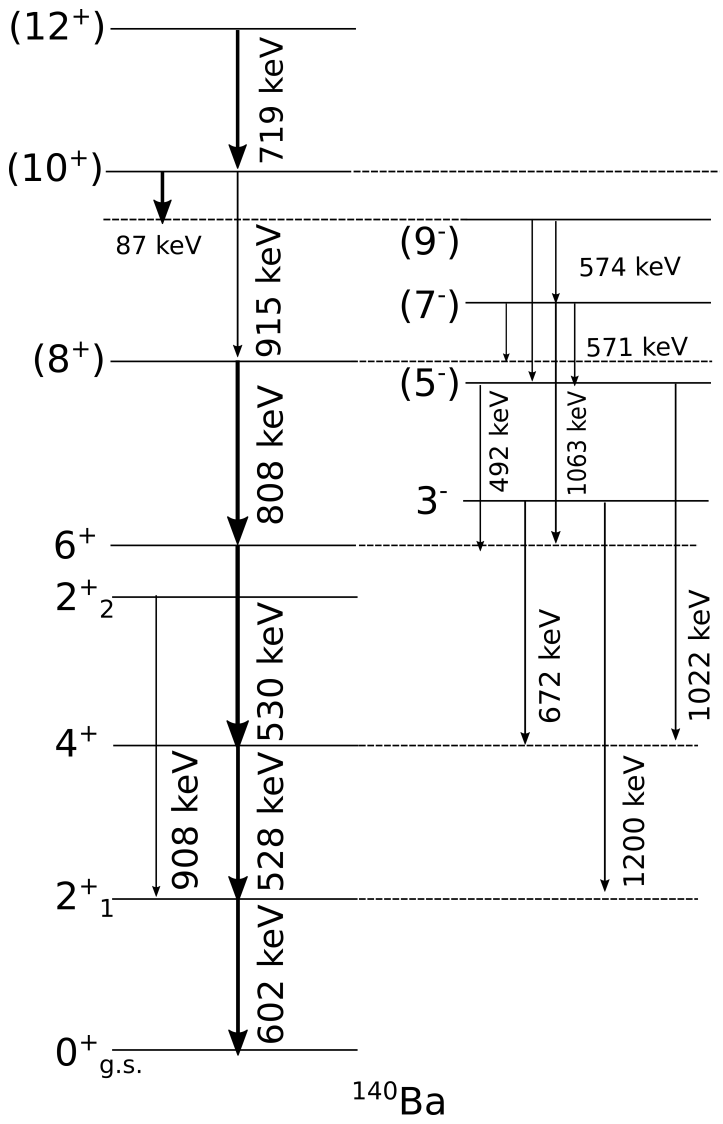

Figure 1.4: Part of the level scheme of ^{140}Ba, showing the ground state band and the side band [20]. One can notice the alternating parity states between the two bands, which is a hint for significant octupole correlations.

section data, either absolute or relative, are important for estimating the degree of level populations of the reaction products. Experimental cross section data are still scarce for such reactions, especially for Barium. The relative cross sections of the $2n$-transfer reaction ^{138}Ba(^{18}O,^{16}O)^{140}Ba with respect to the fusion evaporation reaction ^{138}Ba(^{18}O,$4n$)^{152}Gd, as well as to the total inelastic channel have been measured in this work. Then, by using theoretical calculations for the fusion-evaporation channel, the absolute cross sections for the

^{138}Ba(^{18}O,^{16}O)^{140}Ba reaction have been extracted. These measurements can serve as a reference point for various theoretical studies, i.e. refining Optical Model Potentials, or further experimental studies using such reactions.

The structure of this thesis is as follows: the necessary theoretical framework and the importance of the observables measured in this work are described in Chapter 2. The 9MV Tandem accelerator as well as the detection setup (ROSPHERE array) are described in Chapter 3. The analysis and results regarding the nucleus ^{180}Hf are presented in Chapter 4, while the analysis and results for the nucleus ^{140}Ba are described in Chapter 5. In the end, the conclusions of this work as well as a reference to the future directions of similar studies in these nuclei are given in Chapter 6.

Chapter 2

Theoretical Framework

2.1 Collective motion in nuclear systems

2.1.1 Nuclear Vibrations

The nuclides that lie near closed shells can be described sufficiently well by the nuclear shell model [6–8]. However, for nuclei characterized by proton and neutron numbers away from the magic numbers, a collective approach for studying these systems is favored [7, 32].

The saturation of forces in nuclear matter [7, 8] allows the treatment of a nucleus as a liquid drop, whose observed properties can be understood, to a first approximation, from the interplay between the surface tension and the volume energy of the liquid drop. Thus, nuclear excitations can be treated as different modes of *vibrational* motion.

When a nucleus is at its equilibrium configuration, it can be assumed that its shape is spherical [6]. This assumption is a simplification, but it can enhance the picture of a vibrational nucleus, as spherical shapes do not have rotational degrees of freedom. In practice though, most nuclei have a deformed shape in their equilibrium configuration, and vibrational motion is built upon it.

Considering the nucleus as a liquid drop, the deviations from a default spherical shape with the same density can be described by a function $R(\theta, \phi)$,

which represents the distance from the center of the system to the surface at a polar angle θ and at an azimuthal angle ϕ. This function can be expanded in terms of the spherical harmonics as follows [6, 7, 32]:

$$R(\theta, \phi) = R_0 \left[1 + \sum_{\lambda\mu} a_{\lambda\mu} Y_{\lambda\mu}(\theta, \phi) \right] \tag{2.1}$$

where R_0 is the radius of a sphere having the same density. A mode of order λ is characterized by $2\lambda + 1$ parameters of μ, where $-\lambda \leq \mu \leq \lambda$. Due to rotational invariance, these parameters are dependent on each other [6].

The dipole mode $\lambda = 1$ corresponds to an oscillation around a fixed point in the lab. If the internal structure is not changed (isoscalar mode [6]), then this case does not correspond to a nuclear excitation, as the vibration corresponds to a motion of the center of mass of the nuclear system. However, the isovector [6] dipole mode corresponds to an oscillating motion of the centers of masses of protons and nucleons. This is the cause of the giant dipole resonance [6, 33], which is observed in various nuclei. The quadrupole mode $\lambda = 2$ describes an oscillation between prolate and oblate shapes (see Fig. 2.1). A prolate shape is an ellipsoid with its polar radius larger than its equatorial one. The opposite is called oblate. Positive quadrupole deformation corresponds to a prolate shape, while negative quadrupole deformation corresponds to an oblate one. The octupole mode $\lambda = 3$ corresponds to oscillations of octupole deformations. Such shapes are reflection-invariant, having usually the shape of a "pear". Octupole deformations have been observed in the Ra and Ba isotopic chains [26] and are of special interest in contemporary nuclear physics research. The case of ^{140}Ba is investigated in this work.

A vibrational quantum of energy or mode of vibration, is called a *phonon*. The phonon is a boson and carries $\lambda\hbar$ units of angular momentum with a parity $\pi = (-1)^\lambda$. The ground state of an even–even nucleus is a zero-phonon state. The excited states of such a nucleus can arise from the coupling of a quadrupole phonon ($\lambda = 2$), an octupole one ($\lambda = 3$) etc. For the coupling of two quadrupole phonons, the possible angular momenta are $0^+, 2^+, 4^+$. Dif-

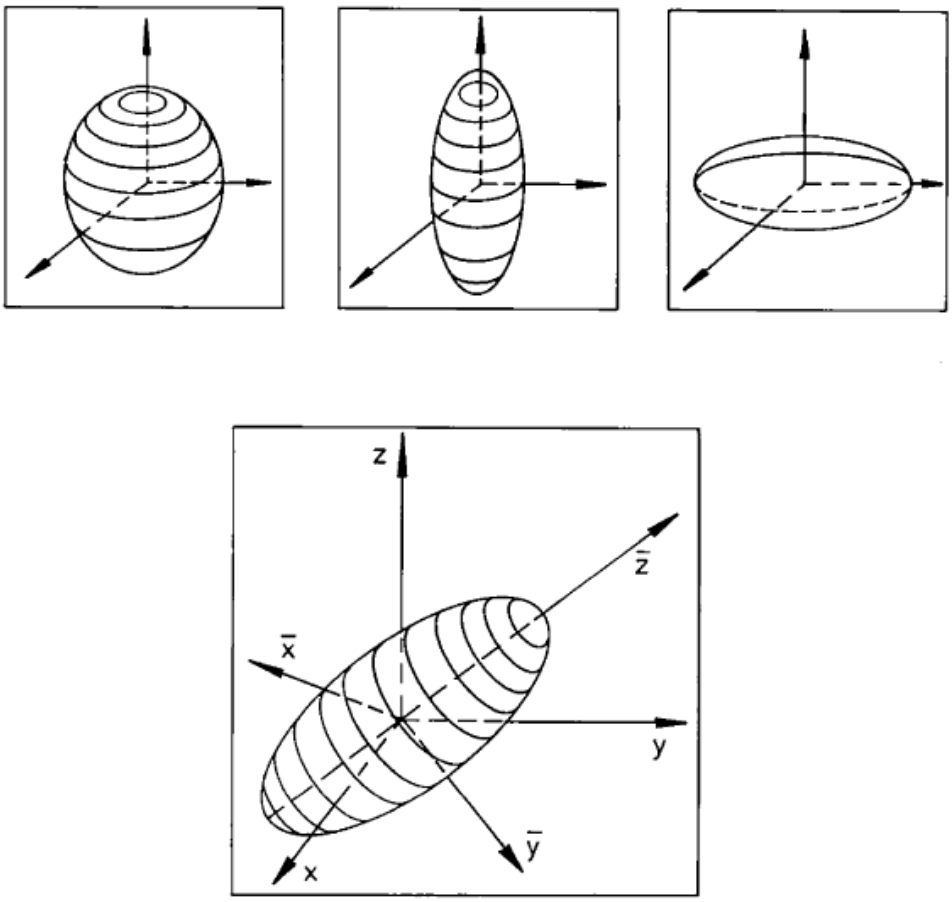

Figure 2.1: Illustration of nuclear shapes, from left to right: spherical, prolate and oblate nucleus. The lab frame of reference xyz and the intrinsic frame of reference $\bar{x}\bar{y}\bar{z}$ are also shown [34].

ferent combinations of phonons can occur and provide the level scheme of a nucleus [6, 7, 32].

2.1.2 Nuclear Rotations

In the vibrational model, the nuclear shape is assumed to be spherical while excitations are built upon the equilibrium configuration in the form of phonons. However, nuclei in the regions $150 \lessapprox A \lessapprox 180$ and $220 \lessapprox A \lessapprox 250$ are characterized by a deformed equilibrium shape [6, 7]. The reason for this lies on the interplay between the nuclear force and the Coulomb force acting on a *rotating* nucleus.

Spherical nuclei lie around closed shells. The reason for this is that all magnetic substates m are fully occupied, making the total angular momentum $L = \sum l_i$, where l_i is each nucleon's angular momentum, equal to zero. Such a quantum system is invariant under arbitrary rotations of the coordinate system, thus leading to a spherical shape [6]. In between the closed shells, however, the situation can be different. Many single-particle states are available, and they can be filled in such a way so that the shape of the system would be non-spherical.

Rotational degrees of freedom cannot be associated with a spherical quantum object, as the wavefunction of a sphere is independent of any angles. On the other hand, if a quantum system is deformed, the rotational motion can be detected by observing the changes in the orientation of a symmetry axis with time.

The angular momentum $\boldsymbol{J}$ of a rotating nucleus is proportional to the angular velocity ω:

$$\boldsymbol{J} = \mathcal{I}\boldsymbol{\omega} \tag{2.2}$$

where $\mathcal{I}$ is the moment of inertial. The kinetic energy associated with the rotational motion is then given by the relation:

$$E_j = \frac{1}{2}\mathcal{I}\omega^2 = \frac{1}{2I}J^2. \tag{2.3}$$

The transition to quantum mechanics is done by assigning the operator of the angular momentum. The rotational part of the Hamiltonian of the system is:

$$H = \sum_{i=1}^{3} \frac{\hbar^2}{2\mathcal{I}_i} J_i^2. \tag{2.4}$$

For the case of axially symmetric systems, such as prolate and oblate nuclear shapes, the moment of inertia along a body-fixed (intrinsic) coordinate system obeys the relation:

$$\mathcal{I}_1 = \mathcal{I}_2 \equiv \mathcal{I} \tag{2.5}$$

with $\mathcal{I}_3 \neq \mathcal{I}$, or else it corresponds to the spherical case. Thus, the Hamiltonian

can be written:

$$H = \frac{\hbar^2}{2\mathcal{I}}(\boldsymbol{J^2} - \boldsymbol{J_3^2}) + \frac{\hbar^2}{2\mathcal{I}_3}\boldsymbol{J_3^2}. \tag{2.6}$$

The eigenvalues of J^2 are $J(J+1)$ and of $\boldsymbol{J_3^2}$ is defined as K. Thus the energy of the system is a function of those two eigenvalues.

A nucleus in an intrinsic state can rotate with different angular velocities in the laboratory frame. A group of states with different angular momenta but sharing the shame intrinsic state is forming a *rotational band*. It is important to note that the only difference in these states is their rotational motion. Thus, the state which correspond to a rotational band are related to each other in terms of their energy, static moments and electromagnetic transition rates.

The rotational wavefunction takes the form [6]:

$$|JMK\rangle_{rot.} = \sqrt{\frac{2J+1}{16\pi^2(1+\delta_{K0})}}\left[\mathcal{D}^J_{MK}(\alpha,\beta,\gamma) \pm (-1)^{J+K}\mathcal{D}^J_{M-K}(\alpha,\beta,\gamma)\right] \tag{2.7}$$

where $\mathcal{D}^J_{MK}$ is the $\mathcal{D}$-function, δ_{K0} is the Kronecker delta and α, β and γ are the Euler angles. The $\pm$ sign corresponds to a positive or negative parity respectively. For $K = 0$, the wavefunction vanishes if the parity is positive and J is odd. Thus, for a $K = 0^+$ band, only even states of J can be built upon this bandhead. For $K > 0$, the only restriction on the allowed spin in a band is $J \geq K$, which is reasonable as K is the projection of of J in the intrinsic frame quantization axis. Thus, the above rules can be summarized as:

$$J = \begin{cases} 0, 2, 4, ... & \text{for } K^\pi = 0^+ \\ 1, 3, 5, ... & \text{for } K^\pi = 0^- \\ K, K+1, K+2, ... & \text{for } K^\pi > 0 \end{cases} \tag{2.8}$$

The energy of a rotational state will be then given, following Eq. 2.6:

$$E_J = \frac{\hbar^2}{2\mathcal{I}}J(J+1) + E_K \tag{2.9}$$

where E_K is the intrinsic energy of the system, corresponding to the intrinsic part of the wavefunction.

2.2 Gamma decay

2.2.1 Classical approach and the transition to quantum mechanics

A static distribution of charges or currents is the cause of electric and magnetic fields, respectively. These fields can be expanded to a series of Legendre polynomials, with each of the terms called multipole moments. One then can study the dipole field, the quadrupole field etc.

If L is an index defined such that the 2^L is the multipole order ($L = 1$ for dipole, $L = 2$ for quadrupole etc.) then the following rules apply [35]:

1. The angular distribution of 2^L radiation, relatively to a properly chosen direction follows the behavior of the Legendre polynomial $P_{2L}(\cos\theta)$.

2. The parity of the radiation field is [35]:

$$\pi(ML) = (-1)^{L+1} \tag{2.10}$$

$$\pi(EL) = (-1)^{L} \tag{2.11}$$

   It is obvious that the electric and magnetic multipoles of the same order have opposite parity.

The transition of the classical treatment of the radiation field to the quantum mechanical level is done by quantizing the multipole components of the electric and magnetic fields. This is done by replacing the multipole moments with multipole operators which act on the nuclear wavefunction and change it from an initial state ψ_i to a final one ψ_f. The decay probability is governed by the matrix element m_{fi} of the multipole operator [6, 35]:

$$m_{fi}(XL) = \langle\psi_i|\,\hat{O}\,|\psi_f\rangle \tag{2.12}$$

where $X = E, M$ for electric and magnetic transitions respectively, ψ_i and ψ_f are wavefunctions of the initial and final states and $\hat{O}$ is the nuclear part of

the transition operator [6]. The function of the operator $\hat{O}$ is to change the nuclear state from the initial state ψ_i to the final one ψ_f and in the process create a photon of the proper energy, parity and multipole order.

The decay constant or transition probability, which represents the probability of emitting a photon per unit time, is given by the relation [6, 35]:

$$T(XL) = \frac{8\pi(L+1)}{L[(2L+1)!!]^2}\frac{k^{2L+1}}{\hbar}B(XL; J_i \to J_f) \tag{2.13}$$

where k is the wavenumber, L is the carried away momentum and $B(XL; J_i \to J_f)$ is the *reduced transition probability*, defined as [6]:

$$B(XL; J_i \to J_f) = \sum |m_{fi}(XL)|^2 \tag{2.14}$$

where the sum runs in all possible final substates. As seen from the above equation, all information for the decay probability is included in the matrix elements $m_{fi}(XL)$, which can be determined if the initial and final wavefunctions are known and vice versa.

2.2.2 Reduced transitions probabilities and lifetimes

Several nuclear structure experiments focus on lifetime measurements for the extraction of information regarding the involved nuclear states. The lifetime of a state is directly connected to the reduced transition probability, a quantity which can offer valuable insight regarding the nuclear wavefunction, as well as the nuclear shape and its evolution.

In general, an excited state is characterized by a width Γ [6]. This width, under the best circumstances, is simply related to the mean lifetime τ of the state:

$$\Gamma\tau = \hbar. \tag{2.15}$$

The above equation directly arises from the uncertainty principle. The width Γ is a measure of the probability of the excited state to decay. The reduced transition probabilities can be calculated by the relation [6, 32]:

$$B(XL; J_i \to J_f) = (2J_i+1)^{-1} |\langle J_f|\hat{O}|J_i\rangle|^2 \tag{2.16}$$

where X can be either E for electric or M for magnetic transition, L is the multipolarity of the transition and J_i, J_f are the initial and final spin parts of the wavefunction, respectively. The reduced transition probability for the inverse transition is connected via the following relation:

$$B(XL; J_f \rightarrow J_i) = \frac{2J_i + 1}{2J_f + 1} B(XL; J_i \rightarrow J_f). \tag{2.17}$$

The total decay probability T in $[s^{-1}]$, defined as $T = \frac{\ln 2}{\tau_{1/2}}$ is related with the reduced transition probability as follows [6]:

$$T(EL) = \alpha\hbar c \frac{8\pi(L+1)}{L[(2L+1)!!]^2} \frac{1}{\hbar} \left(\frac{1}{\hbar c}\right)^{2L+1} E_\gamma^{2L+1} B(EL) \tag{2.18}$$

and

$$T(ML) = \alpha\hbar c \left(\frac{\hbar c}{2M_p c^2}\right) \frac{8\pi(L+1)}{L[(2L+1)!!]^2} \frac{1}{\hbar} \left(\frac{1}{\hbar c}\right)^{2L+1} E_\gamma^{2L+1} B(ML) \tag{2.19}$$

where $e^2 = \alpha\hbar c$ in cgs (centimeter-gram-second) units, $B(EL)$ in units of $e^2 fm^{2L}$ and $B(ML)$ in units of $\mu_N^2 fm^{2L-2}$, with μ_N being the nuclear magneton. In Appendix A, the relations for the transition probabilities of the lowest electric and magnetic multipoles are listed.

Experimentally, the lifetime τ of a state or a partial lifetime of a specific transition can be determined in most cases. They are related according to the following equation:

$$\tau(XL) = \tau \frac{I_{tot}}{I_\gamma(XL)} \tag{2.20}$$

where I_{tot} and $I_\gamma(XL)$ are the sum of all intensities depopulating the level of interest and the intensity of the transition (XL) respectively. The decay probability can then be found by the inverse of lifetime:

$$T(XL) = \frac{1}{\tau(XL)} \tag{2.21}$$

The single-particle transition probabilities are defined in terms of the Weisskopf units. These are given by the relations:

$$B_W(EL) = \frac{1.2^{2L}}{4\pi} \left(\frac{3}{L+3} A^{\frac{2L}{3}}\right) e^2 (fm)^{2L} \tag{2.22}$$

$$B_W(ML) = \frac{10}{\pi} 1.2^{2L} \left(\frac{3}{L+3} A^{\frac{2L-2}{3}}\right) \frac{e\hbar}{2m_c} (fm)^{2L-2} \tag{2.23}$$

The Weisskopf estimates are defined only for $J_i > J_f$.

2.2.3 The mixing ratio

There are often transitions, such as a $2^+ \rightarrow 1^+$, where both $E2$ and $M1$ transitions are allowed. When there is such a mixture of two multipoles, the degree of this mixing is characterized by the *mixing ratio* δ, defined as [6, 36]:

$$\delta^2 = \frac{T(X(L+1); J_i \rightarrow J_f)}{T(X'L; J_i \rightarrow J_f)} \tag{2.24}$$

The sign of δ, after taking the square root of Eq. 2.24 is a matter of convention discussed in [37]. Choosing a convention, however, is a non-trivial problem because the sign of the theoretical δ depends on the sign conventions employed for defining the electromagnetic operators and the reduced matrix elements. On the other hand, the sign of the experimental δ depends on the sign conventions employed for defining the axis of alignment with respect to which the γ-ray angular distribution is measured, and geometrical factors such as Clebsch-Gordan and Racah coefficients that enter the expression employed for the expansion of the angular distribution probability in terms of various polynomials (see § 2.2.4). The convention used for the measurements in this work is that of Krane and Steffen in [38].

The mixing ratio is a highly important quantity and can be measured experimentally. Precise measurements are essential for the calculation of the reduced transition probabilities from measured lifetimes, as accurate knowledge of the partitioning of the total decay probability into different multipole components is required. This information is given by the mixing ratio δ. Then the experimental reduced transition probabilities can be used as a sensitive test of nuclear model calculations.

Furthermore, parities are often assigned using the determined mixing ratio. For example, a large quadrupole component indicates an $E2/M1$ transition rather than an $M2/E1$. The most commonly used experimental method of

directly determining δ is the angular correlation method [36, 37, 39], which is applied in this work.

2.2.4 Angular correlations of successive γ-rays

A nucleus produced in an excited state, either by an α or β decay or by a nuclear reaction, will emit γ-rays that carry away energy and momentum. The energy carried out by a single photon is given by the relation $E_\gamma = pc = \hbar\omega$, where ω is the angular frequency of the emitted photon. If the nucleus is initially in an energy state E_i, and after the emittance of the photon decays to an energy state E_f, the conservation of energy requires:

$$E_i = E_f + E_\gamma + E_r \tag{2.25}$$

where E_r is the recoil energy of the final nucleus. The recoil energy is usually small enough to be considered negligible, as the nucleus is a relatively heavy system compared to the photon's energy.

If L is the carried away angular momentum of the photon emitted in the process of a transition from an initial state J_i to a final state J_f, then the following relation must hold:

$$|J_i - J_f| \leq L \leq J_i + J_f \tag{2.26}$$

The orientation of the angular momenta in space define the quantum number m, whose values are in the range $-J \leq m \leq J$, for a nuclear state of a spin J. It should be noted that the carried-away momentum of the photon should be $L \neq 0$, as there are no monopole electric or magnetic transitions [35].

For known initial and final spins, the photon angular momentum can only by constrained in a certain range of values (see Eq. 2.26). The experimental determination of the multipole character of an emitted γ-ray can only be determined by measuring the angular distribution of the radiation. However, an unequal population among the m substates needs to be created. This can be

done by either placing the sample in a strong magnetic field while simultaneously cooling the sample or observe a previous radiation. The second method is used in this work and it works as follows: One observes a cascade, for example the $0 \to 1 \to 0$, as shown in Fig. 2.2. By taking as the axis of quantization

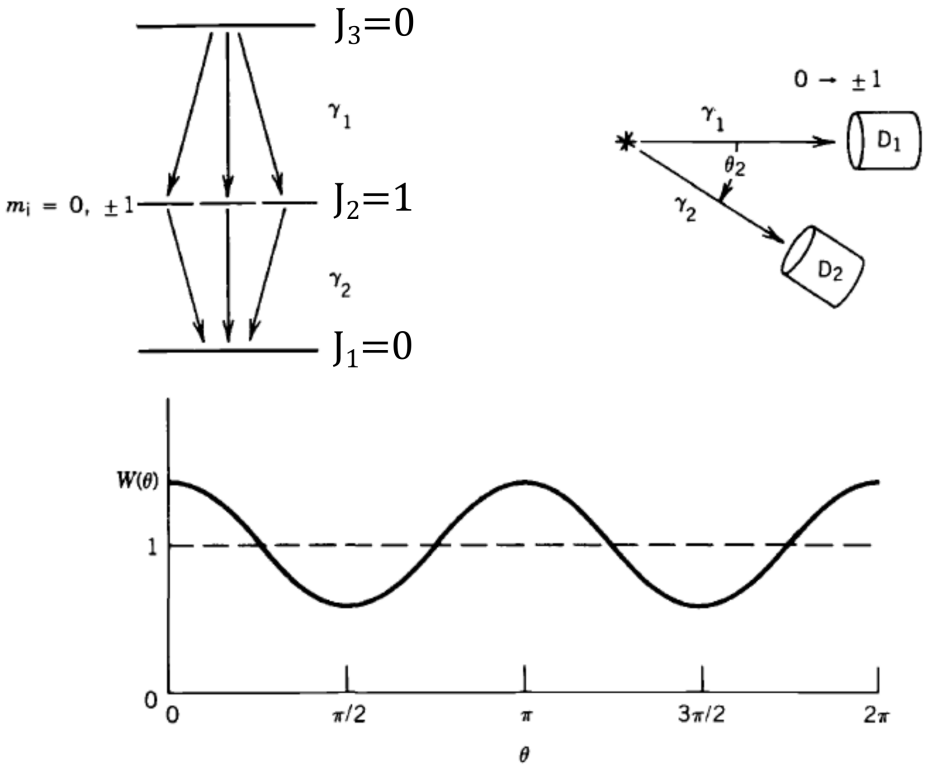

Figure 2.2: Example of observing a cascade of γ-rays between three levels of spins $0 \to 1 \to 0$. From [35].

the axis on which the first γ-ray is emitted, the transition from the J_2 level to the substate $m_i = 0$ cannot be populated, since $\theta_1 = 0$ and the angular behavior of the particular transition follows $W(0 \to m_i = 0) \propto \sin^2\theta_1$. Thus, the substates of the level $J_2 = 1$ are populated unequally, and this will result in an angular distribution of the second γ-ray γ_2 with respect to axis of the γ_1 having a behavior:

$$W(\theta_2) = \frac{1}{2}\left[\frac{1}{2}(1+\cos^2\theta_2) + 0\cdot\sin^2\theta_2 + \frac{1}{2}(1+\cos^2\theta_2)\right] \propto 1+\cos^2\theta_2 \quad (2.27)$$

This method is called an angular correlation measurement. It is important to note that one does not observe the partial characteristics of the radiation,

but a distribution of events with respect to the relative angle θ_2. As described later, this is enough to derive the spin and the mixing ratio of the initial state, and the firstly emitted γ-ray, if the spins of the following levels and the mixing ratio of the secondly emitted γ-ray are known.

The general form of an angular correlation function is [39]:

$$W(\theta) = A_0 \left[1 + a_2 P_2(\cos\theta) + a_4 P_4(\cos\theta)\right] \tag{2.28}$$

where θ is the relative angle, A_0 is normalization factor, which expresses the average of the $W(\theta)$ function, a_2 and a_4 are coefficients which depend on the spins and parities of the levels involved in the cascade and P_2 and P_4 are Legendre polynomials of second and fourth order, respectively.

The theoretical calculation of the a_2 and a_4 coefficients is explained thoroughly in [39]. For a cascade of two γ-rays $\gamma_1(L_1, L_1')$ and $\gamma_2(L_2, L_2')$ of the form $J_3 \to J_2 \to J_1$, the theoretical values for a_2 and a_4 can be calculated by the relation [38, 39]:

$$\begin{aligned} a_k(\delta_2, \delta_1) =& \frac{1}{1+\delta_1^2}[F_k(L_1, L_1, J_1, J_2) + (-1)^{(L_1 - L_1')} 2\delta_1 F_k(L_1, L_1', J_1, J_2) \\ &+ \delta_1^2 F_k(L_1', L_1', J_1, J_2)] \\ &\times \frac{1}{1+\delta_2^2}[F_k(L_2, L_2, J_3, J_2) + 2\delta_2 F_k(L_2, L_2', J_3, J_2) \\ &+ \delta_2^2 F_k(L_2', L_2', J_3, J_2)] \end{aligned} \tag{2.29}$$

where L_i and L_i' are two multipolarities of the emitted photons and δ_1 and δ_2 are the multipole mixing ratios of the first and second transition. The two lowest multipolarities often dominate the transition. The coefficients F_k are defined and tabulated in [40] by Frauenfelder and Steffen, and they are functions of the Clebsch-Gordan and Racah coefficients:

$$\begin{aligned} F_k(L, L', J_i, J) =& (-1)^{J_1 + J - 1}[(2L+1)(2L'+1)(2J+1)(2k+1)^{1/2}] \\ &\times \begin{pmatrix} L & L' & k \\ 1 & -1 & 0 \end{pmatrix} \begin{Bmatrix} L & L' & k \\ J & J & J_i \end{Bmatrix} \end{aligned} \tag{2.30}$$

where the array in parenthesis is the Wigner 3-j symbol, while the array in curly braces is the Wigner 6-j symbol [41].

The measurement of an angular correlation requires sufficient population of the states of interest in a nucleus. There are many ways of populating nuclear excited states, but it is usually done either by β decay or by nuclear reactions in which their exit channel is the nucleus of interest. In this work, transfer reactions have been used, and are described in the next section.

2.3 Transfer reactions and the GRAZING model

Multi-nucleon Transfer Reactions (MTR) are important tools for nuclear structure studies [9, 42, 43]. Especially for energies close to the Coulomb barrier, transfer–reaction cross sections are a large fraction of the total reaction cross section [9], thus leading to a significant population of excited states of the produced nuclei. It is under discussion that such reactions can offer a new pathway for the study of neutron–rich transuranium isotopes and superheavy elements [44], as their expected yields are comparable to the fusion reactions, while providing the advantage of offering a wide range of populated isotopes during the same experiment.

Two–neutron transfer reactions have been successfully used for populating the excited states of nuclei, which are moderately rich in neutrons [13]. For a small number of nucleon transfers and for energies close to the Coulomb barrier, these reactions can be described as grazing collisions, using the semi-classical grazing model [45]. Assuming a nuclear transfer reaction of the form $A(a,b)B$, where the projectile and the target have atomic and mass numbers Z_a, A_a and Z_A, A_A respectively, then after the collision, the nucleus will be rearranged so that the ejectile and the residual nucleus have atomic and mass numbers $Z_b + \Delta Z, A_b + \Delta A$ and $Z_B - \Delta Z, A_B - \Delta A$ respectively. Obviously, the quantities ΔA and ΔZ represent the transferred nucleons and protons,

respectively. The total reaction cross section according to this model is [45]:

$$\sigma_{reac.} = 2\pi \int_{\rho_g}^{\infty} (1-\rho_0)\rho d\rho \tag{2.31}$$

$$= 2\pi \int_{r_g}^{\infty} \left(1 - \frac{Z_a Z_A e^2}{2r_0 E(a)} - \frac{U_{aA}^N(r_0)}{E(a)} - \frac{r_0}{2E(a)}\frac{\partial U_{aA}^N(r_0)}{\partial r}\right) \tag{2.32}$$

$$\times \; [1-p_0(r_0)] r_0 dr_0 \tag{2.33}$$

where p_0 is the elastic scattering probability, $1-p_0(r_0)$ is the reaction probability, ρ are the impact parameters, $E(a)$ is the center of mass energy of the projectile, U_{aA}^N is the ion-ion potential and r_0 is the distance of closest approach. This distance is connected with ρ for a given center-of-mass energy $E(a)$, according to the following relation:

$$E(a) - \frac{E(a)\rho^2}{r_0^2} - \frac{Z_a Z_A e^2}{r_0} - U_{aA}^N = 0 \tag{2.34}$$

It is important to note that the integrand in Eq. 2.31 vanishes at the grazing (orbiting) distance r_g, as it is the distance of closest approach where the radial force is zero.

By defining $\Delta N = \Delta A - \Delta Z$ as the number of transferred nucleons, then the *grazing* cross section is:

$$\sigma(\Delta N, \Delta Z) = 2\pi \int_{\rho_g}^{\infty} \left[P(\Delta N, \Delta Z) - p_0 \delta(\Delta N, 0)\delta(\Delta Z, 0)\right] \rho d\rho \tag{2.35}$$

where $P(\Delta N, \Delta Z)$ is the probability distribution for the reaction characterized by $\Delta N, \Delta Z$ and $\delta(\Delta N, 0), \delta(\Delta Z, 0)$ are δ-functions. The treatment and derivation of probability distributions for the grazing model is thoroughly described in [45].

Winther's grazing model [45] has been proven successful for the description of one– or two–nucleon transfer reactions [46]. Calculations performed with the `GRAZING 9` code use a semi–classical approach developed in [47]. For a small number of nucleon transfers (up to 6–8 neutrons) and for nuclei close to the magic shell closures, the particular model describes experimental data very well; however, it tends to slightly underestimate the data for large numbers of nucleons (see discussion in [48]).

2.4 Fusion-evaporation reactions

In a fusion-evaporation reaction, the projectile and the target initially form a compound system in high excitation energies near the continuum called "compound nucleus". Due to its large angular momentum, it is possible for the compound nucleus to emit a number of nucleons after its formation. These types of reactions are widely used as a tool for nuclear structure studies, because of the high degree of populating high-spin states in heavy nuclei.

The crucial starting point in describing a fusion is the choice of an *optical* nucleus-nucleus potential. Calculations in this work have been performed using the Bass optical potential [46, 49], which is derived using geometrical interpretations for nuclear systems with $Z_pZ_t = 64 - 850$:

$$V_{N-N}(r) = \frac{R_pR_t}{R_p + R_t}\left[0.033\exp(s/3.5) + 0.007\exp(s/0.65)\right]^{-1} \tag{2.36}$$

where $s = r - R_p - R_t$ in fm, with r being the distance and R_p, R_t are the projectile and target radii, respectively.

The cross section of a fusion-evaporation reaction, with an entrance channel α and an exit channel β is evaluated by the relation:

$$\sigma_{f-e} = \sigma_{CN}P(\beta) \tag{2.37}$$

where the compound nucleus formation cross section is calculated using the formula:

$$\sigma_{CN} = \pi\lambda^2\sum_{l=0}^{\infty}(2l+1)T_l \tag{2.38}$$

while $P(\beta)$ is the probability of the compound nucleus to decay via channel β. In Eq. 2.38, l is the relative angular momentum of the projectile-target system and T_l are the transmission coefficients corresponding to the partial wave l.

In this work, fusion-evaporation calculations have been performed using the `PACE4` code, which is the latest version of a modified JULIAN code [50] and uses the Bass model [49], which was derived by using a geometric interpretation of available experimental data combined with a Monte–Carlo approach

to determine the decay of the compound system in the framework of Hauser–Feshbach formalism [51]. As stated in [46], the Bass model potential provides an overall excellent description for the fusion cross sections at energies starting from the Coulomb barrier and above. However, experimental evidence shows that the particular model significantly underestimates the cross section data below the Coulomb barrier (see [46] and references therein).

Chapter 3

Experimental setup

3.1 The 9MV Tandem accelerator of IFIN-HH

The Tandem Van de Graaff accelerator at Horia Hulubei National Institute of Physics and Nuclear Engineering (known as NIPNE or IFIN-HH) in Magurele, Bucharest [16] was built in 1973 by the High Voltage Engineering Corporation (HVEC-USA). It was later upgraded from the original terminal voltage of 7.5 MV (FN machine) to 9 MV. The original configuration of the machine using a charging belt was replaced with a more reliable Pelletron system in 2006, along new ion sources installed together with a new vacuum and power supply system. Because of a considerable seismic activity in the area, a mechanical earthquake protection system was installed [52], in order to protect the setup for mechanical damage caused by earthquakes.

The specific setup meets all contemporary requirements for nuclear structure and nuclear reaction studies in various areas of the isotopic chart, and especially for the neutron-rich exotic nuclear systems. Every stable isotope, apart from noble gases, can be accelerated. As the need to access neutron-rich isotopes has gained momentum in the last 10-15 years, an efficient means is to employ $2n$-transfer reactions using ion beams such as ^{14}C, ^{18}O. Such reactions can populate states in neutron-rich areas of the nuclear chart and study the

nuclear structure. Fusion-evaporation reactions of various reactants also allow for nuclear structure studies at high spins, especially in the neutron-deficient area.

A tandem accelerator works as follows: the negative ions are produced by a source, (usually either a duoplasmatron or a sputter source) and then are selected through an injection magnet. The selected ions are then accelerated by the positive potential of the terminal, which for the specific case can be charged to a maximum of 9MV. Then, the negative ions reaching the terminal region are stripped of their electrons using thin foils of carbon (5-10 g/cm^2) [16]. The stripped ion beam becomes positive and is now accelerated away by the same positive terminal potential. The term "Tandem" comes from this two-stage acceleration process. After the acceleration, the beam is focused using magnetic quadrupole lenses and analyzed by q/m (by treating the Lorentz force as the centripetal force) using a bipolar magnet. The path of the beam through the accelerator and onto the target is under vacuum (a level of 10^{-7} mb is achieved using turbo pumping). For the experiments carried out in this work, the negative ions were produced by a Cesium Sputtering source, which are firstly accelerated towards the positive high-voltage. The energy gain in this stage is:

$$E_1 = eV_t \tag{3.1}$$

where e is the elementary charge and V_t is the terminal voltage. In the stripper, consisting of carbon foils and placed in the high-voltage terminal, the negative ions are stripped of few or all of their electrons, exiting the stripper with a positive charge $+qe$ [53]. Then, these ions are further accelerated, gaining an energy:

$$E_2 = qeV_t \tag{3.2}$$

where q is the positive charge of the ion. By exiting the accelerator, the final total energy of the positive ions is the sum of the energies gained in the first

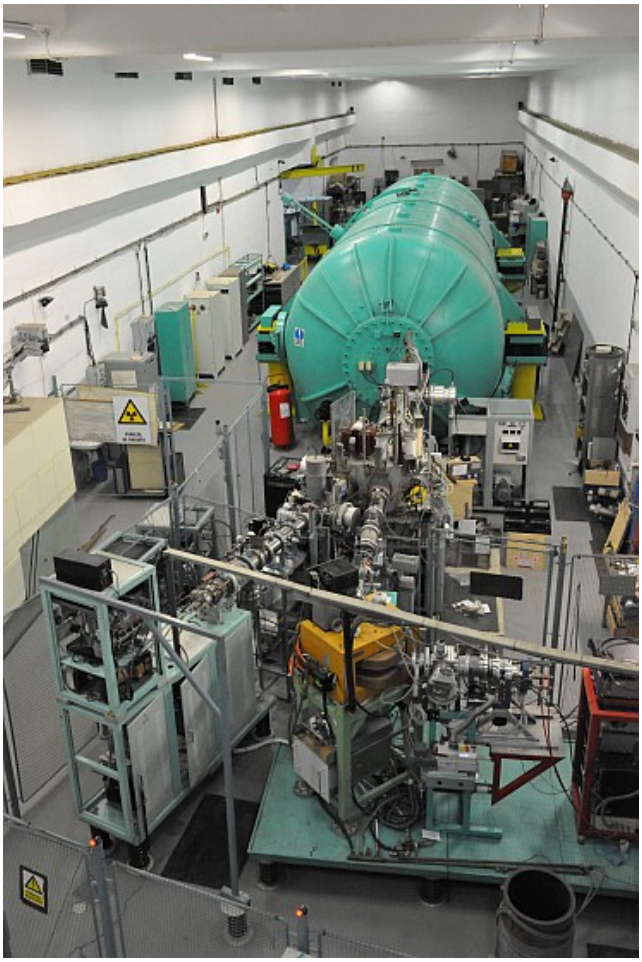

Figure 3.1: Picture of 9MV tandem accelerator at IFIN-HH [16].

and second stage of acceleration, thus:

$$E_f = E_1 + E_2 = eV_t + qeV_t = (1+q)eV_t \tag{3.3}$$

In Fig. 3.1 a photograph of the tank of the Bucharest IFIN-HH Tandem Van de Graaff accelerator is shown.

3.2 The Sputter source

A sputter source uses the Langmuir effect to create a beam of positive cesium ions in a surface ionization source [54]. The Langmuir effect is simply the ionization of atoms of low ionization potential that come into contact with a hot metal with a high work function. If an atom of low ionization energy W_i,

comes in contact with a hot solid surface (this surface is called the *ionizer*) with high work function W_a, then the least bound electron of the absorbed atom is lost to the surface and the atom departs, but now, as a positive ion.

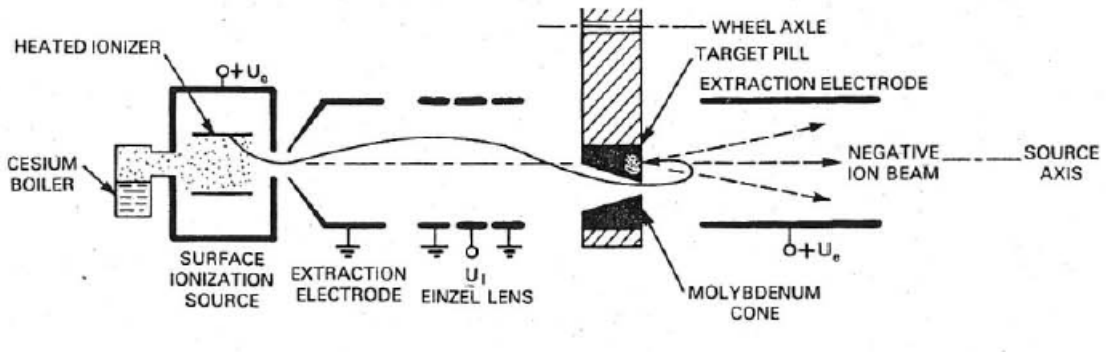

Figure 3.2: A sputter source [54].

A number of cesium atoms ($W_i = 3.89$ eV) is placed on a surface of tungsten ($W_a = 4.53$ eV) with temperatures of the order of 1000 °C. For the achievement of such a temperature, the ionizer is surrounded with a tungsten impedance which is heated as a current of 30 A flows through. Now, using the relation [54]:

$$\frac{N_i}{N_0} = \exp[-(W_i - W_a)/kT] \tag{3.4}$$

where N_i is the number of positive ions and N_0 the number of neutral atoms in the evaporating material, we find that 99.7% of the evaporating cesium atoms are positively charged. These atoms, provided as a vapor from a boiler, move to an aperture towards the ionizer. Using an Einzel lens, the cesium atoms, which have an energy about 30 keV are focused to a small spot and then they are steered onto the edge of a target cone containing the element of our interest. The cesium atoms bombard the target material and this leads to the production of various negatively charged ions, which are then extracted through a hole in the target cone by an electrode.

3.3 The ROSPHERE array

The ROmanian array for SPectroscopy in HEavy ion REactions is a multi-detector setup designed for γ-spectroscopy studies at the 9MV Tandem accelerator of IFIN-HH, Bucharest [55]. The specific array is designed for various measurements in nuclear structure such as $\gamma\gamma$ angular correlation measurements as well as lifetime measurements of nuclear excited states, using techniques such as the Doppler Shift Attenuation Method (DSAM) [56–58], the Recoil-Distance Doppler-Shift technique (RDDS) [59] and the Fast-timing technique [60].

The ROSPHERE array can host up to 25 High-Purity-Germanium (HPGe) detectors. Other detectors such as $LaBr_3$(Ce) scintillators can also be mounted. They are placed in spherical geometry, in five rings with respect to the beam axis in the following angles: $37°, 70°, 90°, 110°, 143°$. By combining all possible detector pairs, the setup is suitable for $\gamma\gamma$ angular correlation measurements, enabling the user to measure spins and multipolarity mixing ratios of excited nuclear states and γ-transitions, respectively.

A picture of the ROSPHERE array mounting 15 HPGE detectors and 10 $LaBr_3$(Ce) scintillators is shown in Fig. 3.3. The HPGe detectors used are commercially available coaxial ORTEC or CANBERRA. BGO shields are embedded on the HPGe detectors, consisting of 8 optically separated trapezoid-shaped BGO crystals with "nose" pieces, read out by 8 R6094 or 8 R3998 Hamamatsu PMTs. The BGO crystals have a thickness of maximum 29 mm and minimum 22 mm and a length of 178.6 mm or 146.6 mm. Tungsten collimators are mounted at the front of the BGO crystals, for shielding them from γ-rays emitted from the target position. Typical energy resolution is 18% at 662 keV [17].

Figure 3.3: Picture of the ROSPHERE array, mounting 15 HPGe and 10 $LaBr_3$(Ce) detectors.

3.3.1 General characteristics of HPGe detectors

HPGe detectors are semiconductor detectors, also referred to as *solid state* detectors, whose basic principle is similar to gas ionization detectors. The radiation now passes through a solid semiconductor, instead of a gas, and creates electron-hole pairs, instead of electron-ion pairs. These are collected by an applied electric field. The advantage of this kind of detectors is their excellent energy resolution, which comes from the relatively small energy required to create an electron-hole pair (about 10 times smaller than the energy for the creation of an electron-ion pair). As a consequence, the amount of ionization produced is an order of magnitude greater than the ionization produced in a gas ionization detector. In addition, the stopping power is greater than gaseous detectors.

Two main types of solid state detectors exist: Germanium and Silicon

detectors. For the case of gamma spectroscopy, germanium is always preferred because of its relatively high atomic number ($Z_{\mathrm{Ge}} = 32$ while for silicon is $Z_{\mathrm{Si}} = 14$. The probability of a photoelectric absorption to occur can be approximated as [61]:

$$P_{p.e.} \approx constant \times \frac{Z^n}{E_\gamma^{3.5}} \tag{3.5}$$

where n is a number between 4 and 5, and E_γ is the photon energy. This results in ~ 60 times greater photoelectric cross section [62].

The HPGe detectors are semiconductor diodes, with a structure of p-i-n, where the i area is very sensitive in ionizing radiation, especially in the range of X and γ-rays. They offer the highest resolution available for gamma-ray energies from a few keV up to 10 MeV. This is illustrated in Fig. 3.4 where a spectrum of ^{60}Co taken with a NaI detector is compared with the same spectrum taken now with a HPGe detector. It is obvious that the HPGe detector has a significantly higher resolution, and a higher peak-to-Compton ratio (as a result of the greater photoelectric cross section, as we mentioned earlier).

3.3.2 Energy resolution

The overall energy resolution of a germanium detection system is determined by mainly three factors:

- the inherent statistical spread in the number of charge carriers
- variations in the charge collection efficiency
- contributions of electronic noise

The intensity of each factor is determined by the energy of the incident radiation and the quality and size of the detector used. The full-width-at-half-maximum (FWHM) W_T, of a typical peak in the spectrum due to the detection of a monoenergetic gamma-ray can be synthesized as [61]:

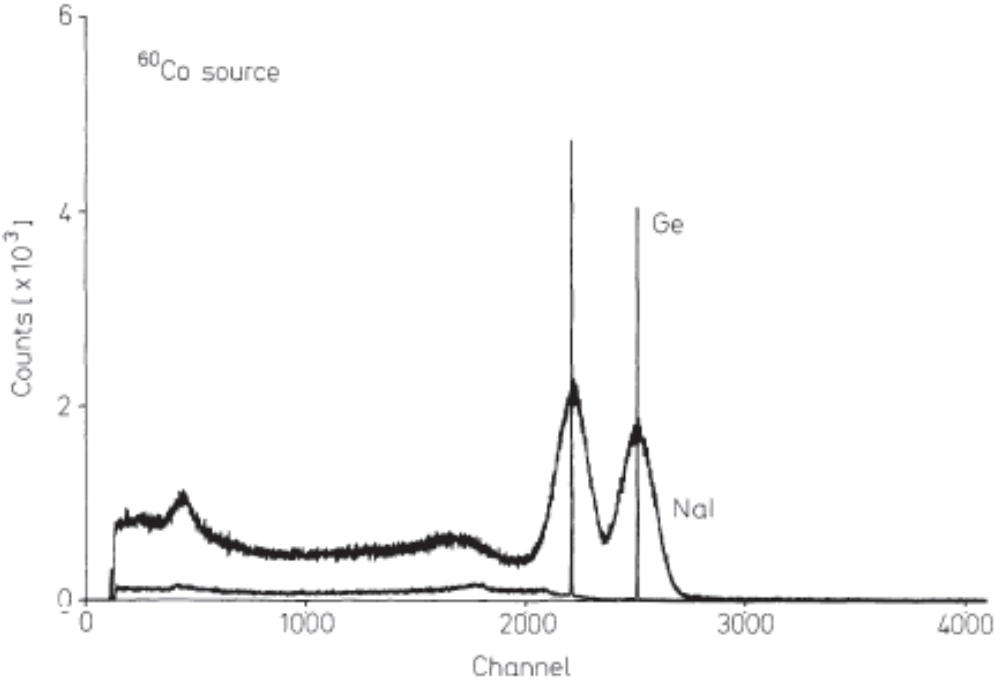

Figure 3.4: Comparison of a ^{60}Co spectrum taken with a NaI (top curve) and a HPGe detector [62].

$$W_T^2 = W_D^2 + W_X^2 + W_E^2 \tag{3.6}$$

where the first factor, W_D, represents the inherent statistical fluctuation in the number of charge carriers created:

$$W_D^2 = (2.35)^2 F \epsilon E \tag{3.7}$$

where F is the Fano factor, ϵ is the energy for the creation of one electron-hole pair and E is the gamma-ray energy. The second factor, W_X arises from incomplete charge collection and is most significant in large volume detectors and low average electric field. Its magnitude can be experimentally estimated by carrying out a series of FWHM measurements as the applied voltage is varied. The necessary assumption is that if an infinite electric field is applied, then the effects of incomplete charge collection are insignificant, thus $W_X \to 0$. Lastly, the third factor, W_E represents the broadening effects of all electronic components following the detector. The measurement of its magnitude is done by supplying the output of a precision pulser with a highly stable amplitude

to the preamplifier and recording the corresponding peak in the pulse height spectrum. These measurements should be made while the detector is normally connected to the preamplifier so that capacitive loading of the preamplifier input is typical of conditions under actual use. A parallel test pulse input to the preamplifier is normally provided for this purpose.

Energy resolution of germanium detectors are often specified at 5.9 keV (^{55}Fe), 122 keV (^{57}Co), 662 keV (^{137}Cs) or 1332 keV (^{60}Co). Large coaxial detectors will produce FWHM values of 800-1200 keV at 122 keV, rising to 1.7-2.3 keV at 1332 keV.

3.3.3 Detection efficiency

Measurements of absolute emission rates of γ-rays require knowledge of the detector efficiency. The emission rate of a point source can be calculated from:

$$S = N\frac{4\pi}{\epsilon_{ip}\Omega} \tag{3.8}$$

where N is the number of events recorded under the full energy peak, Ω is the solid angle subtended by the detector at the source position and ϵ_{ip} the intrinsic peak efficiency, by measuring the full energy peak area over a fixed time and by determining the solid angle Ω. Before the experiment, users carry out efficiency calibrations using sources calibrated by other means. The source-detector distance must be accurately measured to avoid errors in the relative solid angle. The calibration is normally carried out for an assortment of gamma-ray energies covering the range of interest to allow construction of an empirical efficiency versus energy curve.

For the calibration of our detector system, ^{152}Eu sources have been used, because of the convenient half-life (about 13 y) of ^{152}Eu [63] and the wide range of γ-ray energies produced in its decay. The whole procedure of efficiency calibration is described in the next chapter, as one of the first steps of the data analysis.

3.4 Electronics and data acquisition system

The electronics and data acquisition system of ROSPHERE consists of standard NIM and CAMAC modules. The electronics block diagram, shown in Fig. 3.5, has two distinct components: a standard slow coincidence part to select the coincidence of at least n HPGe detectors (usually $n = 2$ or 3) and a delayed coincidence part selecting the triple HPGe-$LaBr_3$(Ce)-$LaBr_3$(Ce) coincidences used for the fast-timing measurements.

The master trigger signal is generated through an OR condition by either the slow coincidence scheme (corresponding to n HPGe detectors firing) or by the delayed coincidence scheme (corresponding to the HPGe-$LaBr_3$(Ce)-$LaBr_3$(Ce) detector combination). The master trigger serves as a common START for the HPGe Time-to-Digital converter. The two individual triggers are sufficiently spaced in time (8 μs) with respect to the HPGe STOP signal to allow an easy offline selection of the desired trigger combination. This master trigger construction is important because it allows simultaneous fast-timing measurements and measurements requiring HPGe coincidences (e.g. in RDDS experiments).

The analogue FERA-bus fast CAMAC DAQ system is used, as it provides stability and flexibility as well as availability of hardware and software solutions. The system is fully compatible with the GASPware data analysis programs [64]. The hardware consists of a CMC203 Fera Driver/Memory/Histogrammer, that provides rapid readout and event control over the FERA-bus with a 1Mword buffer between the FERA data input and CAMAC data output, nine AD413A 4-channel, 13-bit Ortec Analogue-to-Digital Converters (ADC) used for the readout of HPGe energy information and LaBr3(Ce) energy and timing (TAC) information and two 4418 T Silena TDCs used for the HPGe timing information. The data in event-form are transferred through a Jorway 73A SCSI crate controller and stored on a local computer. The DAQ system can handle up to 2500 events/s without significant dead-time. However, if

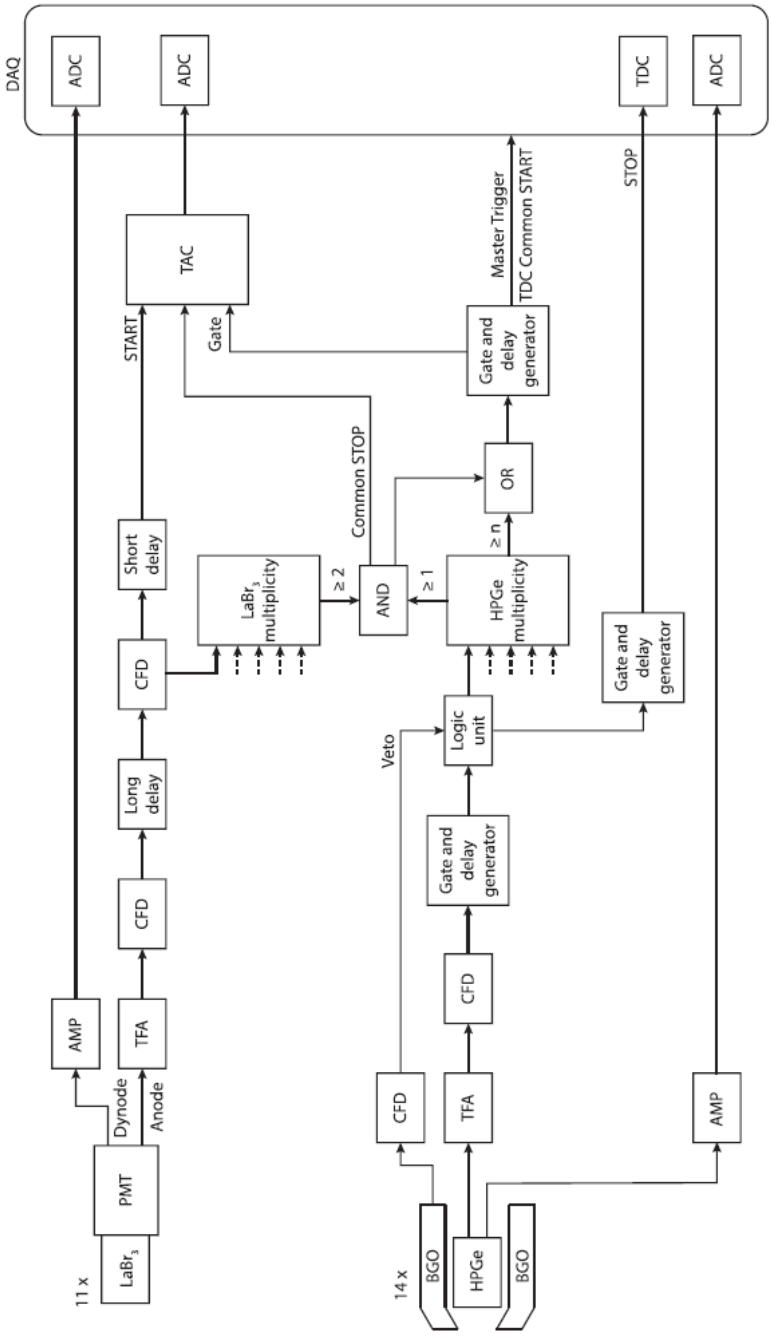

Figure 3.5: Schematic illustration of the electronics system of the ROSPHERE array [55].

this limit is surpassed, the dead-time becomes significant, rising to 50% at 5000 events/s. In the present work, the trigger has been set to $n = 2$ HPGe detectors in both experiments.

3.5 General Characteristics of Data Acquisition Systems

The purpose of the detection system is to register the radiation. This information is converted into an electrical signal, to be studied. This signal will be transferred to a computer where it can be processed and analyzed further. The signal must be carried without loss of information, to ensure data integrity and reliability. It is typically handled by the following types of devices:

- the pre-amplifier
- the amplifier
- the discriminator (in the main amplifier)
- the analog to digital converter (ADC)
- the multichannel analyzer
- the time to digital converter (TDC)

Finally, the data are stored in a computer, awaiting analysis. The main characteristics of the above devices will be analyzed in the following subsections.

3.5.1 The pre-amplifier

The basic objective of the pre-amplifier is to strengthen the weak signal coming from the detector, and lead them to the amplifier. The loss of information must

be as low as possible, and also, there should be no addition of noise currents to the amplified signal.

The initial signal coming from the detector is usually very weak, so it is wise that the connection of the detector with the amplifier to be short. This is the reason why the pre-amplifier is incorporated to the detector, so as to reduce the length of the connecting wire. Thus, the possibilities of additional signals that does not come from the experiment is reduced. Also, the signal-to-noise ratio is reduced, because of the reduced capacity of the short-length wire [62].

3.5.2 The main amplifier

Like the pre-amplifier, one of the main purposes of the main amplifier is to amplify the signal coming from the pre-amplifier. However, there is a second important feature that justifies the use of two amplifiers in a row. While the pre-amplifier's main purpose is to amplify the signal coming from the detector, the main amplifier must not only additionally amplify it, but also has to shape the signal to a convenient form, and then further process it. In short, the main amplifier:

- amplifies the signal coming from the pre-amplifier
- produces a conveniently shaped pulse for further processing

It is important, once again, that no information is lost after the signal exits the main amplifier. When timing information is required to be preserved, a fast response is necessary. For preserving information about pulse heights, it is essential to maintain a strict proportionality relation between input and output amplitudes (linear amplifier). Of the latter, an adjustable gain over a wide range is provided so as to allow a scale adjustment in a spectrum analyzer.

The pulse coming from the pre-amplifier has an exponential form, with a long tail lasting anywhere in the range from $\tau \approx$ few μs-100 μs. The amplitude

of this pulse is proportional to energy. If now, a second pulse arrives within period τ, it will ride on the tail of the first and its amplitude will be increased.

Consequently, there would be a distortion in the energy information, known as *pile-up*. There are two ways to overcome such a problem: either to restrict the counting rate to less than $1/\tau$ counts/s or to reshape the pulse by shortening the tail. The latter method is the most preferable option.

A second reason for pulse-shaping is the reduction of the signal-to-noise ratio. For a given noise spectrum, there is usually an optimum pulse shape in which the signal is least disturbed by noise. Tail pulses are not ideal typically, and it would be more advantageous to have a Gaussian or triangular form. Pulse-shaping remains important even at relatively low counting rates, where the pile-up events are not present.

3.5.3 The discriminator

The discriminator is a device which responds only to input signals with a pulse height greater than a certain threshold value. If this criterion is satisfied, then the discriminator issues a logical signal. If not, no response is made. The value of the threshold is adjustable, usually by a helipot or screw on the front panel. An adjustment of the width of the logical signal is usually possible via similar controls.

The discriminator is used for blocking low-amplitude noise pulses from detectors. "Good" pulses are large enough to trigger the discriminator are then transformed into logic pulses, which are further processed by the electronics (Fig. 3.6). This makes the discriminator a simple analogue-to-digital converter (ADC).

The discriminator uses the method of *triggering*. Because of its use in timing, it is important to keep the time relation constant between the arrival of the input pulse and the issuance of the output pulse. In most discriminators, triggering occurs at the moment the pulse crosses the threshold level. This is

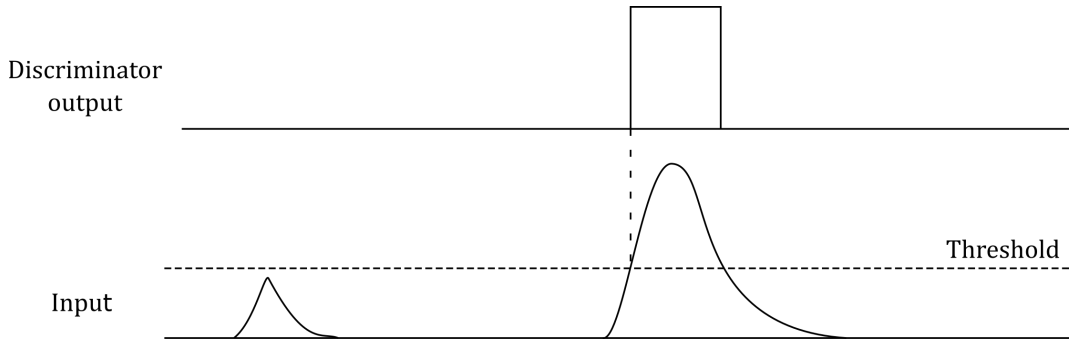

Figure 3.6: The discriminator triggers an output signal only if the input signal has an amplitude greater than the fixed threshold.

known as *leading edge* (LE) triggering.

There is a more precise method called *constant fraction* (CF) triggering [62], where the logic signal is generated at a constant fraction of the peak height, producing a walk-free signal. This technique requires a constant rise-time and its efficiency is very high, yielding walk as little as ±20 ps over an amplitude range of 100 to 1 [62].

3.5.4 The multi-channel analyzer (MCA)

The signal coming from the main amplifier is a set of random, both in time and shape, pulses. This signal then enters the multi-channel analyzer, whose main objective is to measure the amplitude and the number of pulses that occur in a small voltage range. As the height of pulse is proportional to the energy absorbed by the detector, the resulting list of numbers of counts will produce the desired γ-ray spectrum.

In order to understand how an MCA works it is useful to analyze the simplest form of it, the single channel analyzer (SCA). The SCA consists of two electronic thresholds [65]:

- the lower level discriminator (LLD). Pulses are allowed to pass only if their amplitude is above a threshold voltage H_1. Otherwise, the pulse is blocked.

- The upper level discriminator (ULD). Pulses are now allowed to pass only if their amplitude is below a threshold voltage H_2, or blocked otherwise.

The voltage region where the pulses are allowed to pass is called the *window* (Fig. 3.7). For every pulse that passes, the SCA produces a logic output pulse.

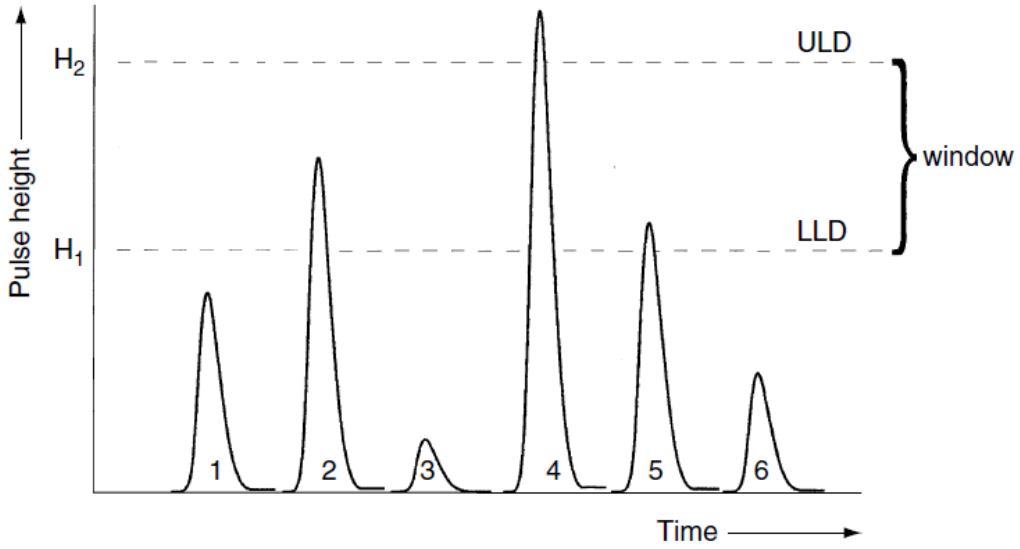

Figure 3.7: A SCA with upper and lower discriminator levels, defining a window [65].

Now assume that the voltage-energy window is small enough. By gradually moving it across the energy range, we could obtain a spectrum, but at considerable cost in terms of time of measurement. It is necessary that a system should be able to monitor a large number of windows simultaneously. The solution to this is a device called: the *analogue to digital converter* (ADC), which is described below.

3.5.5 The Analogue-to-Digital converter (ADC)

As its name states, the ADC is a device which converts an analogue signal to a digital one. It is a fundamental link between analogue and digital electronics.

ADC's are of two types:

- peak-sensing

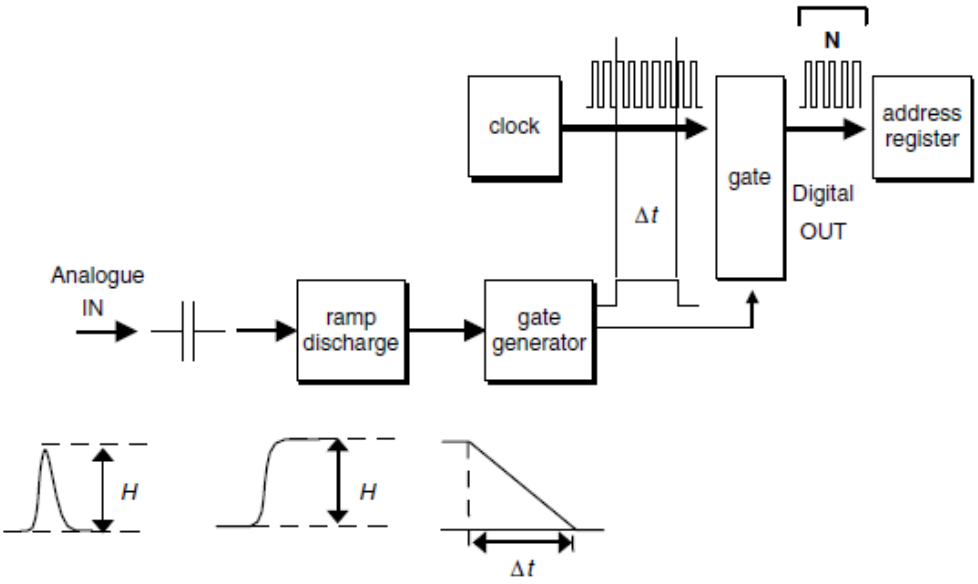

Figure 3.8: Block diagram of a Wilkinson ADC [65].

- charge sensitive

In the peak-sensing ADC's, a maximum of a voltage signal is digitized, while in charge sensitive ADC's it is the total integrated current. The latter is used with current-generating devices, e.g. a PM in current mode (fast detectors). Peak-sensing, on the other hand, is used with slower signals which have already being integrated, e.g. a PM in a voltage mode. The time of integration or the time period over which an ADC seeks a maximum is usually determined by the width of a gate signal.

Conventional analogue MCA systems use on of two types of ADC: the *Wilkinson ADC* and the *Successive approximation ADC*. There is also a third type called *Flash ADC*, but is used in digital signal processing systems. Fig. 3.8 depicts the operational schematics of a Wilkinson ADC. The pulse height measurement proceeds as:

- A capacitor is charged as the analogue pulse rises above a threshold. When the pulse reaches its maximum voltage H, that voltage is retained on the capacitor.

- The capacitor then begins to discharge linearly. At the same time, a timing gate is opened. When the capacitor's voltage reaches zero, that gate is closed. Because of the linearity of the ramp discharge, the time taken to fall to zero will be proportional to the voltage and then to the gamma-ray energy. In effect, the height of the input pulse has been converted to time.

- This time is measured by a high frequency pulse stream, generated by a crystal control clock, which passes through the timing gate. The pulse stream is blocked until the gate opens, at which point a register starts to count the pulses, stopping when the gate is closed. The number of pulses passing through the gate is proportional to the height of the input pulse. Thus, the analogue pulse height has been converted to a digital number.

The most important feature of an ADC is its resolution. It represents the total number of available channels that an ADC can provide. The greater the number of channels, the better is the analog to digital conversion of the signal, which leads to a better resolution.

3.5.6 The Time-to-Amplitude converter (TAC)

In many nuclear physics experiments, especially in nuclear structure, one has to deal with events coming in coincidence. Such events are important for establishing level schemes, performing angular correlation measurements in cascades of γ-rays and reducing the number of background events. Coincidence requires that a time window should be set, where events within or without are considered or rejected for further analysis.

A time period between two logical pulses can be converted into a pulse using the time–to–amplitude converter (TAC) [62]. The amplitude of the pulse is proportional to its duration. This pulse can be further analyzed using an

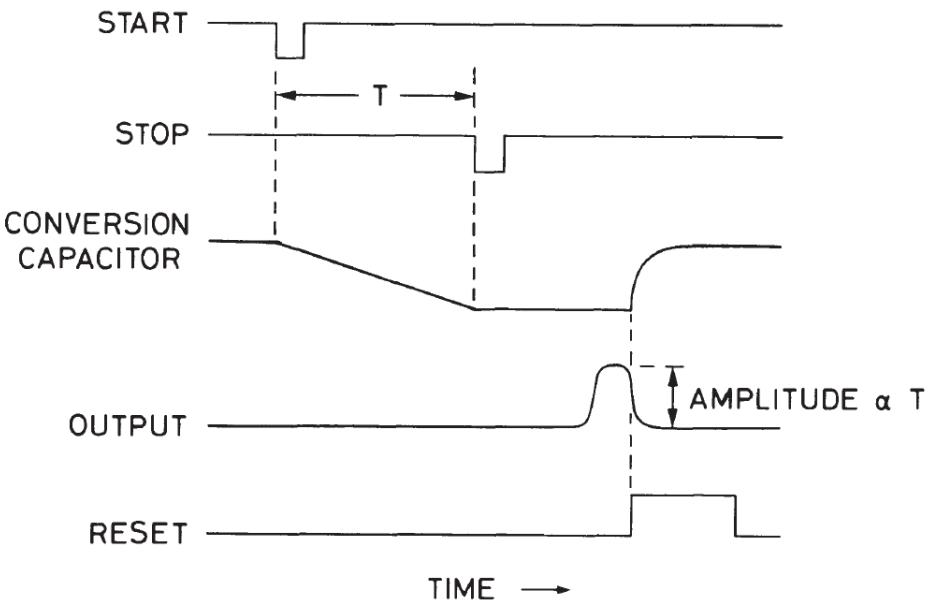

Figure 3.9: Operation of a TDC unit [62].

MCA, giving a spectrum as a function of time intervals. The pulse can be further digitized using an ADC. Such units are called time–to–digital converters (TDC).

The operation of a TDC is shown in Fig. 3.9. The time interval is measured by defining a START signal triggering the beginning of the interval and a STOP signal marking the end of the time interval. This can be simply done by beginning a constant discharge of a capacitor at the arrival of the START signal and to cut off the discharge when the STOP signal arrives. Then, the total charge collected is proportional to the time difference between the START and the STOP signals. More details about TDCs can be found in [62].

3.6 Target Preparation

3.6.1 Ba target preparation

The manufacturing of the ^{nat}Ba target in metallic form presents important difficulties, as it is a material that oxidizes extremely fast. Therefore, as it is

illustrated in Fig. 3.10, a gold–sandwiched ^{nat}Ba target was prepared in the Target Preparation Laboratory of IFIN–HH [66].

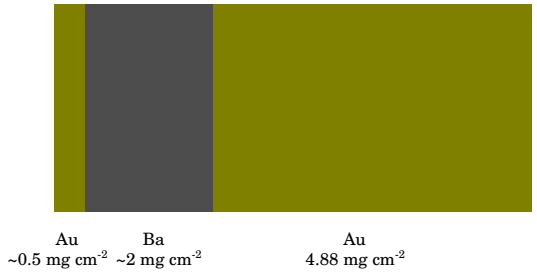

(a) A schematic layout of the target

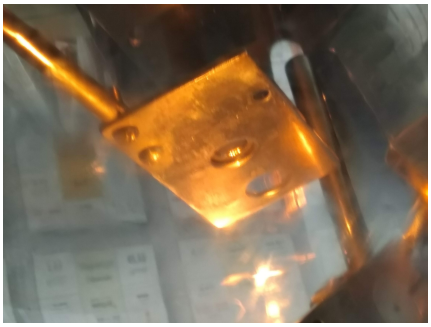

(b) Second stage of Au evaporation

Figure 3.10: Target layout in scale (left) and a picture during the evaporation procedure (right).

The target exhibits the following structure: Au (4.88 mg cm^{-2}) / ^{nat}Ba (2 mg cm^{-2}) / Au (0.5 mg cm^{-2}). The metallic ^{nat}Ba layer (abundance of ^{138}Ba = 71.7%) was obtained through the metalothermic reduction reaction of $BaCO_3$ with La metal powder as reducing agent. For this purpose about double the stoichiometric amount of La metal powder was thoroughly ground with the calculated amount of $BaCO_3$, in an agate mortar set. The resulted mixture was pressed into a pellet, which was inserted into a pinhole tantalum boat. Both ends of the boat were fixed to the high current electrodes of the Quorum technologies E6700 bench top evaporator device. The gold foil of 4.88 mg cm^{-2} thickness, prepared in advance by rolling, was glued to the target frame and placed 4 cm above the tantalum boat in the evaporator. After a high vacuum of 3.5×10^{-5} mbar was reached, a low current was applied through the tantalum boat to degassing of CO_2 resulted from the thermal decomposition of $BaCO_3$. Therefore, the current through the tantalum boat was slightly increased until the reduction temperature was reached.

The evaporation process was carried out until the desired thickness was obtained. The obtained ^{nat}Ba layer was covered with a thin gold layer of 0.5 mg cm^{-2} without breaking the vacuum, to protect the metallic ^{nat}Ba against oxidation. This deposition was made with a tungsten basket, fixed at 9 cm

distance above the substrate. (see Fig. 3.10).

The determination of the thick gold backing was done by weighing, while the other two layers were determined by calculating the thickness from the initial amount of the substance used.

3.6.2 Ta target

A 5 mg cm^{-2} metallic Ta target was also used in this work. The natural abundance of ^{181}Ta is 99.99% [20], making it an ideal target for nuclear structure studies, as it is contains almost only one isotope. The target is not easily oxidized, in contrast to the previously described Ba target, so oxygen contamination is not an issue in this case. A picture of the target is shown in Fig. 3.11 showing its characteristics and its thickness.

(a) A schematic layout of the target

(b) Second stage of Au evaporation

Figure 3.11: Picture of the metallic Ta target along with its characteristics (left) and a picture the same target mounted on the target chamber of ROSPHERE (right).

Chapter 4

Analysis and results

Part 1: The case of ^{180}Hf

In this chapter, the analysis of $\gamma\gamma$ angular correlation measurements for the observed γ-cascades in ^{180}Hf is presented. The ground-state band up to the 1084 keV level, the side-band levels of 1370 keV (band 6), 1374 keV (band 2) and non-band levels 1821 keV, 1608 keV have been populated using the reaction ^{181}Ta(^{11}B,^{12}C)^{180}Hf, at 47 MeV beam energy (see the relevant level scheme in Chapter 1).

The spins, parities and mixing ratios have been measured in this work for the mentioned states. The ground-state spins and parities are confirmed for the measurements for the ground state band levels, except for the 309 $\rightarrow$ 93 $\rightarrow$ 0 cascade, where the possible reasons for this deviation are discussed in the relevant section. Mixing ratios for the corresponding transitions are also measured. Furthermore, a more precise measurement for the spin-parity of the 1374 band 2 level is proposed, which settles a previous disagreement between [24] and [25]. A new value for the mixing ratio of the transition 1374 $\rightarrow$ 309 is suggested which agrees with the previous measurement in [24] and is more precise by about 60%.

Measurements for spins-parities and mixing ratios are presented for the rest

of the previously mentioned side-band and non-band states, and mixing ratio values for the transitions 1370 → 309, 1821 → 1200 keV and 1608 → 1200 keV transitions are reported for the first time. For the cases where the statistics is not sufficient, all possible values for spins-parities and mixing ratios are presented.

In the following, the analysis of the $\gamma\gamma$ angular correlations is discussed, by beginning from the data sorting. The sorting of the data in terms of event folding and relative detector angles is performed using the GASPware analysis software [64]. After the sorting, the efficiency and geometrical corrections are implemented. Then, the measurements of the spins-parities and mixing ratios are performed by comparing the experimental data with all possible theoretical calculations using two methods [36]. The calculations which best describe the experimental data are then adopted as the measured values for these quantities.

4.1 Data sorting

4.1.1 Sorting in terms of the event folding

A total of 7×10^8 events were collected during the three-day run time of the experiment. These events were then sorted in terms of their fold number. Depending on the multiplicity of the reaction, one can separate unwanted events of higher or lower multiplicity, which results in a significantly reduced beam-induced background.

The event-fold histogram for the present experiment is shown Fig. 4.1. 3-fold and 4-fold events are the largest fraction of the total statistics. By applying various gate conditions, one can clear out a significant number of unwanted events. In the present case, most background events come from the fusion evaporation reactions ^{181}Ta(^{11}B,4n)^{188}Pt and ^{181}Ta(^{11}B,3n)^{189}Pt. Because such reactions tend to populate the product nucleus in higher excited

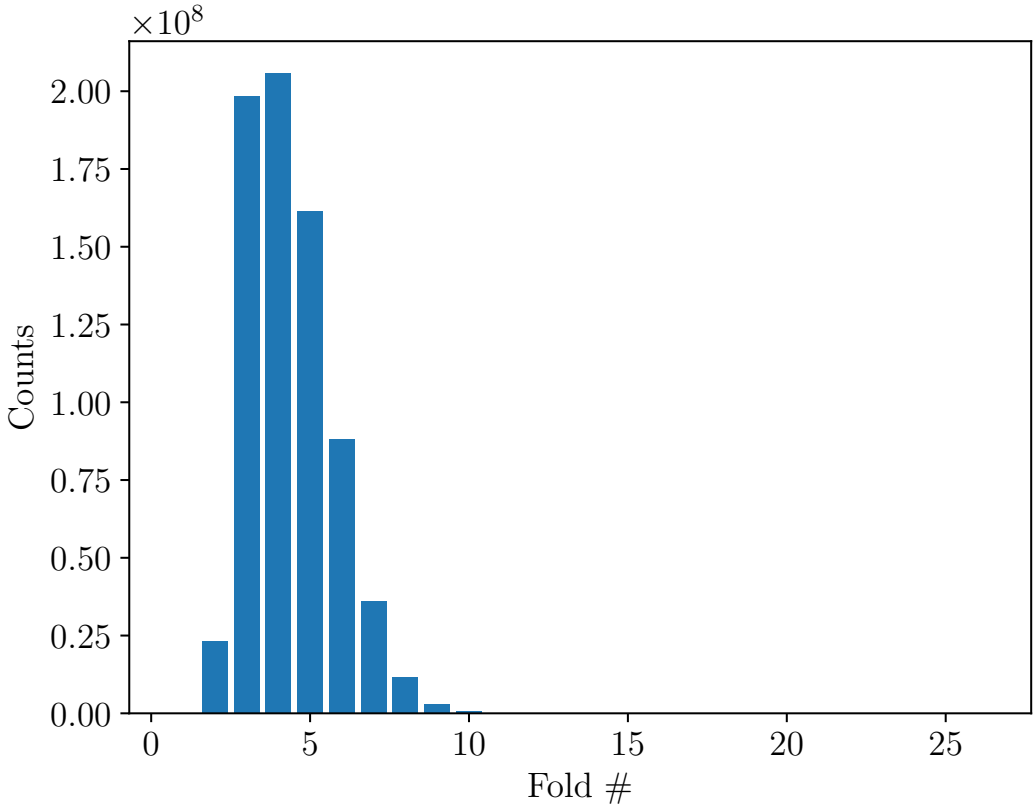

Figure 4.1: Histogram showing the events acquired in ROSPHERE, in terms of their multiplicity. Dismissing events with fold number greater than 3, reduces the background coming from high-multiplicity reactions, e.g. fusion evaporation.

states near the continuum, they have generally higher multiplicity compared to transfer reactions. A comparison can be shown in Fig. 4.2, where the total projection of a symmetric $\gamma\gamma$ matrix is shown for the 3-fold and 4-fold events. It is clear that events coming from the fusion are suppressed in the 3-fold case.

Based on the multiplicity considerations above, the 3-fold events are definitely more suitable for the present analysis. These events have been sorted into three dimensional cubes with the relative angle as the index number.

4.1.2 Sorting in terms of the relative angle

The ROSPHERE array is mounting 25 HPGe detectors in the present setup (see Appendix B for details about the geometry of the array). These detectors can be combined in pairs with specific relative angles, allowing the analysis

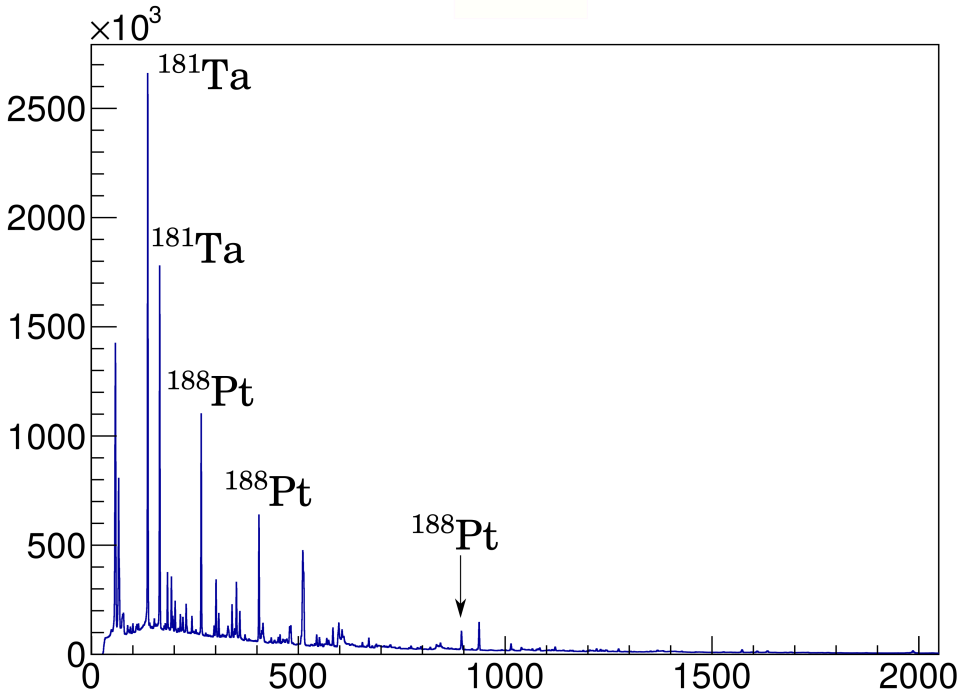

(a)

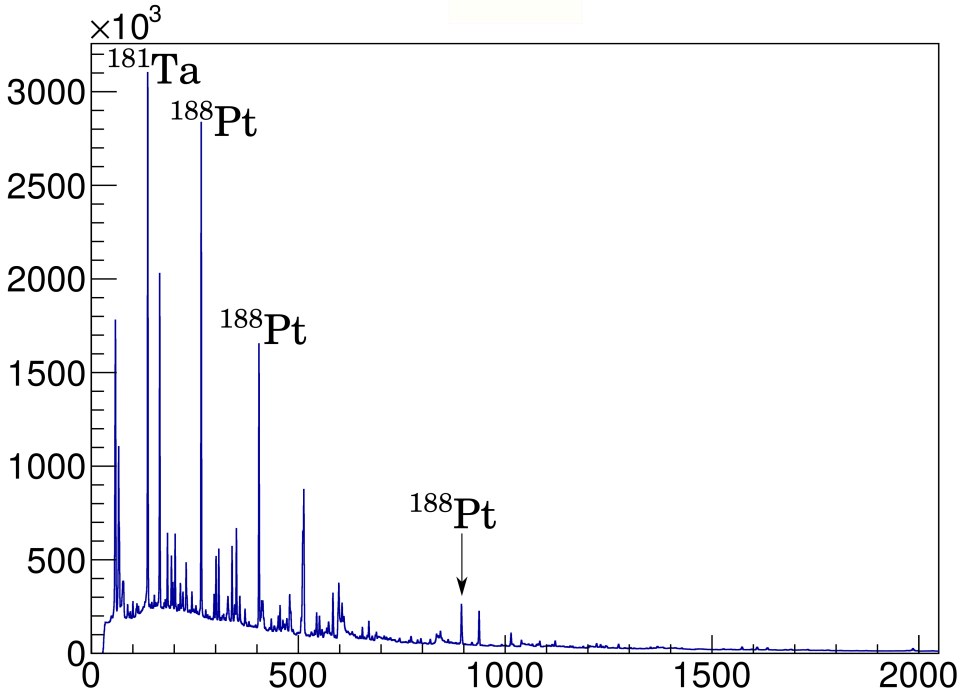

(b)

Figure 4.2: Total projections of symmetric $\gamma\gamma$ matrices of the three-fold events (a) and four-fold events (b). The relative strength of the peaks coming from fusion-evaporation reactions (e.g. ^{188}Pt) is significantly ($\sim 60\%$) reduced in the three-fold case.

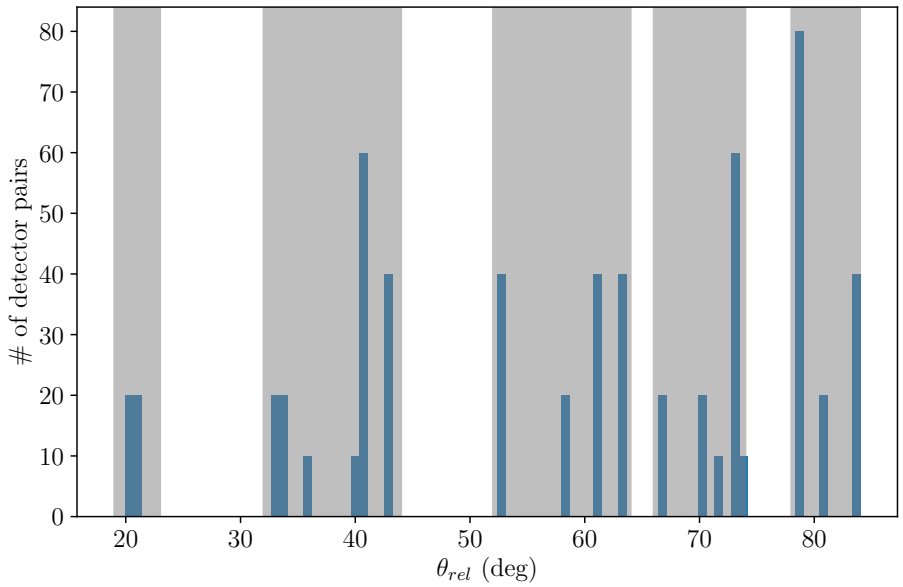

Figure 4.3: Histogram displaying the number of detector pairs in terms of their relative angle for the ROSPHERE array. The shaded areas correspond to the grouping of close angles. The weighted averages of the groups correspond to the relative angles tabulated in Table 4.1.

of $\gamma\gamma$ angular correlations. The 600 possible pairs of detectors with a specific relative angle are then grouped together in 5 relative angles below 90°. This is sufficient, as the angular correlation function:

$$W(\theta) = A_0 \left[1 + a_2 P_2(\cos\theta) + a_4 P_4(\cos\theta)\right] \tag{4.1}$$

is symmetric with respect to $\theta = 90°$. In Eq. 4.1, A_0 is a normalization factor and a_2, a_4 are coefficients that depend on the spins and multipolarities of the states and transitions involved in the cascade of the two γ-rays.

Once the events were sorted into three-dimensional angular correlation cubes, the events can be projected to two-dimensional $\gamma\gamma$ matrices for detectors firing in coincidence at a specific relative angle. The number of pairs at a specific relative angle is shown in Table 4.1 and in Fig. 4.3

Relative angle	No. of pairs
21	40
40	160
60	140
72	120
81	140

Table 4.1: Table showing the number of pairs of HPGe detectors firing in coincidence at a specific relative angle below 90°.

4.1.3 Spectra

After the sorting of the 3-fold data into angular correlation cubes, one can measure the coincident counts between two correlated γ-rays. The ground-state band of the nucleus ^{180}Hf is sufficiently populated up to the 8^+ state. Several side-bands are populated sufficiently to allow angular correlation measurements, including the 1374 keV state in band 2, the 1370 keV state in band 6 and the 1821 and 1608 keV non-band levels. An example is shown in Fig. 4.4, where the 1821 keV transition is depopulated to the 1374 band 2 level and to the 1200 keV 2_3^+ state.

4.1.4 Efficiency Correction

The detector efficiencies have been determined for all 25 HPGe detectors of the current setup of ROSPHERE. The determination of the efficiency curves of the detectors is important, as they should be used for the correction of the relative intensities of the γ-rays measured in each relative angle. The efficiencies are shown below, fitted with a function of the form [67]:

$$\epsilon = 10^{a_0 + a_1 \log(E_\gamma) + a_2 \log^2(E_\gamma)} \tag{4.2}$$

Two ^{152}Eu sources have been used both before and after the experiment.

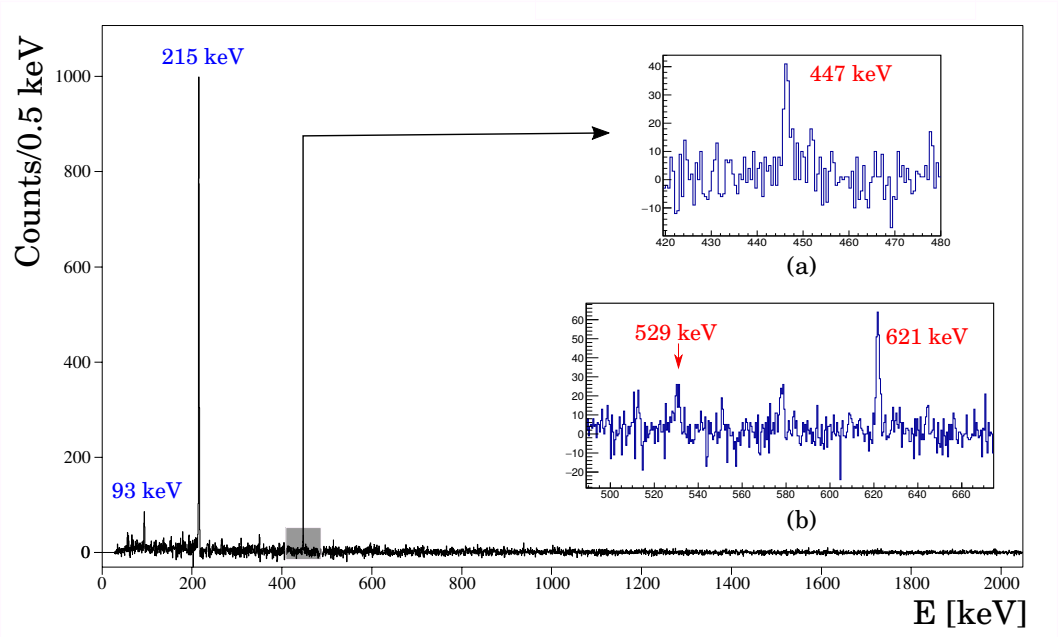

Figure 4.4: Spectrum gated in the 1066 keV transition depopulating the 1374 band 2 level. The 447 transition depopulating the 1821 keV non-band level is shown in inset (a). In inset (b), part of the spectrum gated in 1200 keV shows the same level depopulated by the 621 keV transition to the 1200 keV 2_3^+ state.

The total statistics for each HPGe detector is shown below.

The efficiency correction can be implemented in the angular correlations after the data sorting. The efficiency ϵ_{bin} of the bin of a $\gamma\gamma$ matrix where two γ-rays of energies $E_{\gamma 1}$ and $E_{\gamma 2}$, detected on detector i and detector j respectively, will be given by the relation:

$$\epsilon_{bin} = \frac{1}{2} \sum_{i,j} [\epsilon_i(E_{\gamma 1})\epsilon_j(E_{\gamma 2}) + \epsilon_i(E_{\gamma 2})\epsilon_j(E_{\gamma 1})] \tag{4.3}$$

where the 1/2 factor prevents the double counting of the efficiencies of two detectors.

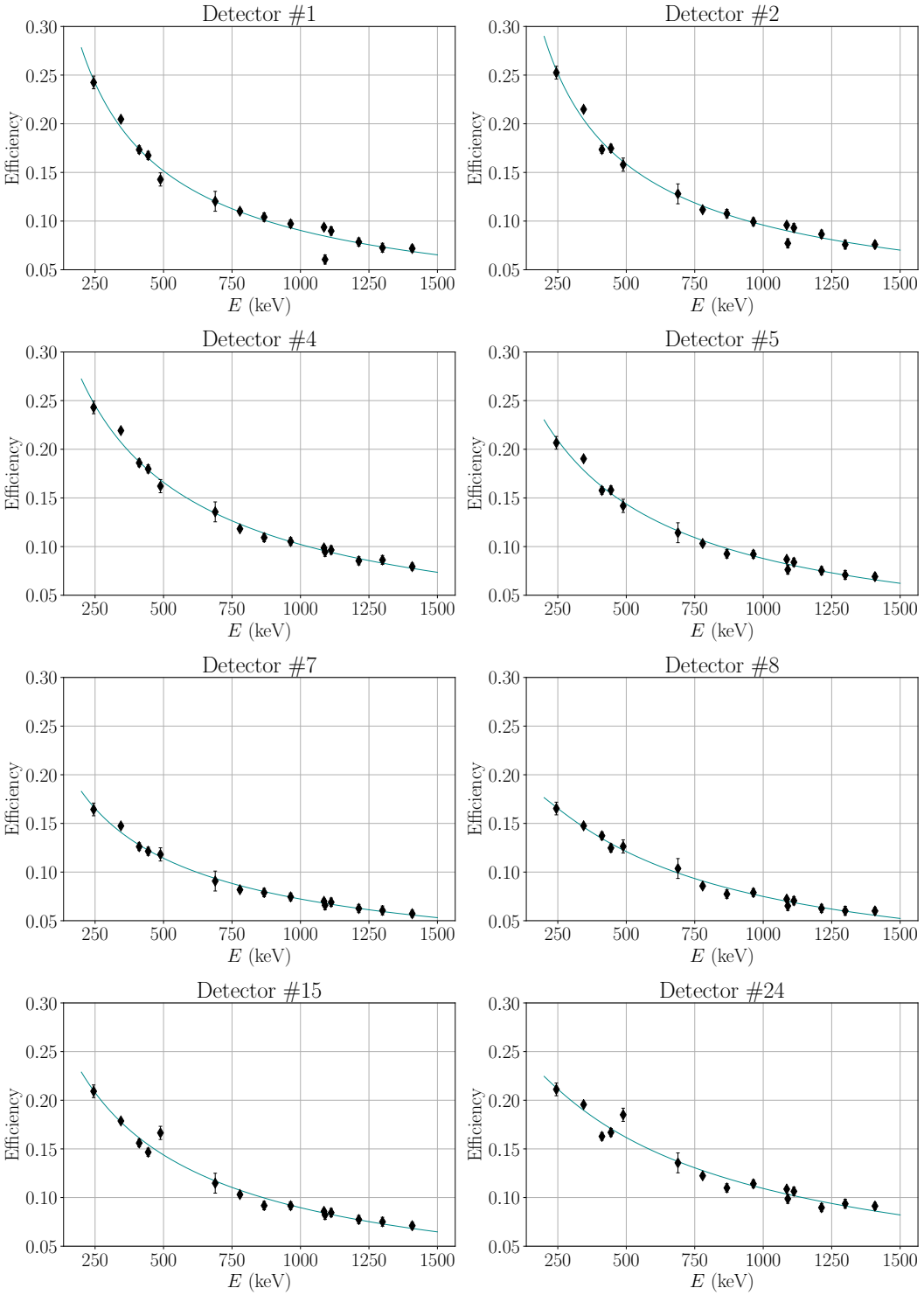

Figure 4.5: Efficiencies of eight (8) out of twenty five (25) HPGe detectors measured by placing a ^{152}Eu source, before the experiment. The rest of the detectors show similar behavior.

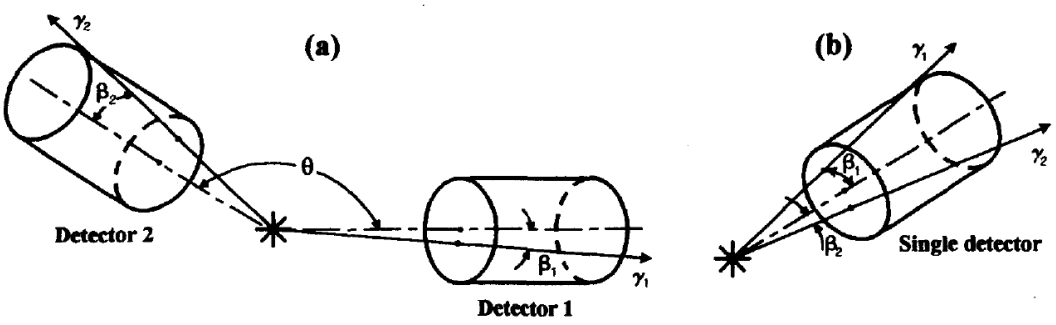

Figure 4.6: Illustration of two γ rays traversing (a) two HPGe detectors and (b) one HPGe detector [68].

4.1.5 Geometrical Corrections

The finite size of the detectors is affecting the measured angular correlation measurements. The angular correlation function of the form of Eq. 4.1 holds under the assumption of point-sized detectors. The effect of the detectors' dimensions should be incorporated in the angular correlation function, in order to determine spins and mixing ratios with significant accuracy. Fig. 4.6 illustrates the effect of two γ-rays traversing finite-size HPGe detectors. Instead of Eq. 4.1, the *effective* angular correlation function:

$$W(\theta) = A_0[Q_2^i Q_2^j a_2 P_2(\cos\theta) + Q_4^i Q_4^j a_4 P_4(\cos\theta)] \tag{4.4}$$

is determined experimentally. In Eq. 4.4, Q_k are the geometrical *attenuation* factors or coefficients corresponding to a specific HPGe detector. These geometrical attenuation coefficients can be determined analytically, depending on the geometry of each detector's crystal and are defined as [69]:

$$Q_k = \frac{J_k}{J_0} \tag{4.5}$$

where J_k is given by the relations:

$$J_2^i = \int_0^{\beta_i^{max}} d\beta_i \sin\beta_i P_k(\cos\beta_i)\epsilon_i(\beta_i) \tag{4.6}$$

$$J_4^j = \int_0^{\beta_j^{max}} d\beta_j \sin\beta_j P_k(\cos\beta_j)\epsilon_j(\beta_j) \tag{4.7}$$

where β is the incident angle of the γ-ray with respect to the detector axis and ϵ are the detector efficiencies for γ-rays incident on the detector within

a solid angle around the incidence angle β, which are also functions of the γ-ray energies. The subscripts 2 and 4 correspond to the attenuation factor multiplying the relevant legendre polynomial in Eq. 4.4 and the superscripts i, j correspond to the detector pair on which the angular correlation is measured, as illustrated in Fig. 4.6. A Python [70] code has been developed base on Krane's formalism [69] in order to incorporate appropriate corrections for the ROSPHERE array [55] featuring coaxial geometry. In Fig. 4.7, the energy dependence of 8 (out of 25) detectors of the ROSPHERE is shown.

While the corrections are considerably small for some detectors, e.g. for detector #3, in general these corrections should be implemented, especially for the corrections of the a_4 coefficient in the angular correlation function, which can be corrected for up to 10% for some detectors, e.g. detector #25.

4.2 Analysis methods

4.2.1 Method A

In the particular method, one determines the experimental angular correlation of two γ-rays involved in a cascade:

$$J_3 \xrightarrow{\gamma_2} J_2 \xrightarrow{\gamma_1} J_1 \tag{4.8}$$

by performing a least-squares fit in the experimental data points. The coefficients a_2^{exp} and a_4^{exp} are then determined from the effective angular correlation function:

$$W_{exp} = A_0 \left[1 + Q_{22} a_2^{exp} P_2(\cos\theta) + Q_{44} a_4^{exp} P_4(\cos\theta)\right] \tag{4.9}$$

where A_0 is a normalization factor and Q_{22}, Q_{44} are the geometrical correction arising from the finite dimensions of the detectors (see Eq. 4.4). Then, the following function can be formed:

$$S^2 = \sum_i \left[\frac{W_{exp}(\theta^i) - W_{th}(\delta, \theta^i)}{\sigma_w^i}\right]^2 \tag{4.10}$$

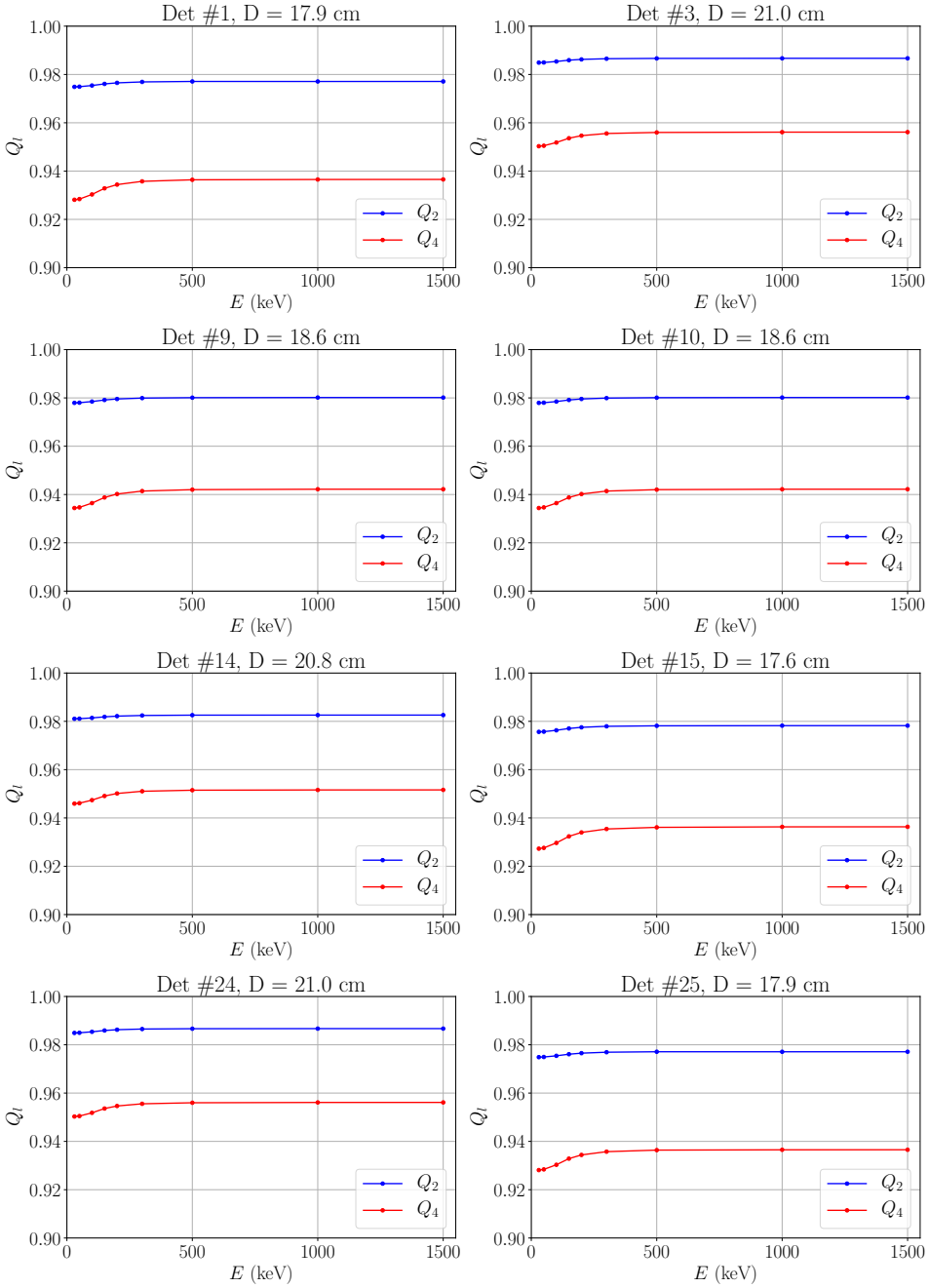

Figure 4.7: Typical behavior of the geometrical attenuation coefficients for eight (8) out of twenty five (25) HPGe detectors of ROSPHERE as a function of γ energy.

for every possible value of the mixing ratio of the two lowest multipolarities δ. If J_1, J_2 and $\delta_{\gamma 1}$ are known, then one can find the solution for the values of J_3 and $\delta_{\gamma 2}$. Eq. 4.10 is a measure of the squared distance of the experimental and the theoretical angular correlation function. The mixing ratio $\delta_{\gamma 2}$ for the transition γ_2 can then be obtained by minimizing the S^2 function with respect to the mixing ratio $\delta_{\gamma 2}$. For well-known confidence limits, which are derived from statistical tables for the χ^2 distribution, one can estimate the possible values of spins of the studied cascade. The mixing ratio is then obtained by the minimum of the curve in an $S^2 - \tan^{-1}\delta$ plot and the error can be found from limits of S^2 function given by the relation [36, 71]:

$$S^2_{lim} = S^2_{min} + 1 \tag{4.11}$$

4.2.2 Method B

In this method, a least-squares fit is performed in the experimental angular correlation in order to find the experimental coefficients a_2 and a_4 and their uncertainties. The comparison with theoretical calculation then proceeds by plotting the experimental a_2 and a_4 along with theoretical calculations. Assuming that the studied cascade is of the form of Eq. 4.8, then for known J_2, J_1 and $\delta(\gamma_1)$, the various choices for J_3 and $\delta(\gamma_2)$ appear in an $a_2 - a_4$ diagram as separate ellipses. The experimental result together with its uncertainty forms also an ellipse, with semi-axis lengths the corresponding uncertainties δa_2 and δa_4. If the experimental ellipse is overlapping with any theoretical ellipse, then the spin it represents is a possible solution for J_3. The mixing ratio $\delta(\gamma_2)$ is obtained by the closest theoretical point, while the uncertainty is found from the intersection points of the experimental and theoretical ellipse.

There are some weaknesses of this method reported in [36], especially when considering the estimation of the uncertainty in the mixing ratio in the $a_2 - a_4$ plane, which can lead to highly precise measurements of the mixing ratio while having poor counting statistics and the opposite. However, the analysis

has been performed with the particular method, together with Method A, for comparison and completeness. The results are presented in the next section.

4.3 Results and theoretical calculations

In this section, the results for the measured spins and mixing ratios are presented. All theoretical calculations have been performed using the Angular Correlation Calculator [72]. Mixing ratios of the two lowest multipolarities are considered. For example, O/Q would mean octupole ($L = 3$) with respect to quadrupole ($L = 2$) radiation while Q/D would mean quadrupole ($L = 2$) to dipole ($L = 1$) radiation.

4.3.1 Ground-state band levels

The 309 g.s. band level

The 309 keV g.s. band level is depopulated by the 215 keV transition to the 93 keV state 2_1^+ state. The latter is depopulated by a "streched" $E2$ transition to the ground state. However, lifetime of the particular state (1.519(10) ns) is rather long for obtaining a reliable result using the angular correlation method. Nevertheless, the geometrically corrected experimental angular distribution coefficients are found to be $a_2 = -0.09 \pm 0.05$ and $a_4 = -0.13 \pm 0.08$. The results are tabulated in Table 4.2 and plotted in Fig. 4.8. Both methods

Table 4.2: Table showing the experimental results with methods A and B for the 309 g.s band state. For a possible spin value, the mixing ratio of the two lowest multipolarities is always considered.

Spin	Mixing (A)	Parity (A)	Mixing (B)	Parity (B)
4	$3.35^{+4.79}_{-1.47}$ (O/Q)	−	$3.54^{+N/A}_{-2.3}$ (O/Q)	−
3	$6.78^{+7.53}_{-3.05}$ (Q/D)	+	$7.04^{+N/A}_{-4.4}$ (Q/D)	+
2	$0.41^{+0.25}_{-0.23}$ (Q/D)	±	$0.43^{+0.29}_{-0.36}$ (Q/D)	±

show that the 309 keV state of the ground state rotational band is not 4 but 3. However, such a conclusion seems contradictory with the energy spacings between the ground state and the 93 keV state and the 309 keV state, which indicate that the spin value should be 4^+ (rotational band). The reason for this inconsistency in the experimental results may be attributed to either the long

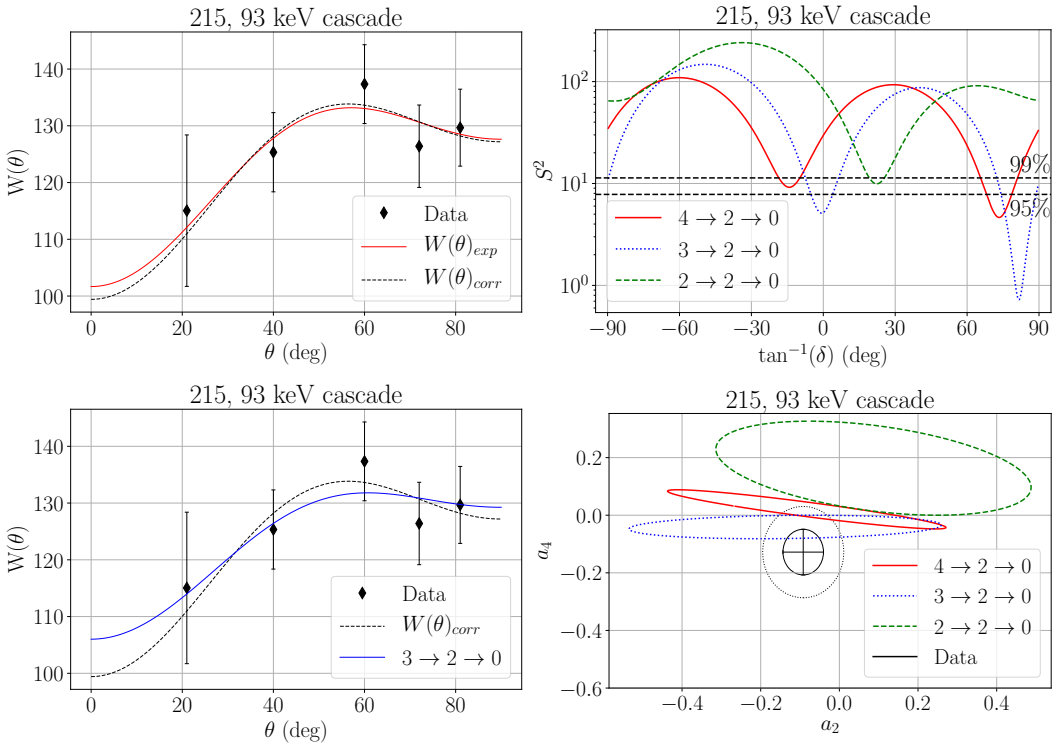

Figure 4.8: Angular correlation of the 215-93 keV cascade (upper left). The red line represents the experimental angular correlation as measured, while the black dashed line represents the angular correlation incorporated with the geometrical corrections due to the finite dimensions of the detectors. The S^2 function with respect to the cotangent of the mixing ratio δ is shown in the upper right corner (Method A), for various spin sequences, along with the 95% and 99% confidence limits. A comparison of the corrected angular correlation with the best fitted theoretical calculation is shown in the lower left and parametric plots for different spin sequences as a function of the mixing ratio δ is shown on the lower right corner (Method B).

lifetime of the intermediate state or counting discrepancies due to low energy of the 93 keV transition, arising for the low-level discriminator settings. In the next analysis to follow, this measurement will be ignored and the transition from 309 keV to 93 keV will be considered a pure $E2$ transition.

The 640 keV g.s. band level

The 640 keV g.s. band level is depopulated to the 309 keV level by emitting a photon of $E_\gamma = 332$ keV. By knowing the spins of the 309 keV (4^+) and of the 93 keV first excited state (2^+), and assuming that the transition 309 $\rightarrow$ 93 keV is a pure $E2$ transition, one can determine the spin and the mixing ratio of the 640 keV level and the mixing ratio of the transition 640 $\rightarrow$ 309 keV.

The geometrically corrected experimental angular distribution coefficients are found to be $a_2 = 0.08 \pm 0.04$ and $a_4 = 0.05 \pm 0.06$. The respective analysis plots are shown in Fig. 4.9. As seen from these plots, there are two possibilities for

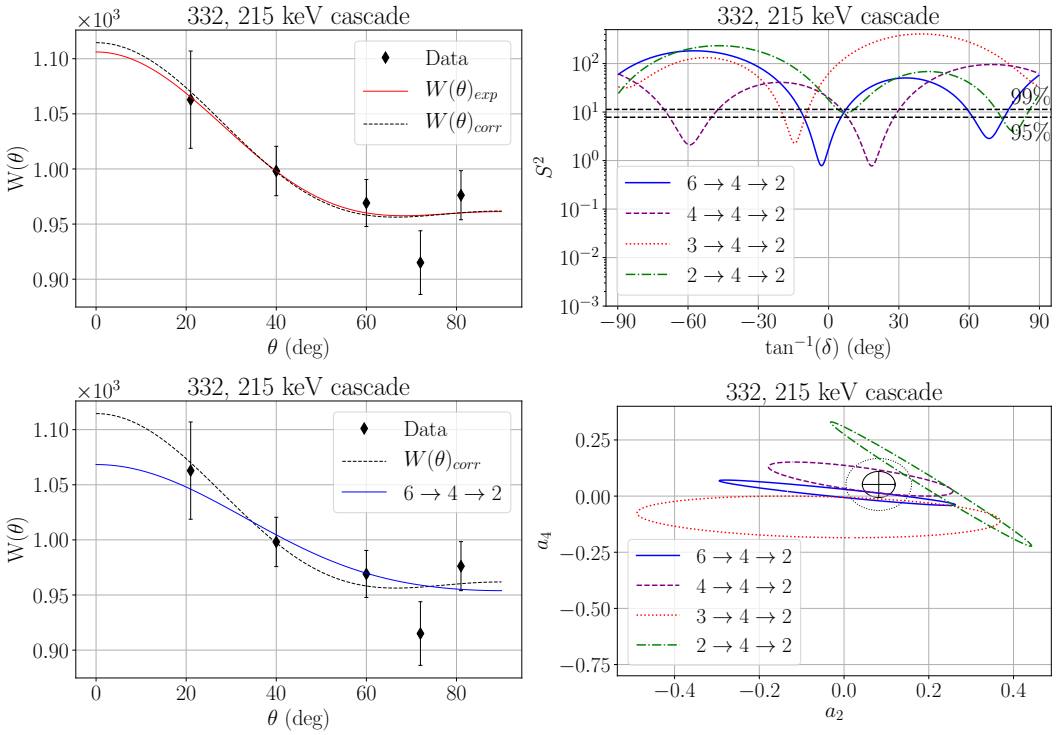

Figure 4.9: Angular correlation of the 332-215 keV cascade (upper left). The red line represents the experimental angular correlation as measured, while the black dashed line represents the angular correlation incorporated with the geometrical corrections due to the finite dimensions of the detectors. The S^2 function with respect to the cotangent of the mixing ratio δ is shown in the upper right corner (Method A), for various spin sequences, along with the 95% and 99% confidence limits. A comparison of the corrected angular correlation with the best fitted theoretical calculation is shown in the lower left and parametric plots for different spin sequences as a function of the mixing ratio δ is shown on the lower right corner (Method B).

the spin of the 640 keV state. An assignment of spin 4 however would require the observation of the transition 640 $\rightarrow$ 93. Such a transition has not been observed in the spectra and is also missing from literature [20]. Thus, the spin value of 6 is favored for the 640 keV state. The octupole to quadrupole mixing ratio can be determined and found from the minimum of the $S^2 - \arctan^{-1}\delta$, which yields a value $\delta = -0.06^{+0.06}_{-0.05}$, while method B yields $\delta = -0.05^{+0.06}_{-0.05}$. The transition is thus almost a pure $E2$, as expected, and is verified that the spin-parity of the 640 keV state is 6^+.

The 1084 keV g.s. band level

The 1084 keV g.s. band level is depopulated to the 640 keV level by emitting a photon of $E_\gamma = 443$ keV. The spins of the 640 keV g.s. band level (6^+) and of the 309 keV excited state (4^+) are established above. The mixing ratio of the $640 \rightarrow 309$ transition is measured as well. With this information known, the spin of the 1084 keV g.s. band and the mixing ratio of the $1084 \rightarrow 640$ keV transition can be measured. The geometrically corrected experimental angular distribution coefficients are found to be $a_2 = 0.13 \pm 0.08$ and $a_4 = 0.04 \pm 0.13$. The respective analysis plots are shown in Fig. 4.10. As seen from the above

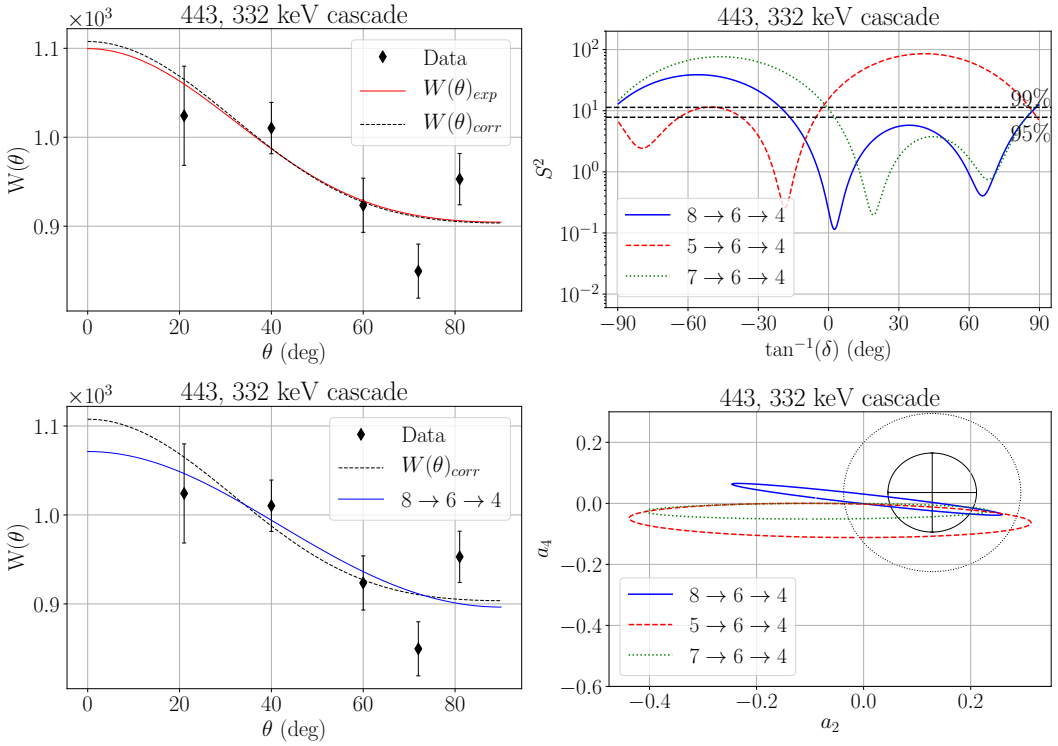

Figure 4.10: Angular correlation of the 443-332 keV cascade (upper left). The red line represents the experimental angular correlation as measured, while the black dashed line represents the angular correlation incorporated with the geometrical corrections due to the finite dimensions of the detectors. The S^2 function with respect to the cotangent of the mixing ratio δ is shown in the upper right corner (Method A), for various spin sequences, along with the 95% and 99% confidence limits. A comparison of the corrected angular correlation with the best fitted theoretical calculation is shown in the lower left and parametric plots for different spin sequences as a function of the mixing ratio δ is shown on the lower right corner (Method B).

plots, there are a few possibilities for the spin of the 1084 keV state. An

assignment of spin 4, 5 or 6 however would require the observation of the transition 1084 $\rightarrow$ 309. Such a transition has not been observed [20]. The value of spin 8 is clearly favored, yielding an octupole to quadrupole mixing $\delta = 0.04^{+0.15}_{-0.13}$ using method A and $\delta = 0.05^{+0.16}_{-0.15}$ using method B. The transition is thus almost a pure $E2$, as expected, and it is verified that the spin-parity of the 1084 keV state is 8^+.

4.3.2 Side-band levels

The 1374 keV Band 2 level

The particular state is assigned a tentative spin of (4^-) from [24]. This result is inconsistent with value of 3^- assigned in [25]. The 1374 keV state is depopulated to the 4^+ of the rotational ground state band. Assuming that the ground state transition $4^+ \rightarrow 2^+$ is a pure $E2$ transition, one can measure the angular correlation and mixing ratio of the 1374 keV state. As seen from the plots the

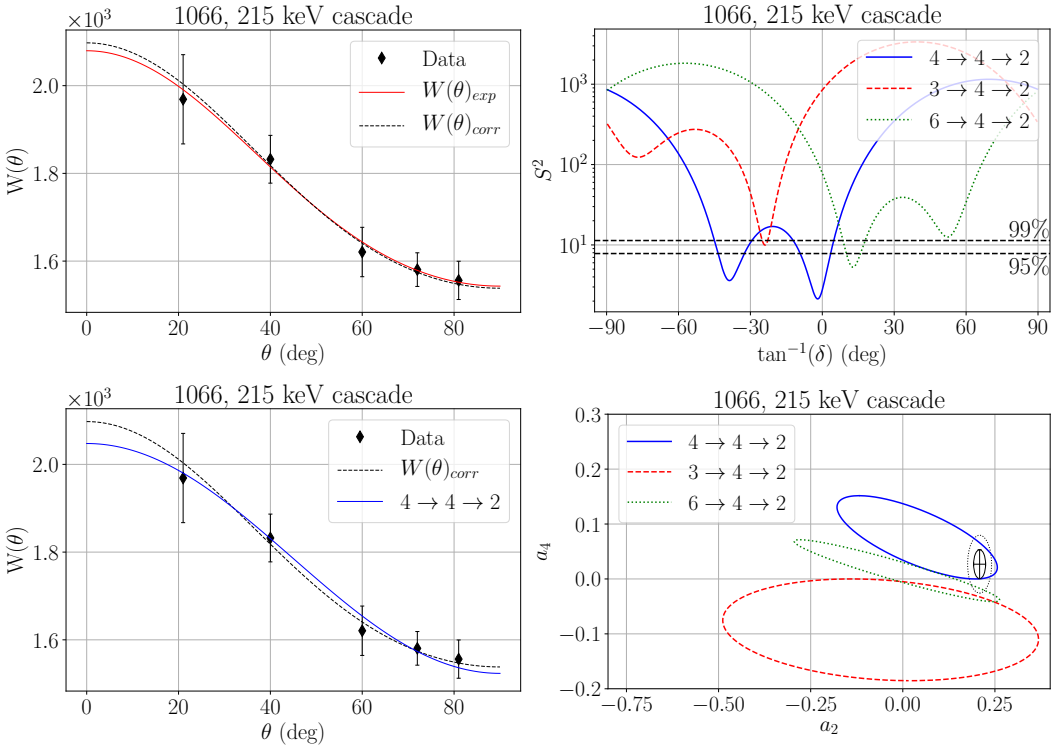

Figure 4.11: Angular correlation of the 1066-215 keV cascade (upper left). The red line represents the experimental angular correlation as measured, while the black dashed line represents the angular correlation incorporated with the geometrical corrections due to the finite dimensions of the detectors. The S^2 function with respect to the cotangent of the mixing ratio δ is shown in the upper right corner (Method A), for various spin sequences, along with the 95% and 99% confidence limits. A comparison of the corrected angular correlation with the best fitted theoretical calculation is shown in the lower left and parametric plots for different spin sequences as a function of the mixing ratio δ is shown on the lower right corner (Method B).

1374 keV state can be assigned with a spin of 4. The corrected experimental values for the coefficients are $a_2 = 0.208 \pm 0.016$ and $a_4 = 0.03 \pm 0.03$. Method

A yields a mixing ratio of quadrupole to dipole $\delta = -0.03^{+0.03}_{-0.05}$ while method B gives a mixing ratio $\delta = -0.04$, but the errors cannot be estimated, as there is only tangential intersection between the theoretical calculations and the 1σ ellipse, as shown in Fig. 4.11. These values agree with the mixing ratio measured in [24] of $-0.12(30)$, and have the additional advantage of being more precise.

The 1370 keV band 6 level

The particular state has a tentative spin-parity assignment of (4^+). The 1370 keV state is depopulated to the 4^+_1 state by emitting a photon of $E_\gamma = 1061$ keV. The angular correlation of the cascade $1370 \rightarrow 309 \rightarrow 93$ is shown in Fig. 4.12. The corrected experimental values for the coefficients are $a_2 = 0.18 \pm 0.25$ and $a_4 = 0.22 \pm 0.36$. The results are tabulated in Table 4.3. For

Table 4.3: Table showing the experimental results with methods A and B for the 1370 band 6 state. For a possible spin value, the mixing ratio of the two lowest multipolarities of always considered.

Spin	Mixing (A)	Parity (A)	Mixing (B)	Parity (B)
4	$-1.3^{+1.8}_{-2.0}$ (Q/D)	+	$-1.2^{+N/A}_{-3.1}$ (Q/D)	+
3	$-0.4^{+0.3}_{-0.3}$ (Q/D)	$\pm$	$-0.4^{+0.2}_{-0.3}$ (Q/D)	$\pm$

the case of spin 4, the upper error limit cannot be derived using method B, as there is not an upper intersection between the 1σ ellipse and the theoretical calculations.

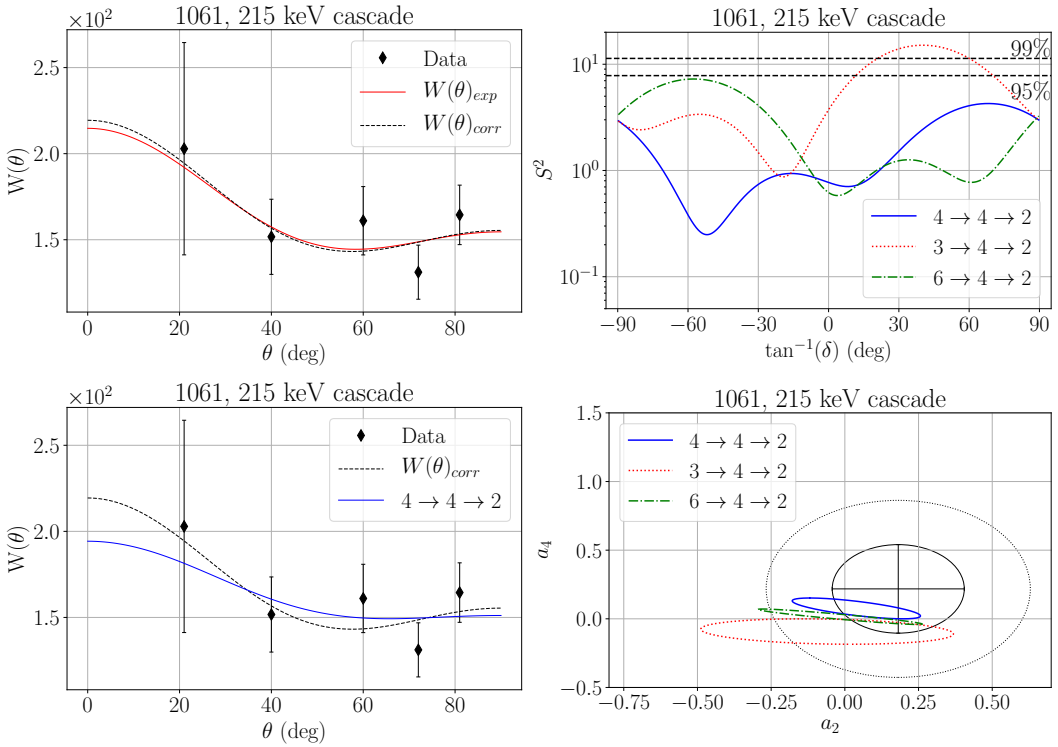

Figure 4.12: Angular correlation of the 1061-215 keV cascade (upper left).The red line represents the experimental angular correlation as measured, while the black dashed line represents the angular correlation incorporated with the geometrical corrections due to the finite dimensions of the detectors. The S^2 function with respect to the cotangent of the mixing ratio δ is shown in the upper right corner (Method A), for various spin sequences, along with the 95% and 99% confidence limits. A comparison of the corrected angular correlation with the best fitted theoretical calculation is shown in the lower left and parametric plots for different spin sequences as a function of the mixing ratio δ is shown on the lower right corner (Method B).

4.3.3 Non-band levels

The 1821 keV non-band level

The 1821 keV non-band level is sufficiently populated in the present experiment to allow a measurement of its spin and possible mixing ratios of the transitions that depopulate it. There is a spin assignment of (3^-), as measured in [24]. The particular transition is depopulated to the 1200 keV (2_3^+) state by emitting a photon of $E_\gamma = 621$ keV. The 2_3^+ state is directly depopulated to the ground state. The measured angular correlation for the cascade of the levels 1821 $\to$ 1200 $\to$ 0 keV is shown in Fig. 4.13 (left). The corrected experimental values for the coefficients are $a_2 = 0.19 \pm 0.06$ and $a_4 = -0.07 \pm 0.10$. The possible

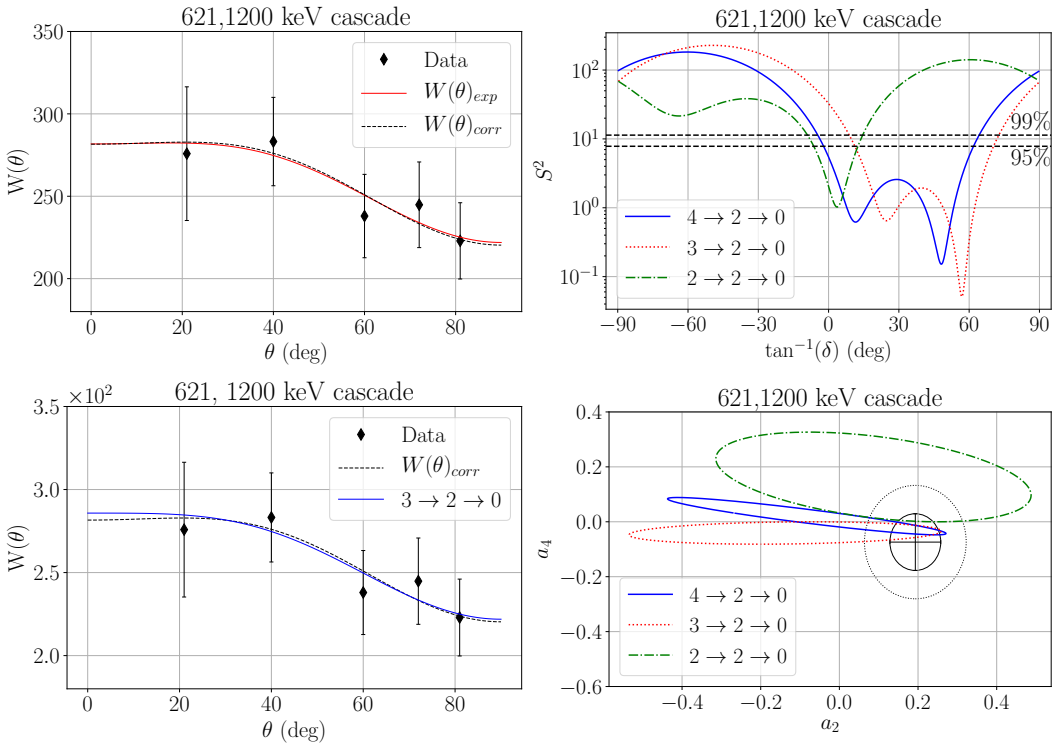

Figure 4.13: Angular correlation of the 621-1200 keV cascade (upper left). The red line represents the experimental angular correlation as measured, while the black dashed line represents the angular correlation incorporated with the geometrical corrections due to the finite dimensions of the detectors. The S^2 function with respect to the cotangent of the mixing ratio δ is shown in the upper right corner (Method A), for various spin sequences, along with the 95% and 99% confidence limits. A comparison of the corrected angular correlation with the best fitted theoretical calculation is shown in the lower left and parametric plots for different spin sequences as a function of the mixing ratio δ is shown on the lower right corner (Method B).

spins and mixing ratios are tabulated in Table 4.4 and shown in Fig. 4.13. The experimental data point for the particular cascade features relatively large

Table 4.4: Table showing the experimental results with methods A and B for the 1821 non-band state. For a possible spin value, the mixing ratio of the two lowest multipolarities of always considered.

Spin	Mixing (A)	Parity (A)	Mixing (B)	Parity (B)
4	$1.1^{+0.3}_{-0.3}$ (O/Q)	−	$1.1^{+0.3}_{-0.4}$ (O/Q)	−
3	$1.5^{+0.4}_{-0.3}$ (Q/D)	+	$1.5^{+0.5}_{-0.6}$ (Q/D)	+

error bars. A spin assignment of 3 agrees with previous measurement in [24]. However, the mixing ratio measurement for the $E_\gamma = 621$ keV favors a mixed

$E2$-$M1$ transition, which can only proceed if the parity of the state is 1821 keV state +. Considering the limited statistics, more precise data are required.

The 1608 keV non-band level

The particular state is assigned a tentative spin of (4)+ from [24]. The 1608 state is depopulated to the 2_3^+ by emitting a photon of $E_\gamma = 408$ keV. The angular correlation of the cascade 1608 $\rightarrow$ 1200 $\rightarrow$ 0 is shown in Fig. 4.14. The corrected experimental values for the coefficients are $a_2 = 0.04 \pm 0.10$ and $a_4 = 0.16 \pm 0.16$. Because there are no transitions from the 1608 keV state directly to the ground state, the spin value of 3 or 4 is favored in the present measurement. Thus, it is suggested that the spin-parity value for the 1608 keV state is 4^+, which agreed with the value in [24]. The results are tabulated in Table 4.5.

Table 4.5: Table showing the experimental results with methods A and B for the 1608 non-band state. For a possible spin value, the mixing ratio of the two lowest multipolarities of always considered. The parity is positive, as the multipolarity of the γ-transition of 408 keV is measured in a previous work [73] as an $E2$.

Spin	Mixing (A)	Parity (A)	Mixing (B)	Parity (B)
4	$-0.13^{+0.12}_{-0.11}$ (O/Q)	+	$-0.11^{+0.09}_{-0.09}$ (O/Q)	+
3	$0.13^{+0.12}_{-0.11}$ (Q/D)	+	$0.14^{+0.04}_{-0.01}$ (Q/D)	+

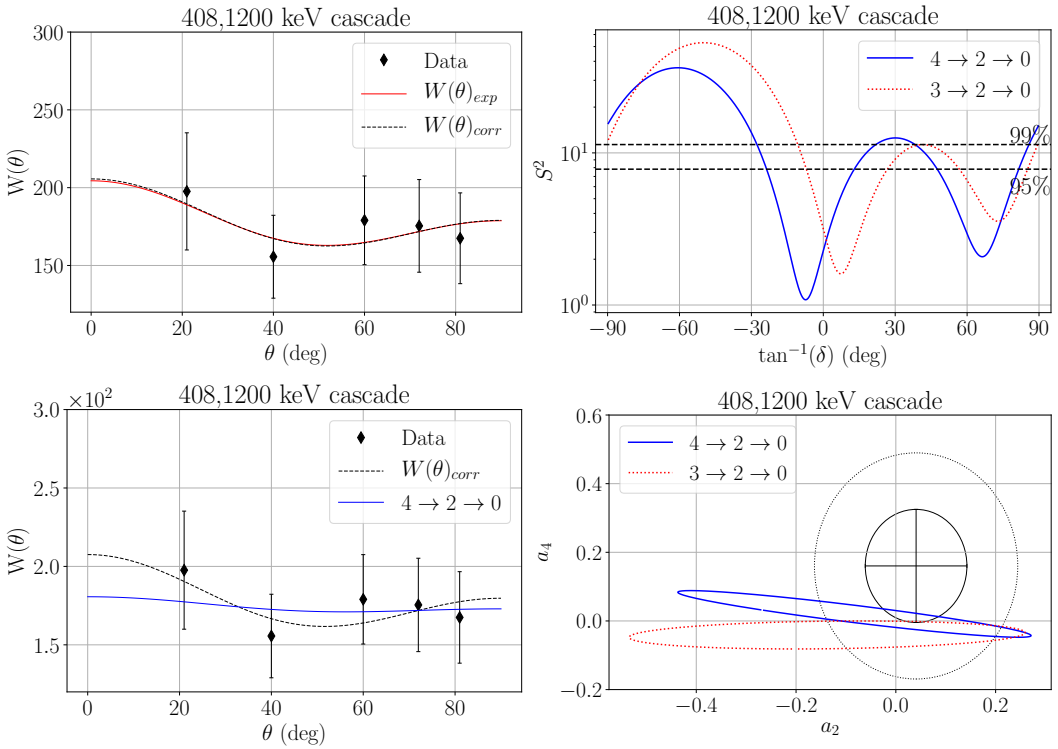

Figure 4.14: Angular correlation of the 408-1200 keV cascade. The red line represents the experimental angular correlation as measured, while the black dashed line represents the angular correlation incorporated with the geometrical corrections due to the finite dimensions of the detectors. The S^2 function with respect to the cotangent of the mixing ratio δ is shown in the upper right corner (Method A), for various spin sequences, along with the 95% and 99% confidence limits. A comparison of the corrected angular correlation with the best fitted theoretical calculation is shown in the lower left and parametric plots for different spin sequences as a function of the mixing ratio δ is shown on the lower right corner (Method B).

4.4 Discussion

The angular correlations of the ground-state band up to the 8^+ state in ^{180}Hf have been measured. The observed correlations agree with the expected spins and parities assigned on the ground-state rotational bands as expected, except for the 309 $\rightarrow$ 93 $\rightarrow$ 0 cascade. There is a difficulty to measure the spin/parity and the mixing ratio of the 309 state using this cascade, as the relatively long lifetime of the 93 keV state is not suitable for an angular correlation measurement. Despite this situation, the transition 309 $\rightarrow$ 93 keV is considered a pure $E2$, which is generally a reasonable assumption in the ground-state band transitions of rotational nuclei. This can be seen also in the rest of the ground-state band transitions. For the case of 640 $\rightarrow$ 309 keV transition, the M3/E2 mixing ratio is found to be $-0.06^{+0.06}_{-0.05}$, while for the case of 1084 $\rightarrow$ 640 keV transition the same mixing ratio is found to be $0.04^{+0.15}_{-0.13}$. These results show the dominance of $E2$ components along the ground-state band.

Spins and mixing ratios of various side-band and non-band levels have been also studied. The 1374 band 2 state can be assigned a definite spin-parity assignment of 4^-, with a quadrupole to dipole mixing ratio equal to $-0.03^{+0.03}_{-0.05}$. The particular measurement settles the previous disagreement in [24] and [25], as a 4^- spin-parity assignment is favored. The mixing ratio result is also more precise than the previously given value in [24]. The 1370 keV band 6 level, spins-parities of $3^\pm$ or 4^+ are possible values. For the case of a spin value of 3, the measured quadrupole to dipole mixing ratio is equal to $-0.4^{+0.3}_{-0.3}$. For the case of a spin 4 assignment, the quadrupole to dipole mixing ratio is measured equal to $-1.4^{+1.8}_{-2.0}$, suggesting an E2-M1 character. The latter assignment agrees with the spin-parity assignment of [24], however one cannot exclude the possibility of a $3^\pm$ with the present data.

The 1821 keV band level measurement suggest as most possible value a spin equal to 3. For this case, the quadrupole to dipole mixing ratio is measured $1.5^{+0.4}_{-0.3}$ suggesting that the transition is also a mixed $E2$-$M1$ transition. Thus

a spin-parity assignment of 3^+ is assigned instead of a (3^-) given by [24]. For the case of the 1608 keV non-band level, the most possible value is a spin-parity of 4^+, with an octupole to quadrupole mixing ratio equal to $-0.13^{+0.12}_{-0.11}$. The possibility of a spin-parity assignment of 3^+ cannot be excluded from the present data.

Chapter 5

Analysis and results

Part 2: The case of ^{140}Ba

An attempt to populate the excited states of interest using the $2n$-transfer reaction ^{138}Ba(^{18}O,^{16}O)^{140}Ba reaction was performed at IFIN–HH [16] using a specially manufactured ^{nat}Ba target sandwiched between two Au layers. This was considered imperative due to Barium's quick oxidation in air. Gamma spectra in four beam energies (61, 63, 65 and 67 MeV) near the Coulomb barrier have been acquired using the Bucharest ROSPHERE array, using 15 HPGe detectors.

Lower limits on the lifetimes of the ground-state band up to the 8^+ state (see the relevant level scheme in Chapter 1) are reported, using the limitations of the Doppler Shift Attenuation Method technique (DSAM) [56, 58]. Furthermore, relative cross sections regarding the $2n$–transfer reaction with respect to the fusion and the total inelastic reaction channels have been also deduced. An attempt to predict the unmeasured cross sections of the ^{138}Ba(^{18}O,^{16}O)^{140}Ba in the studied energy range by relying on the experimental yield and the theoretical calculations for the fusion-evaporation reaction ^{138}Ba(^{18}O,$4n$)^{152}Gd is also presented.

5.1 Spectroscopy

A total of four beam energies have been studied, in order to find the best conditions for the population of the excited states in ^{140}Ba. The lowest beam energy $E(^{18}\mathrm{O}) = 61$ MeV was expected to significantly reduce the beam-induced background coming from the fusion-evaporation reactions:

$$\begin{aligned} {}^{18}\mathrm{O} + {}^{138}\mathrm{Ba} &\rightarrow {}^{152}\mathrm{Gd} + 4n \\ &\rightarrow {}^{153}\mathrm{Gd} + 3n \end{aligned} \tag{5.1}$$

The 602 keV ($2_1^+ \rightarrow 0_{g.s.}^+$) transition of ^{140}Ba was populated, as well as the overlapping transitions $4_1^+ \rightarrow 2_1^+$ and $6_1^+ \rightarrow 4_1^+$. In Fig. 5.1, the projection of the symmetric $\gamma\gamma$–matrix is shown, in the region near the ground-state transition $2_1^+ \rightarrow 0_1^+$ is shown. The overlapping transitions $4_1^+ \rightarrow 2_1^+$ and $6_1^+ \rightarrow 4_1^+$ are also shown in the same figure. The transition $3_1^- \rightarrow 2_1^+$ (1200 keV) is not present in the spectrum.

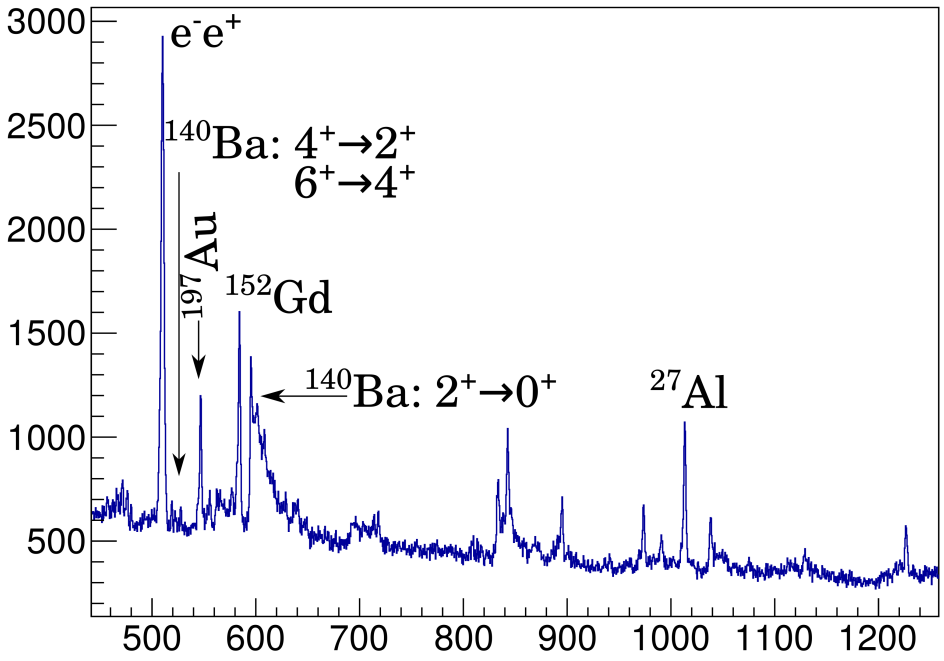

Figure 5.1: Projection of the symmetric matrix for beam energy 61 MeV.

In Fig. 5.2, the projection of the symmetric matrix is shown, for beam energy $E(^{18}\mathrm{O}) = 63$ MeV along with the $\gamma\gamma$–coincidence spectrum gated on the 602 keV transition. By examining the coincidence spectrum (Fig. 5.2b), the transitions tabulated on Table 5.1 have been populated, all belonging to the ground-state band of ^{140}Ba.

Table 5.1: Transitions observed in the coincidence spectra, at 63 and 65 MeV beam energy.

E_γ [keV]	Transition
602.35	$2_1^+ \rightarrow 0_1^+$
528.25	$4_1^+ \rightarrow 2_1^+$
529.7	$6_1^+ \rightarrow 4_1^+$
808.0	$(8_1^+) \rightarrow 6_1^+$

The transition $2_2^+ \rightarrow 2_1^+$ seem to be absent. Absent seem also to be the transition $3^- \rightarrow 2_1^+$. Note that there is a photopeak located at 1204 keV in the projection of the symmetric matrix, but it originates from the reaction ^{74}Ge(n,n'γ)^{74}Ge, as it shows the characteristic shape of neutron peaks in a HPGe detector. In addition, by gating on this photopeak, no other transitions of the same cascade are observed.

For beam energy $E(^{18}\mathrm{O}) = 65$ MeV the spectra have shown the highest peak–to–background ratio for the 602 keV transition of ^{140}Ba. The situation is the same as for the previous beam energies, with the same transitions shown in the $\gamma\gamma$–coincidence spectra. The corresponding coincidence spectrum, gated on 602 keV, is shown in Fig. 5.3.

For beam energy $E(^{18}\mathrm{O}) = 67$ MeV, the 602 keV transition has shown a higher counting rate but the peak–to–background ratio for the 602 keV transition showed to be worse than in the case of that with 65 MeV beam energy. This results from the high beam-induced background coming from the fusion-evaporation reactions described in Eq. 5.1. The coincidence spectrum

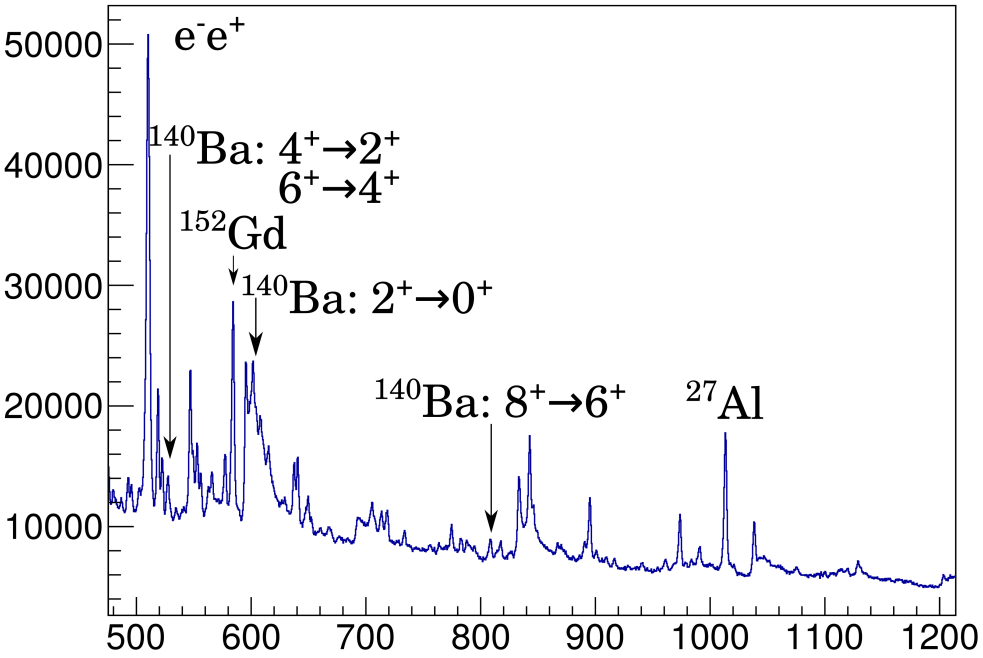

(a)

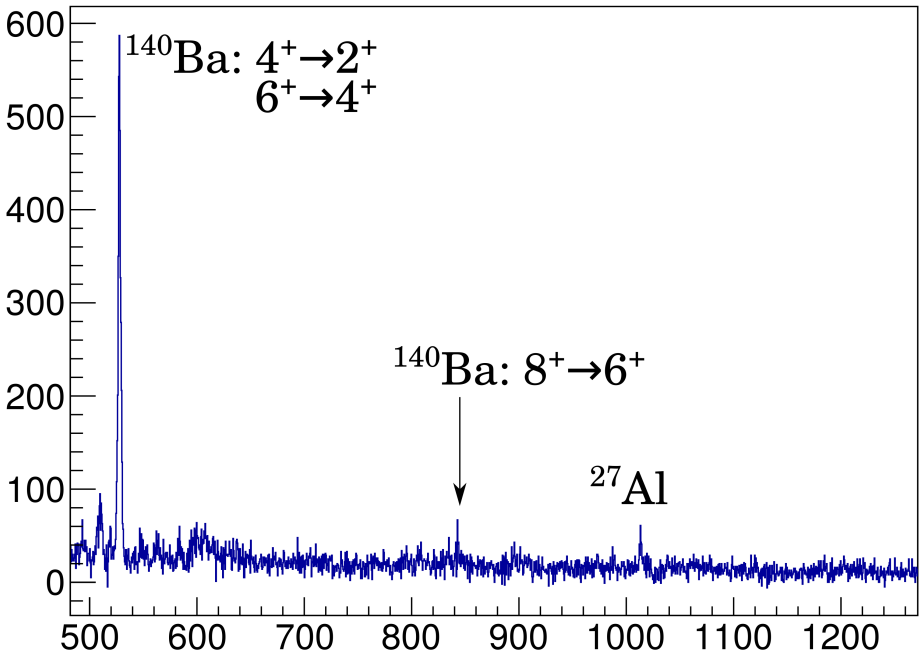

(b)

Figure 5.2: Projection of the symmetric $\gamma\gamma$–matrix (a) and the coincidence spectrum (b) gated at 602 keV transition for beam energy of 63 MeV. See text for details.

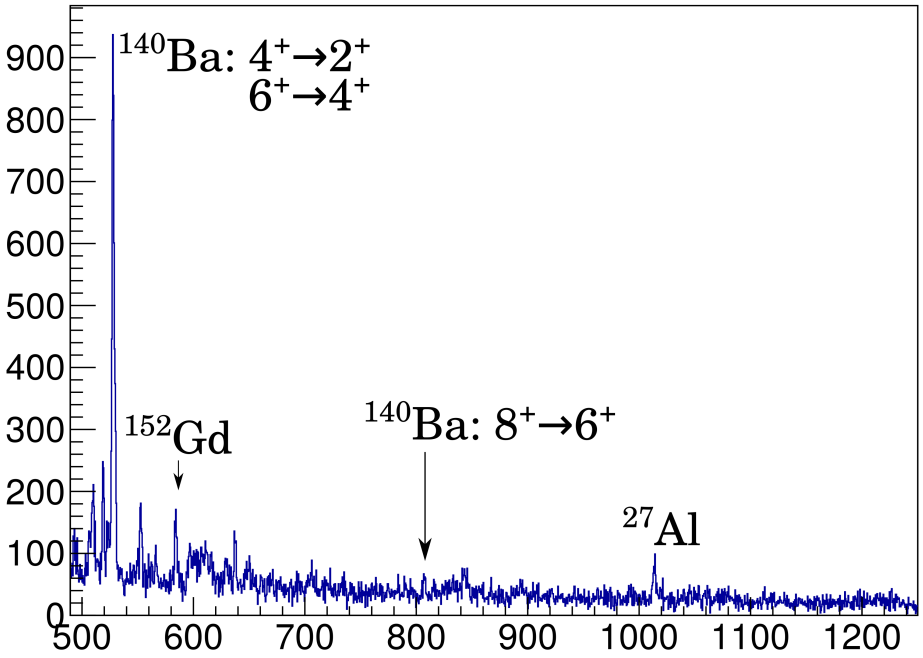

Figure 5.3: Coincidence spectrum at beam energy of 65 MeV.

is shown on Fig 5.4. Due to the short time of the run ($\sim$ 30 minutes), the statistics is obviously low, making visible only the two overlapping transitions $4_1^+ \rightarrow 2_1^+$ and $6_1^+ \rightarrow 4_1^+$.

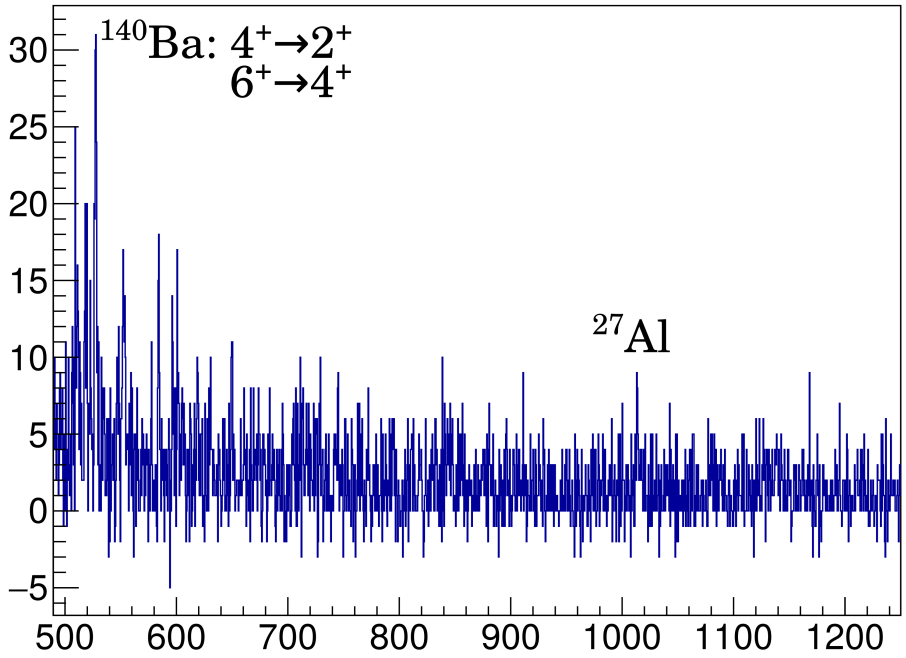

Figure 5.4: Coincidence spectrum for beam energy of 67 MeV.

5.1.1 Lifetimes

Lower limits on lifetimes of the states up to 8^+ in the ground–state band [20], corresponding to the observed transitions can be set, by taking into account the limitation of the Doppler Shift Attenuation Method (DSAM) [56, 58]. In Fig. 5.5a, the two overlapping transitions of energies 528 and 530 keV are shown, depopulating the 4^+ and 6^+ states of the ground–state band. As it can be seen for the spectra recorded in the backward (143°) and forward ring (37°), no visible lineshapes can be distinguished. The same holds for Fig. 5.5b, where the transition of 808 keV is depopulating the 8^+, also in the ground–state band.

The maximum recoil velocity in the particular reaction mechanism is 2% the speed of light. At such recoil velocities, the range of lifetimes that can be measured with DSAM should be lower than approximately 1 ps [56, 57, 74, 75]. The present limit is established in terms of the range of lifetimes that the particular method can be applied, and not the sensitivity of the experimental

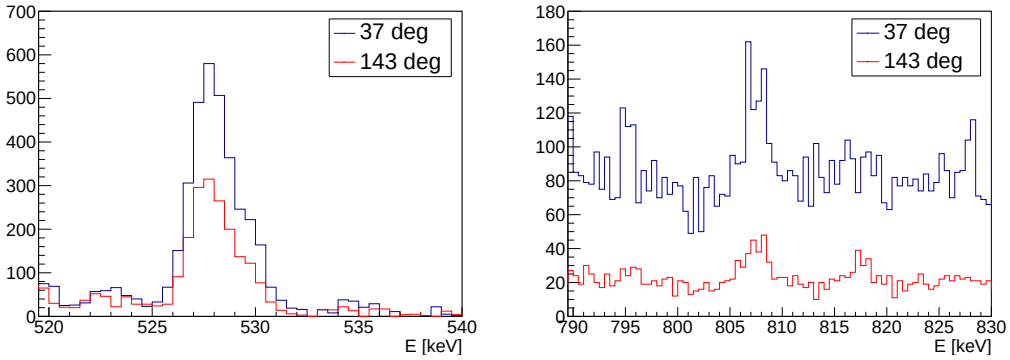

(a) (b)

Figure 5.5: Backward (143°) and forward (37°) spectra for (a) the 528 and 530 keV overlapping transitions, and (b) for the 808 keV transition. The spectra show no backward–forward lineshapes.

setup.

5.1.2 Relative cross sections

The cross section of a reaction can be estimated by the relation:

$$\sigma = \frac{N_R}{\Phi N_t} \tag{5.2}$$

where N_R is the number of occurring reactions, N_t is the number of target nuclei that the beam interacts with, and Φ is the incident flux of projectiles.

The reactions

$$\begin{aligned} {}^{18}\mathrm{O} + {}^{138}\mathrm{Ba} &\rightarrow {}^{16}\mathrm{O} + {}^{140}\mathrm{Ba} \\ &\rightarrow {}^{152}\mathrm{Gd} + 4n \\ &\rightarrow {}^{18}\mathrm{O} + {}^{138}\mathrm{Ba}^{*} \end{aligned}$$

stem from the same entry channel and occur inside the barium foil. In general, the relative cross section for two different exit channels α, β can be estimated by:

$$\sigma_R = \frac{N_R(\alpha)}{N_R(\beta)} \tag{5.3}$$

i.e. by determining the ratios of the corresponding number of reactions.

In the present case, the number of reactions can be deduced by measuring all observed photopeaks feeding the ground state of the produced nuclei for the

two above exit channels, and then correcting with the full absolute efficiency of the ROSPHERE array:

$$N_R = \frac{A}{\epsilon_{abs}} \tag{5.4}$$

where A is the area of the photopeak and ϵ_{abs} is the absolute efficiency.

For the $2n$-transfer reaction ^{18}O+^{138}Ba→^{16}O+^{140}Ba, only the $E_\gamma = 602$ keV transition was observed, while for the ^{18}O+^{138}Ba→^{152}Gd+$4n$ reaction, only the transition with $E_\gamma = 344$ keV [20] was recorded in the data. Also, for the total inelastic channel, the transition $E_\gamma = 1436$ keV was observed [20]. A projection spectrum of the full $\gamma\gamma$ matrix is shown in Fig. 5.6, with the peaks of interest marked.

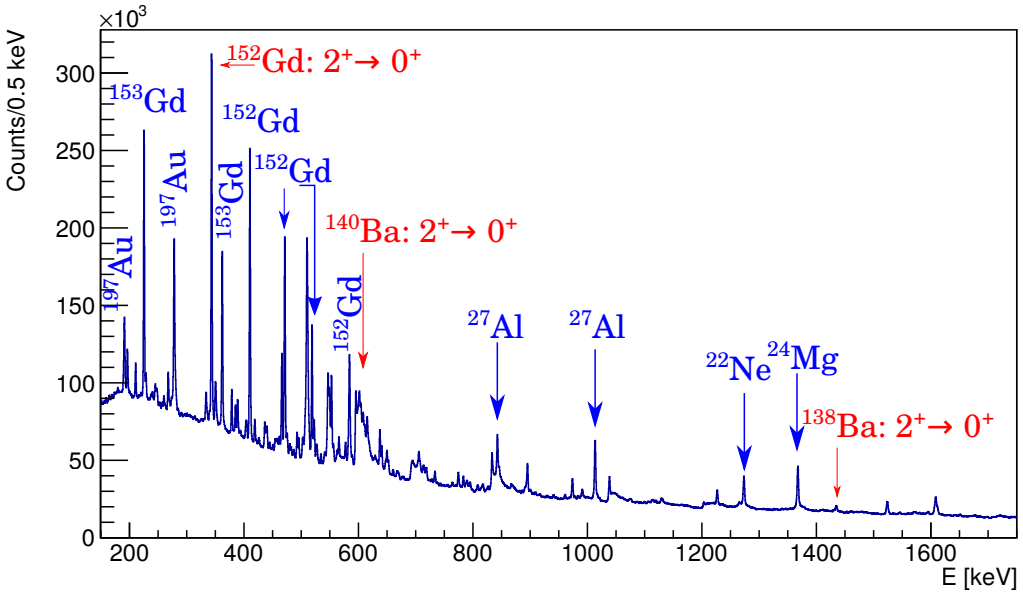

Figure 5.6: Total projection spectrum from the $\gamma\gamma$ matrix acquired using the ROSPHERE array. Transitions in barium isotopes are marked, as well as several from the fusion–evaporation channels. A few contaminant peaks are also indicated.

By extracting the ratios, and taking into account the energy loss inside the barium foil of the target (Table 5.2), the results for the relative cross sections of the $2n$-neutron transfer reaction ^{18}O + ^{138}Ba→^{16}O + ^{140}Ba with respect to the fusion–evaporation counterpart ^{18}O + ^{138}Ba→^{152}Gd + $4n$ and with respect to the total inelastic channel are shown in Fig. 5.7 as a function of energy in

the laboratory system. The energy loss in for each beam energy has been determined using the SRIM2013 code [76].

Table 5.2: Experimental results and theoretical calculations. From left to right column: E_b is the beam energy; E_{Ba} is the incident energy of at the front of the Barium foil, by taking into consideration the beam energy loss inside the front Au foil; ΔE_{Ba} is the total energy loss in the barium foil; E_{eff} is the effective energy at the middle of the barium foil; σ_R^{fus} is the ratio of the $2n$–transfer reaction cross section over the cross section of the fusion-evaporation channel (see eq. 5.3); σ_R^{inel} is the ratio of the $2n$–transfer reaction cross section over the total inelastic cross section; σ_{Gd} and σ_{Ba} are normalized cross sections (see text for details); σ_{PACE} and $\sigma_{GRAZING}$ are results of `PACE4` [77] and `GRAZING 9` [45] calculations for the ^{18}O + ^{138}Ba→^{152}Gd + 4n and ^{18}O + ^{138}Ba→^{16}O + ^{140}Ba reactions, respectively. All values are in the laboratory system.

E_b (MeV)	E_{Ba} (MeV)	ΔE_{Ba} (MeV)	E_{eff} (MeV)	σ_R^{fus}	σ_R^{inel}	σ_{Gd} (mb)	σ_{Ba} (mb)	σ_{PACE4} (mb)	$\sigma_{GRAZING}$ (mb)
61	60.04	4.91	57.59	0.3±0.1	0.7±0.4	0.43±0.01	0.11±0.06	–	0.1112
63	62.05	4.83	59.64	0.12±0.01	0.8±0.1	2.46±0.01	0.29± 0.04	0.00178	0.33087
65	64.06	4.75	61.69	0.107±0.006	1.8±0.1	8.02±0.04	0.86±0.06	0.847	0.63257
67	66.07	4.68	63.73	0.06±0.01	2.0±0.5	23.4±0.1	1.5±0.3	23.4	0.89368

5.2 Cross section predictions

In order to further investigate the experimental values of the relative cross sections measured in the present work, theoretical calculations have been per-

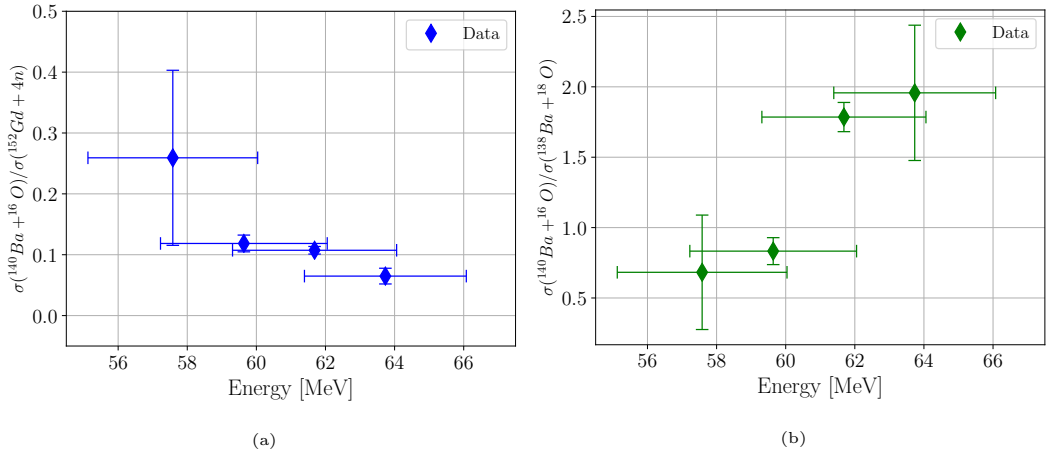

(a) (b)

Figure 5.7: Relative cross section of the two neutron–transfer reaction ^{18}O+^{138}Ba→^{16}O+^{140}Ba with respect to the fusion-evaporation reaction ^{18}O+^{138}Ba→^{152}Gd+4n (left) and the ratio with respect to the total inelastic channel ^{18}O+^{138}Ba→^{16}O+^{138}Ba* (right).

formed using the GRAZING 9 [45] and PACE4 [77] codes.

The former uses Winther's grazing model [45], which has been proven successful for the description of one– or two–nucleon transfer reactions [46]. Calculations performed with the GRAZING 9 code use a semi–classical approach developed in [47]. For a small number of nucleon transfers (up to 6–8 neutrons) and for nuclei close to the magic shell closures, the particular model describes experimental data very well; however, it tends to slightly underestimate the data for large numbers of nucleons (see discussion in [48]).

On the other hand, the PACE4 code is the latest version of a modified JULIAN code [50] and uses the Bass model [49], which was derived by using a geometric interpretation of available experimental data combined with a Monte–Carlo approach to determine the decay of the compound system in the framework of Hauser–Feshbach formalism [51]. As stated in Ref. [46], the Bass model potential provides an overall excellent description for the fusion cross sections at energies starting from the Coulomb barrier and above. However, experimental evidence shows that the particular model significantly underestimates the cross section data below the Coulomb barrier [46].

All calculations have been performed using the default parameters each code employs. Fig. 5.8 shows the results of the calculations: Fig. 5.8a includes cross section calculations with PACE4 (solid circles), while Fig. 5.8b contains calculated cross sections with GRAZING 9 (solid squares). PACE4 could not produce a value at the lowest energy (E_{eff}=57.6 MeV), as was expected, since this value is far below the barrier. The experimental absolute yield for the fusion–evaporation channel is shown in Fig. 5.8 (solid diamonds). All data points have been normalized with a single numerical factor. That factor was estimated by scaling the experimental point at the energy nearest to the barrier (E_{eff}=63.7 MeV) with the respective value calculated with PACE4 (see overlapping points in Fig. 5.8a).

Calculations with GRAZING 9 are shown in Fig. 5.8b (solid squares). In the same graph, experimental data of the 2n–transfer reaction ^{18}O + ^{138}Ba $\rightarrow$ ^{16}O

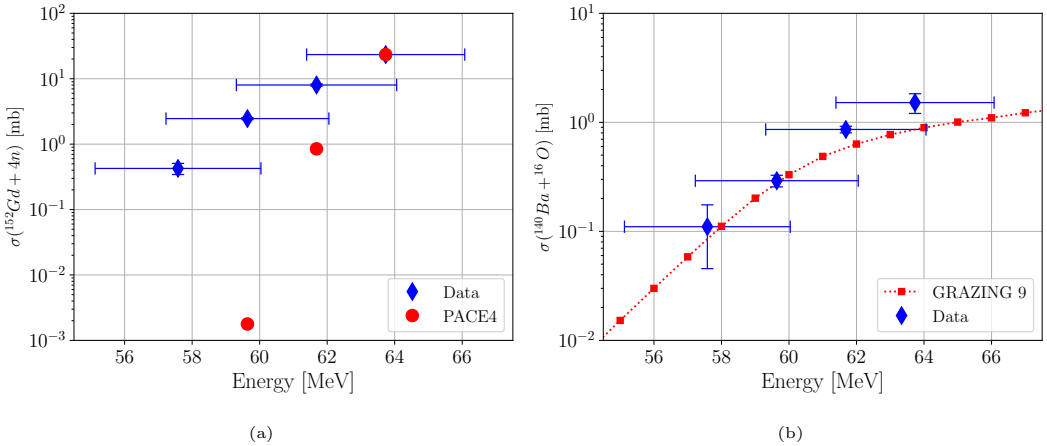

Figure 5.8: (a) Normalized cross sections of the fusion–evaporation channel after normalization to `PACE4` calculations (see text). Vertical error bars are smaller than the symbol size. (b) Deduced cross sections for the 2n–neutron transfer channel (solid diamonds) after taking into account the results from panel (a), together with `GRAZING 9` calculations (solid squares). No scaling is involved in any of the data sets in panel (b). The dotted line is to guide the eye. Scales of y–axes in (a) and (b) are different.

+ ^{140}Ba are shown. These data have been extracted from the ratio in Fig. 5.7 taking into account the scaled cross sections of the fusion–evaporation channel, as described earlier. No further scaling is involved.

5.3 Discussion

Within the present framework, a study of the nucleus ^{140}Ba by using the $2n$–transfer reaction ^{18}O + ^{138}Ba $\rightarrow$ ^{16}O + ^{140}Ba, has been performed. By considering the kinematics of the reaction studied and the limitation of DSAM, lower limits on the lifetimes of 3 states of the ground state band have been set over 1 ps. Of course, further studies are necessary in order to further constrain the above limit. The present results also set the path for using a different technique for the measurement of the particular lifetimes, such as the plunger technique or the fast–timing technique. For direct measurement of the reduced transition probabilities, especially for the $B(E3)$ corresponding to the first 3^- state, the use of radioactive beams and Coulomb excitation technique can override a lot of issues, such as possible target contamination and the level

population strength.

The relative cross sections between the $2n$–transfer reaction ^{18}O + ^{138}Ba $\rightarrow$ ^{16}O + ^{140}Ba and the competing fusion–evaporation reaction ^{18}O + ^{138}Ba $\rightarrow$ ^{152}Gd + 4n have been deduced by taking into account the relative yield of the two observed transitions feeding the ground state of the two produced nuclei. The relative cross section behavior seems to follow a reducing pattern with respect to beam energy, showing that the fusion–evaporation channel becomes stronger faster, as the Coulomb barrier is approached. This behavior is rather expected given the fact that the reactions occur in the pure–tunneling energy range. In addition, the relative cross sections of the reaction ^{18}O + ^{138}Ba $\rightarrow$ ^{16}O + ^{140}Ba and the total inelastic channel are presented. The inelastic channel is a competing reaction channel, which as can be seen from Fig. 5.7b, the respective cross section values are of the same order of magnitude within the studied energy range. The behavior of these cross sections follows an increasing pattern, indicating that the 2n–transfer reaction shows a stronger increase as the energy increases towards the Coulomb barrier.

Absolute cross sections deduced with this method, taking advantage of the ratios of cross sections, may be lower than their actual values, as some transitions feeding the ground state may not be observed in the spectra, resulting in missing strength in the overall estimation. In addition, the ^{152}Gd decay features $E0$ transitions directly to the ground state. It is very hard to observe such transitions in the γ–spectrum, despite their contribution to the total number of produced nuclei. While this can be usually treated as a weak effect, it cannot be assumed with certainty.

Calculations with the theoretical codes `PACE4` and `GRAZING 9` have been performed to provide a comparison with experimental data produced in the present work. The scaling of the experimental data to the `PACE4` result at the maximum energy, almost identical to the energy of the barrier, can be trusted to produce absolute cross sections for the absolute cross sections in the fusion–evaporation channels. This becomes evident when the deduced

cross sections for the studied $2n$–transfer reaction are further compared to `GRAZING 9` calculations. There is a very good agreement between experimental data and theory, both in trend and in magnitude. The two lowest energy points are effectively the same within the experimental uncertainty, while the discrepancy between the rest is of the order of 20%. It has to be stressed again that this comparison involves no other scaling than the one used for the fusion–evaporation channel.

Chapter 6

Conclusions

A study of the two neutron-rich nuclei ^{180}Hf and the ^{140}Ba has been presented in this work, as the outcome of two experiments that have been carried out at the 9MV Tandem accelerator laboratory in Horia Hulubei National Institute of Physics and Nuclear Engineering (IFIN-HH) [16].

The stable neutron-rich ^{180}Hf was populated using the proton pick-up reaction ^{181}Ta(^{11}B,^{12}C)^{180}Hf, at 47 MeV beam energy, for the first time. The ground-state band up to the 1084 keV level, the side-band levels of 1370 keV (band 6), 1374 keV (band 2) and non-band levels 1821 keV, 1608 keV have been populated. The statistics was sufficient to extract spins-parities and mixing ratios for these levels and the corresponding transitions depopulating them. The disagreement between the spin value of the 1374 keV band 2 state between [24] and [25] seems to be settled, as the new value measured in this work clearly favors a spin-parity value of 4^-. A new value for the mixing ratio ($\delta = -0.03^{+0.03}_{-0.05}$) for the transition 1374 $\rightarrow$ 309 is suggested which agrees with the previous measurement in [24] and is more precise. Furthermore, measurements for spins-parities and mixing ratios have been presented for the rest of the previously mentioned side-band and non-band states, and mixing ratio values for the transitions 1821 $\rightarrow$ 1200 keV and 1608 $\rightarrow$ 1200 keV transitions are reported for the first time.

Despite the large uncertainties in some measurements, possible spins and mixing ratios have been determined for the populated states in ^{180}Hf. The present work can set the path for new measurements, aiming on the lifetimes of these states. The measured mixing ratios coupled with lifetime measurements will allow then the estimation of the corresponding reduced transition probabilities, which can provide useful insight for the structure of ^{180}Hf.

The neutron-rich nucleus ^{140}Ba has been also studied in this work, using the $2n$-transfer reaction ^{138}Ba(^{18}O,^{16}O)^{140}Ba. The reaction populated significantly the ground-state band up to the 8^+ level, overcoming major technical difficulties such as the target oxidation, allowing an extraction of a lower-limit in the lifetimes of the $8^+, 6^+$ and 4^+. In addition, a side-measurement of the currently unmeasured cross sections of the $2n$-transfer ^{138}Ba(^{18}O,^{16}O)^{140}Ba reaction near the Coulomb barrier has also been performed in this work. The measurement was performed using the relative values of the cross-sections of ^{138}Ba(^{18}O,^{16}O)^{140}Ba and the fusion-evaporation reaction ^{138}Ba(^{18}O,$4n$)^{152}Gd together with theoretical calculations for the latter reaction, using `PACE4` [77]. The derived cross sections of ^{138}Ba(^{18}O,^{16}O)^{140}Ba are found to be in excellent agreement with theoretical calculations using the `GRAZING 9` [45] code.

However, the 3^-_1 state of ^{140}Ba was not populated. Although the answer of whether the specific nucleus is characterized by enhanced octupole correlation cannot be given from this work, the results presented are enough to pinpoint the next directions of studies in this nucleus. Employing a similar method as used in the two neighbouring isotopes ^{144,146}Ba in [28, 29], by using a ^{140}Ba radioactive beam together with Coulomb excitation can possibly lead to a measurement of the $B(E3; 0^+_{g.s.} \rightarrow 3^-)$, the value of which would determine the strength of octupole collectivity and establish the onset of octupole correlations in the Ba isotopic chain.

Appendices

Appendix A

Transition probability relations for the lowest multipoles

For the lowest for multipoles, the following relations for electric transitions obtained [6]:

$$T(E1) = 1.59 \times 10^{15} E_\gamma^3 B(E1) \quad \text{(A.1)}$$

$$T(E2) = 1.23 \times 10^{9} E_\gamma^5 B(E2) \quad \text{(A.2)}$$

$$T(E3) = 5.71 \times 10^{2} E_\gamma^7 B(E3) \quad \text{(A.3)}$$

$$T(E4) = 1.70 \times 10^{-4} E_\gamma^9 B(E4) \quad \text{(A.4)}$$

while for magnetic transitions:

$$T(M1) = 1.76 \times 10^{13} E_\gamma^3 B(M1) \quad \text{(A.5)}$$

$$T(M2) = 1.35 \times 10^{7} E_\gamma^5 B(M2) \quad \text{(A.6)}$$

$$T(M3) = 6.31 \times 10^{0} E_\gamma^7 B(M3) \quad \text{(A.7)}$$

$$T(M4) = 1.88 \times 10^{-6} E_\gamma^9 B(M4) \quad \text{(A.8)}$$

where the transition energy E_γ is in MeV, $B(EL)$ in units of $e^2 fm^{2L}$ and $B(ML)$ in units of $\mu_N^2 fm^{2L-2}$.

Appendix B

ROSPHERE detector angles and distances

The geometry of the 25 HPGe ROSPHERE setup is given in Table B.1. The type (Ortec or Canberra), the coordinates and the distances from the center of the target chamber are given for each detector. θ° is the angle with respect to the beam direction and ϕ° is the azimuthal angle, with $\phi^\circ = 0$ the direction pointing to the ground and its positive direction is counter-clockwise with respect to the beam.

Table B.1: List of the 25 HPGe setup of ROSPHERE. Their coordinates (θ, ϕ) as well as their distances from the center of the target chamber are listed.

HPGe Index #	θ°	ϕ°	Type	Distance [cm]
1	37	0	Ortec	17.9
2	37	72	Ortec	17.9
3	37	144	Canberra	21.0
4	37	216	Ortec	17.9
5	37	288	Ortec	17.9
6	70	36	Ortec	18.6
7	70	108	Canberra	21.7
8	70	180	Canberra	21.7
9	70	252	Ortec	18.6
10	70	324	Ortec	18.6
11	90	0	Canberra	20.8
12	90	288	Canberra	20.8
13	90	216	Canberra	20.8
14	90	144	Canberra	20.8
15	90	72	Ortec	17.6
16	110	36	Canberra	21.7
17	110	108	Canberra	21.7
18	110	180	Ortec	18.6
19	110	252	Ortec	18.6
20	110	324	Ortec	18.6
21	143	0	Canberra	21.0
22	143	288	Ortec	17.9
23	143	216	Canberra	21.0
24	143	144	Canberra	21.0
25	143	72	Ortec	17.9

References

[1] E. Caurier, G. Martínez-Pinedo, F. Nowacki, A. Poves, and A. P. Zuker, "The shell model as a unified view of nuclear structure," *Rev. Mod. Phys.*, vol. 77, pp. 427–488, 2005.

[2] J. L. Durell, "The structure and spectroscopy of neutron-rich nuclei," *The European Physical Journal A*, vol. 15, p. 167, 2002.

[3] A. Bohr and B. R. Mottelson, "Rotational states in even-even nuclei," *Phys. Rev.*, vol. 90, pp. 717–719, 1953.

[4] W. Hamilton, *The electromagnetic interaction in nuclear spectroscopy.* North-Holland, Amsterdam, 1975.

[5] B. A. Brown and W. A. Richter, "Magic numbers in the neutron-rich oxygen isotopes," *Phys. Rev. C*, vol. 72, no. 057301, 2005.

[6] S. Wong, *Introductory Nuclear Physics.* Wiley, New York, 2008.

[7] C. Bertulani, *Nuclear Physics in a Nutshell.* In a Nutshell, Princeton University Press, 2007.

[8] A. Sitenko and V. Tartakovskii, *Lectures on the Theory of the Nucleus.* Pergamon, Oxford, 1975.

[9] L. Corradi, G. Pollarolo, and S. Szilner, "Multinucleon transfer processes in heavy-ion reactions," *Journal of Physics G: Nuclear and Particle Physics*, vol. 36, no. 113101, 2009.

[10] R. A. Broglia, O. Hansen, and C. Riedel, *Two-Neutron Transfer Reactions and the Pairing Model*, pp. 287–457. Boston, MA: Springer US, 1973.

[11] D. Bés, R. Broglia, O. Hansen, and O. Nathan, "Isovector pairing vibrations," *Physics Reports*, vol. 34, no. 1, pp. 1 – 53, 1977.

[12] M. Igarashi, K. Kubo, and K. Yagi, "Two-nucleon transfer reaction mechanisms," *Physics Reports*, vol. 199, no. 1, pp. 1 – 72, 1991.

[13] S. Leoni, B. Fornal, N. Mărginean, M. Sferrazza, Y. Tsunoda, T. Otsuka, G. Bocchi, F. C. L. Crespi, A. Bracco, S. Aydin, M. Boromiza, D. Bucurescu, N. Cieplicka-Oryńczak, C. Costache, S. Călinescu, N. Florea, D. G. Ghiţă, T. Glodariu, A. Ionescu, L. Iskra, M. Krzysiek, R. Mărginean, C. Mihai, R. E. Mihai, A. Mitu, A. Negreţ, C. R. Niţă, A. Olăcel, A. Oprea, S. Pascu, P. Petkov, C. Petrone, G. Porzio, A. Şerban, C. Sotty, L. Stan, I. Ştiru, L. Stroe, R. Şuvăilă, S. Toma, A. Turturică, S. Ujeniuc, and C. A. Ur, "Multifaceted quadruplet of low-lying spin-zero states in ^{66}Ni: Emergence of shape isomerism in light nuclei," *Phys. Rev. Lett.*, vol. 118, no. 162502, 2017.

[14] K. Nowak, K. Wimmer, S. Hellgartner, D. Mücher, V. Bildstein, J. Diriken, J. Elseviers, L. P. Gaffney, R. Gernhäuser, J. Iwanicki, J. G. Johansen, M. Huyse, J. Konki, T. Kröll, R. Krücken, R. Lutter, R. Orlandi, J. Pakarinen, R. Raabe, P. Reiter, T. Roger, G. Schrieder, M. Seidlitz, O. Sorlin, P. Van Duppen, N. Warr, H. De Witte, and M. Zielińska, "Spectroscopy of ^{46}Ar by the (t, p) two-neutron transfer reaction," *Phys. Rev. C*, vol. 93, no. 044335, 2016.

[15] K. E. Rehm, "Quasi-elastic heavy-ion collisions," *Annual Review of Nuclear and Particle Science*, vol. 41, no. 1, pp. 429–468, 1991.

[16] "Institutul National de Cercetare-Dezvoltare pentru Fizica si Inginerie Nucleara Horia Hulubei." www.nipne.ro/, 2003.

[17] D. Bucurescu, I. Căta-Danil, G. Ciocan, C. Costache, D. Deleanu, R. Dima, D. Filipescu, N. Florea, D. Ghiţă, T. Glodariu, M. Ivaşcu, R. Lică, N. Mărginean, R. Mărginean, C. Mihai, A. Negret, C. Niţă, A. Olăcel, S. Pascu, T. Sava, L. Stroe, A. Şerban, R. Şuvăilă, S. Toma, N. Zamfir, G. Căta-Danil, I. Gheorghe, I. Mitu, G. Suliman, C. Ur, T. Braunroth, A. Dewald, C. Fransen, A. Bruce, Z. Podolyák, P. Regan, and O. Roberts, "The ROSPHERE γ-ray spectroscopy array," *Nuclear Instruments and Methods in Physics Research Section A: Accelerators, Spectrometers, Detectors and Associated Equipment*, vol. 837, pp. 1 – 10, 2016.

[18] S. K. Tandel, P. Chowdhury, F. G. Kondev, R. V. F. Janssens, T. L. Khoo, M. P. Carpenter, T. Lauritsen, C. J. Lister, D. Seweryniak, S. Zhu, A. Deacon, S. J. Freeman, N. J. Hammond, G. D. Jones, E. F. Moore, and J. F. Smith, "Configurations and decay hindrances of high-k states in ^{180}Hf," *Phys. Rev. C*, vol. 94, p. 064304, Dec 2016.

[19] P. M. Walker and F. R. Xu, "High K-isomerism in rotational nuclei," *Physica Scripta*, vol. 91, no. 013010, 2015.

[20] The Evaluated Nuclear Structure Data File (ENDSF), http://www.nndc.bnl.gov/ensdf/, accessed 2020.

[21] S. B. Burson, K. W. Blair, H. B. Keller, and S. Wexler, "The radiations from Hafnium," *Phys. Rev.*, vol. 83, pp. 62–68, 1951.

[22] R. D'Alarcao, P. Chowdhury, E. H. Seabury, P. M. Walker, C. Wheldon, I. Ahmad, M. P. Carpenter, G. Hackman, R. V. F. Janssens, T. L. Khoo, C. J. Lister, D. Nisius, P. Reiter, D. Seweryniak, and I. Wiedenhoever, "High-K isomers in neutron-rich hafnium nuclei at and beyond the stability line," *Phys. Rev. C*, vol. 59, pp. R1227–R1231, 1999.

[23] J. Wiederhold, V. Werner, R. Kern, N. Pietralla, D. Bucurescu, R. Carroll,

N. Cooper, T. Daniel, D. Filipescu, N. Florea, R.-B. Gerst, D. Ghita, L. Gurgi, J. Jolie, R. S. Ilieva, R. Lica, N. Marginean, R. Marginean, C. Mihai, I. O. Mitu, F. Naqvi, C. Nita, M. Rudigier, S. Stegemann, S. Pascu, and P. H. Regan, "Evolution of $e2$ strength in the rare-earth isotopes ^{174,176,178,180}Hf," *Phys. Rev. C*, vol. 99, p. 024316, 2019.

[24] E. Grigorev, V. Bodarenko, and K. Nam, "Angular distributions of γ rays from the 180hf(n,n'γ) reaction and new bands of 180hf," *Sov. J. Nuc. Phys.*, vol. 54, p. 914, 1991.

[25] S. Boneva, E. Vasileva, V. Kulik, L. Kkhem, Y. Popov, A. Sukhovoi, V. Khitrov, and Y. Kholnov, "Two-quantum cascades and decay scheme of the compound state of 180hf excited in the reaction 179hf(n, 2γ)," *Izv.Akad.Nauk SSSR, Ser.Fiz.*, vol. 54, p. 1787, 1991.

[26] P. A. Butler and W. Nazarewicz, "Intrinsic reflection asymmetry in atomic nuclei," *Rev. Mod. Phys.*, vol. 68, pp. 349–421, 1996.

[27] C. Bauer, T. Behrens, V. Bildstein, A. Blazhev, B. Bruyneel, J. Butterworth, E. Clément, L. Coquard, J. L. Egido, A. Ekström, C. R. Fitzpatrick, C. Fransen, R. Gernhäuser, D. Habs, H. Hess, J. Leske, T. Kröll, R. Krücken, R. Lutter, P. Marley, T. Möller, T. Otsuka, N. Patronis, A. Petts, N. Pietralla, T. R. Rodríguez, N. Shimizu, C. Stahl, I. Stefanescu, T. Stora, P. G. Thirolf, D. Voulot, J. van de Walle, N. Warr, F. Wenander, and A. Wiens, "Prolate shape of ^{140}ba from a first combined doppler-shift and coulomb-excitation measurement at the rex-isolde facility," *Phys. Rev. C*, vol. 86, no. 034310, 2012.

[28] B. Bucher, S. Zhu, C. Y. Wu, R. V. F. Janssens, D. Cline, A. B. Hayes, M. Albers, A. D. Ayangeakaa, P. A. Butler, C. M. Campbell, M. P. Carpenter, C. J. Chiara, J. A. Clark, H. L. Crawford, M. Cromaz, H. M. David, C. Dickerson, E. T. Gregor, J. Harker, C. R. Hoffman, B. P. Kay, F. G. Kondev, A. Korichi, T. Lauritsen, A. O. Macchiavelli, R. C. Pardo,

A. Richard, M. A. Riley, G. Savard, M. Scheck, D. Seweryniak, M. K. Smith, R. Vondrasek, and A. Wiens, "Direct evidence of octupole deformation in neutron-rich ^{144}Ba," *Phys. Rev. Lett.*, vol. 116, no. 112503, 2016.

[29] B. Bucher, S. Zhu, C. Y. Wu, R. V. F. Janssens, R. N. Bernard, L. M. Robledo, T. R. Rodríguez, D. Cline, A. B. Hayes, A. D. Ayangeakaa, M. Q. Buckner, C. M. Campbell, M. P. Carpenter, J. A. Clark, H. L. Crawford, H. M. David, C. Dickerson, J. Harker, C. R. Hoffman, B. P. Kay, F. G. Kondev, T. Lauritsen, A. O. Macchiavelli, R. C. Pardo, G. Savard, D. Seweryniak, and R. Vondrasek, "Direct evidence for octupole deformation in ^{146}Ba and the origin of large $e1$ moment variations in reflection-asymmetric nuclei," *Phys. Rev. Lett.*, vol. 118, no. 152504, 2017.

[30] J. Egido and L. Robledo, "A self-consistent approach to the ground state and lowest-lying negative-parity state in the barium isotopes," *Nuclear Physics A*, vol. 518, no. 3, pp. 475 – 495, 1990.

[31] L. M. Robledo, M. Baldo, P. Schuck, and X. Viñas, "Octupole deformation properties of the barcelona-catania-paris energy density functionals," *Phys. Rev. C*, vol. 81, no. 034315, 2010.

[32] A. Bohr and B. Mottelson, *Nuclear Deformations*. No. Vol. 2 in Nuclear Structure, World Scientific, Singapore, 1998.

[33] B. L. Berman and S. C. Fultz, "Measurements of the giant dipole resonance with monoenergetic photons," *Rev. Mod. Phys.*, vol. 47, pp. 713–761, 1975.

[34] K. Heyde, *Basic Ideas and Concepts in Nuclear Physics: An Introductory Approach*. Institute of Physics, Bristol, 1999.

[35] K. S. Krane, *Introductory nuclear physics*. Wiley, New York, 1988.

[36] S. Robinson, "How reliable are spins and δ-values derived from directional correlation experiments?," *Nuclear Instruments and Methods in Physics Research Section A: Accelerators, Spectrometers, Detectors and Associated Equipment*, vol. 292, no. 2, pp. 386 – 400, 1990.

[37] J. Lange, K. Kumar, and J. H. Hamilton, "E0-E2-M1 multipole admixtures of transitions in even-even nuclei," *Rev. Mod. Phys.*, vol. 54, pp. 119–194, 1982.

[38] K. Krane, R. Steffen, and R. Wheeler, "Directional correlations of gamma radiations emitted from nuclear states oriented by nuclear reactions or cryogenic methods," *Atomic Data and Nuclear Data Tables*, vol. 11, no. 5, pp. 351 – 406, 1973.

[39] H. J. Rose and D. M. Brink, "Angular distributions of gamma rays in terms of phase-defined reduced matrix elements," *Rev. Mod. Phys.*, vol. 39, pp. 306–347, 1967.

[40] K. Siegbahn, *Alpha-, Beta- and Gamma-Ray Spectroscopy.* Elsevier Science, Amsterdam, 2012.

[41] M. Rotenberg, R. Bivins, N. Metropolis, and J. Wooten, *The 3-j and 6-j Symbols. [By] M. Rotenberg, R. Bivins, N. Metropolis, John K. Wooten.* Cambridge, Mass., 1959.

[42] S. Szilner, C. A. Ur, L. Corradi, N. Mărginean, G. Pollarolo, A. M. Stefanini, S. Beghini, B. R. Behera, E. Fioretto, A. Gadea, B. Guiot, A. Latina, P. Mason, G. Montagnoli, F. Scarlassara, M. Trotta, G. d. Angelis, F. D. Vedova, E. Farnea, F. Haas, S. Lenzi, S. Lunardi, R. Mărginean, R. Menegazzo, D. R. Napoli, M. Nespolo, I. V. Pokrovsky, F. Recchia, M. Romoli, M.-D. Salsac, N. Soić, and J. J. Valiente-Dobón, "Multinucleon transfer reactions in closed-shell nuclei," *Phys. Rev. C*, vol. 76, p. 024604, 2007.

[43] V. Zagrebaev and W. Greiner, "Production of new heavy isotopes in low–energy multinucleon transfer reactions," *Phys. Rev. Lett.*, vol. 101, p. 122701, 2008.

[44] S. Heinz, "Multinucleon transfer reactions – a pathway to new heavy and superheavy nuclei?," *Journal of Physics: Conference Series*, vol. 1014, no. 012005, 2018.

[45] A. Winther, "Grazing reactions in collisions between heavy nuclei," *Nuclear Physics A*, vol. 572, no. 1, pp. 191 – 235, 1994.

[46] W. Reisdorf, "Heavy-ion reactions close to the coulomb barrier," *Journal of Physics G: Nuclear and Particle Physics*, vol. 20, pp. 1297–1353, sep 1994.

[47] K. Wendt, S. A. Ahmad, C. Ekström, W. Klempt, R. Neugart, and E. W. Otten, "Hyperfine structure and isotope shift of the neutron-rich barium isotopes $^{139--146}$Ba and ^{148}Ba," *Zeitschrift für Physik A Atomic Nuclei*, vol. 329, no. 4, pp. 407–411, 1988.

[48] V. V. Samarin, "Few-nucleon transfers and weakly dissipative processes in the grazing model of low-energy nuclear reactions," *Bulletin of the Russian Academy of Sciences: Physics*, vol. 77, no. 7, pp. 820–824, 2013.

[49] R. Bass, "Nucleus-nucleus potential deduced from experimental fusion cross sections," *Phys. Rev. Lett.*, vol. 39, pp. 265–268, 1977.

[50] M. Hillman and Y. Eyal, "Code JULIAN (unpublished); Gavron, A.: Modification JULIAN PACE," *Phys. Rev. C*, vol. 21, p. 230, 1980.

[51] W. Hauser and H. Feshbach, "The inelastic scattering of neutrons," *Phys. Rev.*, vol. 87, pp. 366–373, 1952.

[52] L. Marinescu, V. Zoran, S. Dobrescu, G. Pascovici, G. Semenescu, G. Marmureanu, H. Sandi, and T. Sireteanu, "A concept for earthquake protec-

tion of the bucharest tandem accelerator," *Nuclear Instruments and Methods in Physics Research Section A: Accelerators, Spectrometers, Detectors and Associated Equipment*, vol. 287, no. 1, pp. 127 – 131, 1990.

[53] R. V. D. Graaff, "Tandem electrostatic accelerators," *Nuclear Instruments and Methods*, vol. 8, no. 2, pp. 195 – 202, 1960.

[54] C. Rolfs and W. Rodney, *Cauldrons in the Cosmos: Nuclear Astrophysics*. Theoretical Astrophysics, University of Chicago Press, 1988.

[55] D. Bucurescu, I. Căta-Danil, G. Ciocan, C. Costache, D. Deleanu, R. Dima, D. Filipescu, N. Florea, D. Ghiţă, T. Glodariu, M. Ivaşcu, R. Lică, N. Mărginean, R. Mărginean, C. Mihai, A. Negret, C. Niţă, A. Olăcel, S. Pascu, T. Sava, L. Stroe, A. Şerban, R. Şuvăilă, S. Toma, N. Zamfir, G. Căta-Danil, I. Gheorghe, I. Mitu, G. Suliman, C. Ur, T. Braunroth, A. Dewald, C. Fransen, A. Bruce, Z. Podolyák, P. Regan, and O. Roberts, "The rosphere γ-ray spectroscopy array," *Nuclear Instruments and Methods in Physics Research Section A: Accelerators, Spectrometers, Detectors and Associated Equipment*, vol. 837, pp. 1 – 10, 2016.

[56] T. K. Alexander and J. S. Forster, *Lifetime Measurements of Excited Nuclear Levels by Doppler-Shift Methods*, pp. 197–331. Boston, MA: Springer US, 1978.

[57] P. Petkov, A. Dewald, and P. von Brentano, "A new procedure for lifetime determination using the doppler-shift attenuation method," *Nuclear Instruments and Methods in Physics Research Section A: Accelerators, Spectrometers, Detectors and Associated Equipment*, vol. 560, no. 2, pp. 564 – 570, 2006.

[58] P. Petkov, D. Tonev, J. Gableske, A. Dewald, and P. von Brentano, "Lifetime analysis using the doppler-shift attenuation method with a gate on

feeding transition," *Nuclear Instruments and Methods in Physics Research Section A: Accelerators, Spectrometers, Detectors and Associated Equipment*, vol. 437, no. 2, pp. 274 – 281, 1999.

[59] A. Dewald, O. Möller, and P. Petkov, "Developing the recoil distance doppler-shift technique towards a versatile tool for lifetime measurements of excited nuclear states," *Progress in Particle and Nuclear Physics*, vol. 67, no. 3, pp. 786 – 839, 2012.

[60] Marginean, N., Balabanski, D. L., Bucurescu, D., Lalkovski, S., Atanasova, L., Cata-Danil, G., Cata-Danil, I., Daugas, J. M., Deleanu, D., Detistov, P., Deyanova, G., Filipescu, D., Georgiev, G., Ghita, D., Gladnishki, K. A., Lozeva, R., Glodariu, T., Ivascu, M., Kisyov, S., Mihai, C., Marginean, R., Negret, A., Pascu, S., Radulov, D., Sava, T., Stroe, L., Suliman, G., and Zamfir, N. V., "In-beam measurements of sub-nanosecond nuclear lifetimes with a mixed array of hpge and labr3:ce detectors," *Eur. Phys. J. A*, vol. 46, no. 3, pp. 329–336, 2010.

[61] G. F. Knoll, *Radiation Detection and Measurement*. Wiley, New York, 2011.

[62] W. R. Leo, *Techniques for Nuclear and Particle Physics Experiments*. Springer-Verlag, 1994.

[63] "Nucléide - Lara, library for gamma and alpha emissions." http://www.nucleide.org/Laraweb/index.php. Accessed: 2020-04-24.

[64] N. Mărginean, "Gaspware analysis software." private communication.

[65] G. Gilmore, *Practical Gamma-ray Spectroscopy*. Wiley, 2011.

[66] N. M. Florea, L. Stroe, R. Mărginean, D. G. GhiŢă, D. Bucurescu, M. Badea, C. Costache, R. Lică, N. Mărginean, C. Mihai, D. V. Moşu, C. R. NiŢă, S. Pascu, and T. Sava, "The status of the target preparation

laboratory at ifin-hh bucharest, romania," *Journal of Radioanalytical and Nuclear Chemistry*, vol. 305, no. 3, pp. 707–711, 2015.

[67] Z. Kis, B. Fazekas, J. Östör, Z. Révay, T. Belgya, G. Molnár, and L. Koltay, "Comparison of efficiency functions for ge gamma-ray detectors in a wide energy range," *Nuclear Instruments and Methods in Physics Research Section A: Accelerators, Spectrometers, Detectors and Associated Equipment*, vol. 418, no. 2, pp. 374 – 386, 1998.

[68] I.-J. Kim, Sun, Gwang-Min, and H. D. Park, "Calculation of effective angular correlation in the hpge spectroscopy of co-60 γ-rays," *J. Korean Nuclear Society*, vol. 34, no. 1, p. 22, 2002.

[69] K. Krane, "Solid-angle correction factors for coaxial ge(li) detectors," *Nuclear Instruments and Methods*, vol. 98, no. 2, pp. 205 – 210, 1972.

[70] "Python software foundation. python language reference, version 3.6." https://www.python.org/. Accessed: 2020.

[71] D. Cline and P. Lesser, "Error estimation in non-linear least squares analysis of data," *Nuclear Instruments and Methods*, vol. 82, pp. 291 – 293, 1970.

[72] "GRIFFIN-collaboration", "Angular Correlation Utility." http://griffincollaboration.github.io/AngularCorrelationUtility/, 2016. [Online; accessed 2020].

[73] A.A. Rodionov, S.L. Sakharov and Yu.L. Khazov, "Internal conversion electrons from reaction ^{179}Hf(n,γ)," *Program and Theses, Proc.36th Ann.Conf.Nucl.Spectrosc.Struct.At.Nuclei, Kharkov*, 1986.

[74] C. Mihai, A. A. Pasternak, D. Filipescu, M. Ivaşcu, D. Bucurescu, G. Căta Danil, I. Căta Danil, D. Deleanu, D. Ghiţă, T. Glodariu, Y. N. Lobach, N. Mărginean, R. Mărginean, A. Negret, S. Pascu, T. Sava, L. Stroe, G. Suliman, and N. V. Zamfir *Phys. Rev. C*, vol. 81, no. 034314, 2010.

[75] P. Petkov, "Robustness of the analysis of Doppler-shift attenuation lifetime measurements according to the coincidence differential decay curve method with respect to class of uncertainties in the stopping powers," *AIP Advances*, vol. 8, no. 7, 2018.

[76] J. F. Ziegler, M. Ziegler, and J. Biersack, "Srim – the stopping and range of ions in matter (2010)," *Nuclear Instruments and Methods in Physics Research Section B: Beam Interactions with Materials and Atoms*, vol. 268, no. 11, pp. 1818 – 1823, 2010. 19th International Conference on Ion Beam Analysis.

[77] A. Gavron, "Statistical model calculations in heavy ion reactions," *Phys. Rev. C*, vol. 21, pp. 230–236, 1980.